BRIDGING THE GAP IN UNDERSTANDING BONE AT MULTIPLE LENGTH SCALES USING FLUID DYNAMICS

by

ERIC JAMES ANDERSON

Submitted in partial fulfillment of the requirements

For the degree of Doctor of Philosophy

Dissertation Advisor: Dr. Melissa Knothe Tate

Department of Mechanical & Aerospace Engineering

CASE WESTERN RESERVE UNIVERSITY

January, 2007

CASE WESTERN RESERVE UNIVERSITY

SCHOOL OF GRADUATE STUDIES

We hereby approve the dissertation of

Eric J. Anderson

candidate for the Ph.D. degree *.

(signed) Melissa L. Knothe Tate
(chair of the committee)

Joseph Prahl

Clare M. Rimnac

Donald Feke

Harihara Baskaran

(date) November 21, 2006

*We also certify that written approval has been obtained for any proprietary material contained therein.

CONTENTS

LIST OF TABLES

LIST OF FIGURES

ACKNOWLEDGEMENTS

I would like to thank a number of people who have supported me throughout my undergraduate and graduate education. To begin, I wish to express my sincere gratitude to my graduate advisor, Dr. Melissa Knothe Tate for her mentorship over the last four years and for providing me with the opportunity to expand into a new field. Her unique outlook on research, teaching, and life as well as the numerous opportunities to present my research across the country and world have enhanced my education and provided me with exciting and unique experiences.

Furthermore, I would like to thank everyone in the mechanobiology laboratory for their friendship and support over the years, and in particular, Adam Sorkin and Tom Falls for their help with the experimental testing and design studies.

Sincere appreciation is also extended to Dr. Joseph Prahl and Dr. Iwan Alexander for their support, conversations, and advising throughout my undergraduate and graduate education, as well as the Department of Mechanical & Aerospace Engineering for support throughout the years.

I would also like to thank the members of my dissertation committee, Dr. Donald Feke, Dr. Clare Rimnac, and Dr. Harihara Baskaran for their comments and suggestions.

Finally and most importantly, I would like to thank my parents for their confidence and support over the last seven years and for making my education possible, as well as my brother and Danielle for their continued love and support, and being a strong reason to stay and pursue my Ph.D.

Bridging the Gap in Understanding Bone at Multiple Length Scales using Fluid Dynamics

Abstract

by

ERIC JAMES ANDERSON

Fluid flow through the network of pathways in bone tissue is hypothesized to play an integral role in transducing external mechanical forces from the skeletal level down to the cells embedded deep within bone tissue. Communicating these external forces to bone cells is thought to be the mechanism by which bone is regenerated, and thus has major implications in fighting bone disease as well as repairing defects or damage to the tissue. This research pursues the role of fluid flow in bone remodeling and looks to bridge the gap between tissue and cellular level knowledge using computational fluid dynamics modeling of the Navier-Stokes equations as well as experimental validations of applicable models.

Using physiologic model geometries of increasing complexity, the following work predicts currently immeasurable properties of the tissue such as permeability or cell communication, as well as the resultant mechanical forces as they exist at the cellular and subcellular levels. The mechanical environment of the osteocyte is described, where the mode and magnitude of force on the cell varies spatio-temporally. Both hydrodynamic pressure and imparted shear stress are found on the cell surface, where the cell body

experiences a nearly constant pressure and virtually zero shear stress while the cell processes are exposed to high gradients of both shear stress and pressure. This differentiation between types and location of forces has possible implications in cell physiology and the types of receptors or mechanosensors present on the cell. In addition, along the cell processes, which radiate from the cell body, subcellular geometries near the lower continuum-limit yield small discontinuities in the annular wall that are found to amplify peak shear stresses up to five times that of previous predictions. This result gives insight into a major paradox that has existed in bone and suggests a bridge between theoretical predictions and laboratory measurements of the necessary mechanical force for cell stimulation, where previous *in vitro* measurements have been an order of magnitude higher than *in vivo* predictions. This knowledge of the cell's mechanical environment is used to improve and design applications for laboratory cell studies and tissue growth *in vitro*.

CHAPTER 1

General Introduction

Background

For more than a century the relationship between bone and its mechanical environment has been studied at the organ and tissue scales using experimental, analytical, and computational techniques. In the late 19th century, Roux (1881) and Wolff (1884) independently described the relationship between the structure and function of bone, where bone optimizes its material properties and architecture in response to the functional demands placed upon it (mechanical loads) [1-3]. Investigators have strived to understand the mechanisms of this structure-function relationship in hopes of manipulating the mechanical environment to repair or grow bone tissue and/or to prevent or reverse bone disease. Although research has focused on elucidation of external mechanical loads as well as the underlying mechanisms in which bone senses and adapts to its mechanical environment, the means by which external mechanical signals are transduced to the cellular level in bone, a process referred to as mechanotransduction, remains unclear. A mechanotransduction event *per se* can occur either via a direct transmission of a mechanical signal to a receptors on a cell surface or indirectly via a mechanically modulated transport of molecules, such as nutrients, growth factors and cytokines, that bind at cell surfaces, subsequently triggering up- or down-regulation of gene activity within the cell nucleus [35,33].

As a material, bone is comprised of both solid (75%) and liquid (25%) phases. The form of each phase is dictated by the length scale of interest, e.g. hierarchically, from the systemic (skeleton) to organ, tissue, cellular, and subcellular scales [4]. The solid

phase, or mineralized matrix, is analogous to a porous sponge; a number of studies have described the variation in bone's solid phase morphology and material properties as a function of bone type, location and length scale [5]. Similarly, the geometry of bone's fluid cavities and properties of the fluid within those cavities change with length scale, from the vascular Haversian canals (μm) to the lacunocanalicular system (μm – nm) and matrix microporosity (nm-Å). At the μm scale of the vascular system, e.g. the Haversian and Volkmann canals, the fluid is comprised of blood, which is non-Newtonian fluid and whose flow properties are well understood. Going below the length scale of a single blood cell, *i.e.* at the nm-μm scale of the fluid within the lacunocanalicular spaces surrounding bone cells (osteocytes) and their processes, the fluid no longer exhibits properties similar to the non-Newtonian fluid (blood) within the vascular system. Due to the nature of bone itself and the remoteness of the lacunocanalicular system, the fluid within these spaces can not be extracted in sufficient quantity or without introduction of artifacts, both of which would be necessary to elucidate the exact chemical composition of the fluid [6]. Thus, the chemical composition and properties of bone's pericellular fluid are unknown. Hence, for the purposes of analytical and computational studies of flow through bone's pericellular fluid spaces, the fluid is estimated to be plasma-like, with a slightly higher viscosity than water. Although this approximation may be appropriate for predictions of flow properties, it should be noted that bone's nonvascular fluid exhibits a higher concentration of potassium than plasma [6,47]; hence, this approximation would not be appropriate for biochemical models.

In applying Biot's theory of poroelasticity [7] to model bone as a fluid-filled sponge, external mechanical loading is predicted to deform the porous tissue, which

induces internal pressure gradients and cyclical fluid movement within the pericellular space [8,9]. In recent decades, numerous *in vivo* [10,11] and *in vitro* [12-17] studies have investigated the relationship between bone cells (osteoblasts, osteoclasts, and osteocytes) and their surrounding mechanical-fluid environment. Consequently, it is hypothesized that fluid flow is an integral component in mechanotransduction. However, as mentioned previously, the specific mechanisms of mechanotransduction in bone are not yet understood [18-22].

Ideally, the role of fluid flow in mechanotransduction would be observed directly in *in vivo* experimental models. However, current limitations in optical imaging as well as the opacity and geometric complexity of bone currently render such studies impossible. Thus, theoretical and computational models have been designed to elucidate fluid movement at multiple length scales in bone. Over the past decade, several studies have predicted flow in bone from a macroscopic perspective, where the tissue is considered to be a porous media with given bulk properties obtained from macroscopic experimental measures [23-34]. These results have paved a way for a general understanding of flow magnitude and direction; however they cannot be extrapolated to the cellular scale, where continuum or bulk properties no longer apply. For this purpose, cell scale models have been developed, using macroscopic data, to predict more accurate flow parameters through a pericellular network [9,5,35-45]. Typically, these studies have used highly idealized geometries to approximate the pericellular network. The degree to which these approximations accurately describe the specific flow regimes and forces imparted to the cells themselves was unknown at the start of the research program described in this dissertation. Hence, at the start of these studies, a gap in understanding existed between

pericellular flow at the organ-tissue scale and the cell scales. This gap in understanding was thought to be key to solving a paradox in the field of bone fluid flow, where mechanical forces predicted, based on *in vivo* data, to occur at the cellular level are orders of magnitude lower than those required to induce a cellular response in *in vitro* studies [46].

Purpose

The previously mentioned paradox provided the impetus for the studies described herein, with the goal to bridge the gap in understanding fluid flow at bone's lowest and highest length scales. Specifically, computational fluid dynamics predictions and experimental measurements were carried out in nano-microanatomically true scale models of pericellular spaces in bone. Extending beyond the macroscopic organ-level models, this work begins with a network of cells at the tissue level, continues down in length scale to understand flow around a single cell, and culminates with an investigation of flow in subcellular nanoscale spaces. Applications of the acquired knowledge are presented as well, where optimization of flow regimes are carried out for controlled mechanical stresses to cells seeded within flow chambers and tissue engineering scaffolds for *in vitro* studies.

Beginning with the tissue-level in Chapter 2, fluid flow around a network of cells in the lacunocanalicular network is investigated. Confocal images of actual lacunocanalicular geometry are used to create both computational as well as scaled-up physical models of the micro- and nanoscale pathways. A description of cellular communication is sought by measuring permeability experimentally in the physical models. Analytical and computational models are then applied to determine scaling

factors and to perform parametric studies on the effects of virtually included cellular and subcellular structures. These results not only build upon the work of previous macroscopic models, they also provide parameters of the microscale flow pathways in bone that cannot be acquired from *in vivo* experimental observation.

Building on tissue-level results, models of cellular-level flow are presented in Chapter 3. Specific flow regimes around a single cell are predicted, where computational models of an osteocyte cell body with several orientations and variations of attached cell processes are created. For a physiologic pressure drop obtained from previous macroscale studies [24,25], the resulting Reynolds number, pressure gradient, velocity in the pericellular space, and imparted shear stress on the cell surface is calculated. Particular attention is focused on the location and type of mechanical force found at the cell level, as an understanding of the variation in mechanical stimulation combined with cell physiology may play a key role in unraveling the underlying mechanisms of mechanotransduction.

Having established a basic understanding of the mechanical environment of osteocytes, Chapter 4 analyzes mechanical forces imparted to cell processes (areas of high shear stress) for specific physiologic geometries, thus underscoring the effects of geometry idealization. Transmitted electron microscopy (TEM) is used to acquire high resolution images of the cell process and the surrounding mineralized bone matrix. Dimensionless pressure, velocity, and wall shear stress are calculated for an applied pressure drop. Parametric and statistical analyses are carried out to determine variability in peak stresses on the process surface. Based on microcrack geometries from previous studies [44], flow and stress variations are also predicted for damaged bone.

Applications of the results found in Chapters 2-4 are presented in Chapters 5 and 6, where descriptions of the fluid environment of osteocytes embedded within bone are used to design and optimize *in vitro* flow devices. Chapter 5 investigates commercial cell flow chamber performance, where such devices are designed to provide a controlled mechanical stress to a cell monolayer seeded within the chamber. With regard to the physiologic fluid environment of bone cells, the flow regimes and imparted forces are calculated in four chamber models. Computational results are then validated using micro-PIV techniques in each physical chamber. In Chapter 6, knowledge of the predicted mechanical stimulation to cells *in vivo* is used to characterize and optimize the fluid geometry in tissue engineering scaffolds. In order to grow bone tissue in the laboratory using tissue engineering scaffolds, the structure must provide the necessary environment for cells seeded within. For a specific scaffold target geometry, the target pressure gradient, velocity, shear stress, and permeability are calculated for a given pressure drop. Variations in these parameters are then predicted for geometrical discrepancies due to the manufacturing process. Differences between target and actual flow parameters are used to present a practical tool for scaffold optimization which obviates the need for iterative experimentation and scaffold fabrication.

Finally, in Chapter 7 conclusions are drawn on the work presented. The impact of these results on our understanding of mechanotransduction in bone is discussed, as well as their implications for applications and future studies.

REFERENCES

1. Roux W, 1885. Beiträge zur Morphologie der funktionellen Anpassung. Arch Anat Physiol Anat Abt 120-185.

2. Wolff J, 1892. Das Gesetz der Transformation der Knochen. Berlin, Hirschwald.

3. Roesler H, 1981. Some historical remarks on the theory of cancellous bone structure (Wolff's Law). In The Joint ASME-ASCE Applied Mechanics, Fluids Engineering and Bioengineering Conference: Mechanical Properties of Bone. New York. pp. 27-42.

4. Knothe Tate ML, 2003. "Whither flows the fluid in bone?" An osteocyte's perspective. J Biomech 36:1409-1424.

5. Piekarski K, 1981. Mechanically enhanced perfusion in bone. In the Joint ASME-ASCE Applied Mechanics, Fluids Engineering and Bioengineering Conference: Mechanical Properties of Bone. New York.

6. Knothe Tate ML, 2001. Interstitial fluid flow. In: Cowin SC (ed.) Bone Mechanics Handbook. Ch. 22. pp. 1-29.

7. Biot MA, 1941. General theory of three-dimensional consolidation. J Applied Physics 12:155-164.

8. Bassett CA, 1965. Electrical effects in bone. Scientific American 213:18-25.

9. Piekarski K, Munro M, 1977. Transport mechanism operating between blood supply and osteocytes in long bones. Nature 269:80-82.

10. Lanyon LE, Baggott DG, 1976. Mechanical function as an influence on the structure and form of bone. J Bone Joint Surg 58B:436-443.

11. Rubin CT, Lanyon LE, 1985. Regulation of bone mass by mechanical strain magnitude. Calc Tissue Intl 37:411-417.

12. Burger EH, Veldhuijzen JP, 1993. Influence of mechanical factors on bone formation, resorption and growth in vitro. In: Hall BK (ed.) Bone, vol. 7. CRC Press, Boca Raton, FL, USA, pp. 37-56.

13. Almekinders LC, Banes AJ, Ballenger CA, 1993. Effects of repetitive motion on human fibroblasts. Med Sci Sports Exerc 25:603-607.

14. Klein-Nulend J, van der Plas A, Semeins CM, Ajubi NE, Frangos JA, Nijweide PJ, Burger EH, 1995. Sensitivity of osteocytes to biomechanical stress in vitro. FASEB J 9:441-445.

15. Guilak F, Ratcliffe A, Mow VC, 1995. Chondrocyte deformation and local tissue strain in articular cartilage: a confocal microscopy study. J Orthop Res 13:410-421.

16. Smalt R, Mitchell FT, Howard RL, Chambers TJ, 1997. Induction of NO and prostaglandin E2 in osteoblasts by wall shear stress but no mechanical strain. Am J Physiol 273:E751-758.

17. You J, Yellowley CE, Donahue HJ, Zhang Y, Chen Q, Jacobs CR, 2000. Substrate deformation levels associated with routine physical activity are less stimulatory to bone cells relative to loading-induced oscillatory fluid flow. J Biomech Eng 122:387-393.

18. Knothe Tate ML, Knothe U, Niederer P, 1998a. Experimental elucidation of mechanical load-induced fluid flow and its potential role in bone metabolism and functional adaptation. Am J Med Sci 316:189-195.

19. Knothe Tate ML, Niederer P, Knothe U, 1998b. In vivo tracer transport through the lacunocanalicular system of rat bone in an environment devoid of mechanical loading. Bone 2:107-117.

20. Knothe Tate ML, Knothe U, 2000. An ex vivo model to study transport processes and fluid flow in loaded bone. J Biomech 33:247-254.

21. Johnson DL, McAllister TN, Frangos JA, 1996. Fluid flow stimulates rapid and continuous release of nitric oxide in osteoblasts. Am Physiol Soc 205-208.

22. Owan I, Burr DB, Turner CH, Qiu J, Tu Y, Onya JE, Duncan RL, 1997. Mechanotransduction in bone: osteoblasts are more responsive to fluid forces than mechanical strain. Am J Physiol 273:C810-C815.

23. Nowinski JL, Davis CF, 1972. The flexure and torsion of bones viewed as anisotropic poroelastic bodies. Intl J Eng Sci 10:1063-1079.

24. Zhang D, Cowin SC, 1994. Oscillatory bending of a poroelastic beam. J Mech Phys Solids 42:1575-1599.

25. Zhang D, Cowin SC, 1996. Load carrying capacity of the pore pressure in a poroelastic beam subject to oscillatory excitation. In: Selvadurai (Eds.) Mechanics of poroelastic media. Kluwer Academic Publishers, pp. 273-298.

26. Liebschner MAK, Keller TS, 1999. The importance of the permeability constant in hydraulic strengthening of cortical bone. In: ASME Bioengineering Division, Summer Conference.

27. Manfredini P, Cocchetti G, Maier G, Redaelli A, Montevicchi FM, 1999. Poroelastic finite element analysis of a bone specimen under cyclic loading. J Biomech 32:135-144.

28. Zhang D, Weinbaum S, Cowin SC, 1998a. Estimates of the peak pressures in bone water. J Biomed Eng 120:697-703.

29. Zhang D, Weinbaum S, Cowin SC, 1998b. On the calculation of bone pore water pressure due to mechanical loading. Intl J Solids Struc 35:4981-4997.

30. Prendergast PJ, Huiskes R, Soballe K, 1997. Biophysical stimuli on cells during tissue differentiation at implant interfaces. J Biomech 30:539-548.

31. Lacroix D, Prendergast PJ, 2000. Mechanotransduction during fracture healing: the effect of cell proliferation. In: Ribreau, Berland, Moreau, Ratier, Renaudeaux, Thiriet, Wendling (Eds.) Mechanotransduction. Groupement pour l'avancement des methods d'analyse des contraintes G.A.M.A.C. et Soci, Paris, pp. 39-46.

32. Steck R, Niederer P, Knothe Tate ML, 2000. A finite difference model of load-induced fluid displacements within bone under mechanical loading. Med Eng Phys 22:117-125.

33. Steck R, Niederer P, Knothe Tate ML, 2003. A finite element analysis for the prediction of load-induced fluid flow and mechanochemical transduction in bone. J Theor Biol 220:249-259.

34. Tami AE, Schaffler MB, Knothe Tate ML, 2003. Probing the tissue to subcellular level structure underlying bone's molecular sieving function. Biorheology 40:577-590.

35. Knothe Tate ML, Niederer P, 1998. Theoretical FE-based model developed to predict the relative contribution of convective and diffusive transport mechanisms for the maintenance of local equilibria with cortical bone. In: Clegg S (ed.) Advances in heat and mass transfer in biotechnology, American Society of Mechanical Engineers, New York, pp. 133-142.

36. Weinbaum S, Cowin Sc, Zeng Y, 1992. Fluid shear stress excitation of osteocytes. Adv Bioeng 22:25-28.

37. Weinbaum S, Cowin SC, Zeng Y, 1994. A model for the excitation of osteocytes by mechanical loading-induced bone fluid shear stresses. J Biomech 27:339-360.

38. Johnson MW, Chakkalakal DA, Harper RA, Katz JL, Rouhana SW, 1982. Fluid flow in bone in vitro. J Biomech 15:881-885.

39. Johnson MW, Katz JL, 1984. Some new developments in the rheology of bone. Biorheology 1:169-174.

40. Harrigan TP, Hamilton JJ, 1993. Bone strain sensation via transmembrane potential changes in surface osteoblasts: Loading rate and microstructural implications. J Biomech 26:183-200.

41. Cowin SC, Weinbaum S, Zeng Y, 1995. A case for bone canaliculi as an anatomical site of strain generated potentials. J Biomech 28:1281-1297.

42. Wang L, Fritton SP, Cowin SC, Weinbaum S, 1999. Fluid pressure relaxation depends upon osteonal microstructure: modeling an oscillatory bending experiment. J Biomech 32:663-672.

43. Han Y, Cowin SC, Schaffler MB, Weinbaum S, 2004. Mechanotransduction and strain amplification in osteocyte cell processes. Proc Natl Acad Sci 101:16689-16694.

44. Tami AE, Nasser P, Verborgt O, Schaffler MB, Knothe Tate ML, 2002. The role of interstitial fluid flow in the remodeling response to fatigue loading. J Bone Miner Res 7:2030-2037.

45. Steck R, Knothe Tate ML, 2005. In silico stochastic network models that emulate the molecular sieving characterstics of bone. Ann Biomed Eng 33:87-94.

46. Rubin CT, Lanyon LE, 1984. Regulation of bone formation by applied dynamic loads. J Bone Joint Surg 66A:397-410.

47. Neuman MW, Neuman WF, 1980. On the measurement of water compartments, pH and gradients in calvaria. Calcif Tissue Int 31:135-145.

CHAPTER 2

Pairing computational and scaled physical models to determine permeability as a measure of cellular communication in micro- and nano-scale pericellular spaces

Eric J. Anderson[1], Steven M. Kreuzer[1], Oliver Small[2], Melissa L. Knothe Tate[1,2]

[1]Dept of Mechanical & Aerospace Engineering, Case Western Reserve University, Cleveland, OH
[2]Dept of Biomedical Engineering, Case Western Reserve University, Cleveland, OH

Submitted to *Microfluidics and Nanofluidics Journal*

ABSTRACT

The pericellular fluid environment can be difficult to study due to remoteness and complexity of its nanoscale fluid pathways. The degree to which the pericellular fluid environment modulates the transport of mechanical and molecular signals is unknown. As a consequence, experimental and computational studies have been limited and/or highly idealized. In this study we apply a fundamental fluid dynamics technique to measure pericellular permeability through scaled-up physical models obtained from high resolution microscopy. We assess permeability of physiologic tissue by tying together data from parallel experimental and computational models that account for specific structures of the mineralized flow cavities and cellular structures therein (body, process, pericellular matrix). These studies show that a healthy cellular network devoid of cellular

structure exhibits permeability on the order of 2.8×10^{-16} m^2; inclusion of cellular structures reduces permeability to the order of 10^{-17} - 10^{-18} m^2. These permeability studies provide not only unprecedented quantitative experimental measures of the pericellular fluid environment but also provide a novel measure of "infrastructural integrity" that likely influences the efficiency of the cellular communication networks across the tissue.

INTRODUCTION

Cells are the living component of tissues, which are self-annealing biological materials. The self-annealing property of tissues represents the end result of cell activity over the time period of observation, which enables tissues to remodel or adapt functionally in response to environmental cues such as mechanical loading or disuse (Fig 2.1). Tissue remodeling depends on patent cellular machinery, as well as cellular navigation and coordination. The cellular mechanisms underlying tissue remodeling are poorly understood.

All cells of the human body are bathed in fluid. The pericellular fluid provides a medium through which environmental cues (mechanical, chemical, electrical) are transmitted to cells, resulting in up- or down regulation of gene expression (Fig 2.1)[1-4]. Delineated by the structural network of cells, which in themselves allow for direct cell to cell signal transmission across the tissue (intracellular signaling)[1], the contiguous pericellular fluid provides a powerful extracellular means to modulate cellular activity (Fig 2.1). Elucidation of the pericellular fluid environment could provide important

insight into mechanisms underlying cellular navigation and coordination during tissue remodeling.

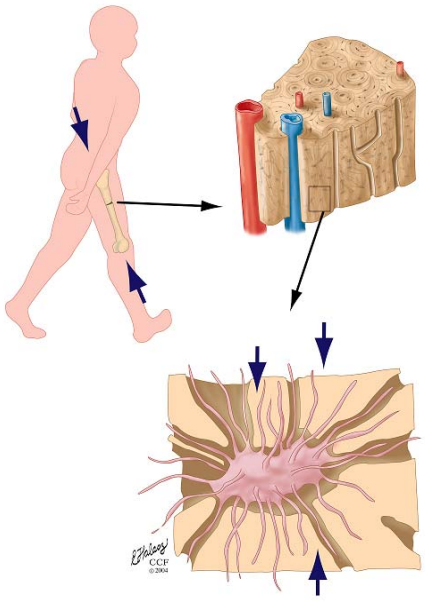

Figure 2.1: Schematic of fluid transport in the periosteocytic lacunocanalicular network. Both chemical and mechanical signals are transported by the fluid.

The pericellular fluid environment is interdependent on the state of the solid mechanical elements of the tissue, as mechanical loading of tissue causes pericellular fluid to move, much like the fluid moves when a saturated sponge is squeezed[5]. One measure of the interplay between the solid and fluid phases of a biological material is permeability. In this study, permeability through the micro- and nanoscale pericellular fluid network provides a measure of the tissue's capacity for transport of signals and molecules via the cellular fluid network. Experimental measurements as well as computational predictions of tissue permeability are challenging due to the remote location of cells and their networks. Hence, the goal of this study is to implement an experimental and computational scaling approach to determine the permeability of the nano-microscale fluid space around cells that comprise the living component of the

biological tissue in which they reside, thus providing not only an unprecedented experimental measurement but also a means to validate computational predictions.

Parametric scaling or similitude analysis is a fundamental science and engineering approach used to study mechanics in very large or small scale systems where direct measures are impossible[6-9], *e.g.* in the pericellular fluid space. By scaling down, *e.g.* an airplane or wing, experiments can be carried out on the scaled model to determine the desired flow parameters normally too difficult to measure in the actual system[22,23]. These parameters can then be related, through the scaling relationship, to the large-scale parameters found in the actual system. When applied to fluid dynamics[10-14], qualitative and quantitative descriptions of flow regimes can be obtained using scaling relationships if viscous and inertial forces (Reynolds number) are maintained across length scales.

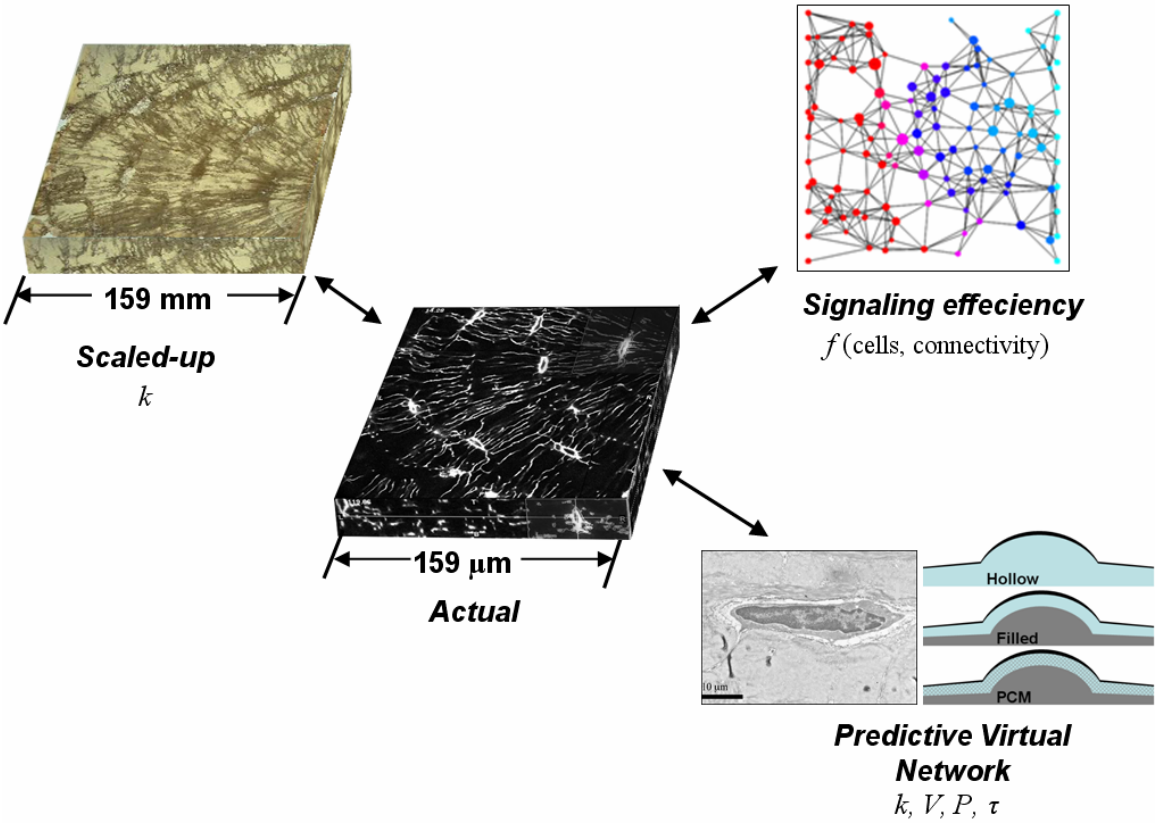

Figure 2.2: Schematic of computational and experimental techniques used to determine properties of the lacunocanalicular network and osteocyte communication or connectivity.

In the present study, scaled physical models and predictive virtual and stochastic computational models are used in parallel to determine the effect of cell connectivity and network organization on communication and transport across tissues (referred to hereafter as *signal transmission efficiency*, see Fig 2.2 for overview). Fluid flow rates are measured experimentally by applying a pressure head to scaled-up, rapid prototyped physical models of pericellular fluid networks created from three-dimensional confocal imaging data. By scaling the measured flow rate down to the cellular scale, fluid network permeability can be calculated using Darcy's Law. To complement the physical model, which accounted for the pericellular network devoid of cellular and sub-cellular structures, virtual computational models are created to investigate the effect of cellular and pericellular structures on network permeability. Finally, stochastic network models are used to estimate changes in signal transmission efficiency as a function of changes in network connectivity.

METHODS

Creation of Scaled-up, physical models

Tissue specimens are obtained from the cortical sheath of the femoral neck from human patients undergoing orthopaedic surgery; specimens diagnosed with pathology are excluded from this study (Fig. 2.3, IRB approved, exemption #4). The tissue is bulk-stained with basic fuchsin to mark the pericellular network and processed for sectioning into 200 micron sections[15]. One volume of interest is identified and imaged as a stack of two-dimensional images, comprising fifty-four transverse plane images ($159 \times 159 \times 0.53$

μm) is obtained (Fig. 2.3) using the laser scanning confocal microscope (SP2 AOBS, Leica Microsystems, Mannheim). The image stack is reconstructed into a digital volume of interest (VOI) containing the pericellular network (Mimics, Materialise Inc., Ann Arbor, MI). Dimensions of the tissue are then scaled up by 1000 times to yield a magnified version of the VOI. A physical model was created by converting the digital model into rapid prototyped scaled physical model.

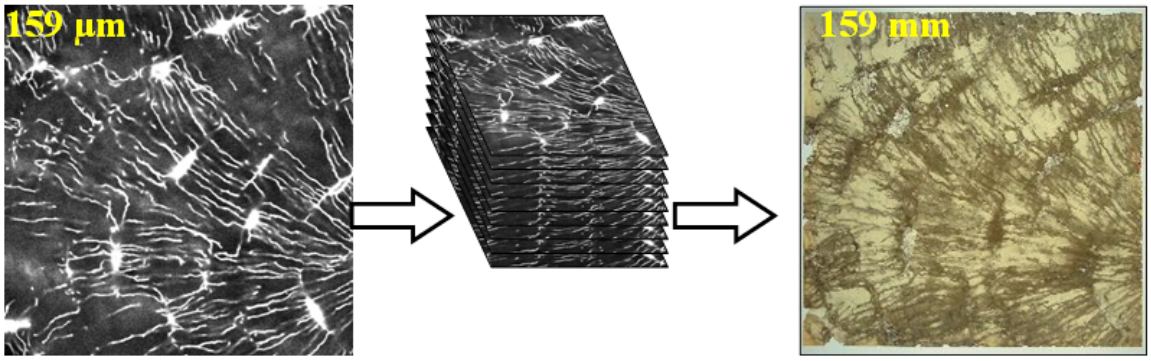

Figure 2.3: Confocal microscope image, bone tissue (black), fluid filled channels: lacuna, canaliculi (white), converted into 54-image stack, 28.5 microns thick (Knothe Tate et al., 2002). Rapid-prototyped scaled-up physical model of lacunocanalicular network (without osteocytes) created from image stack.

A rapid prototyping machine is used to create, layer by layer, a photopolymerized resin block with voids corresponding in geometry and scaled dimension to pericellular channels (159 x 159 x 28.5 mm, Fig. 2.3) (SLA-250, 3D Systems, Valencia, CA). Dimensions of the prototype are compared to the confocal image until the fabricated volume contains anatomically correct pericellular spaces sans the cells and their processes (requiring 3 iterations of the prototype until discrepancies < 5%). It is assumed that the discrepancies in the stereolithography are smaller than that of the confocal image. The matrix microporosity of bone is not included in the scaled up model, because its length scale is on the order of several water molecules, which is below the length scale for continuum fluid mechanics[1].

Permeability measurements in scaled-up, physical models

Permeability of the scaled up physical models is measured in the primary direction of flow. In an osteon, the basic building block of cortical bone, cells and their networks are organized radially from a central pore in which a blood vessel resides. In the physical models, the blood vessel is located along one edge (side) of the physical model; this edge is used as an inlet measuring the permeability of fluids with two different viscosities. The opposite side serves as the outlet for fluid flow. The remaining four sides of the model are sealed to eliminate exiting flow; four acrylic sections enclose these surfaces, with a silicon rubber gasket inserted between the acrylic and bone section to prevent leakage (Fig. 2.4). Furthermore, it is assumed that the interstitial fluid within the pericellular network is similar to that of water. Hence, for the first set of experiments, water is used as the perfusate medium (viscosity = 0.001 kg/m-s). However, in order to maintain Reynolds number in the experimental model, properties of the fluid must be scaled appropriately. For low Reynolds number flow, Navier-Stokes' equations are written as a balance between pressure and viscous effects,

$$\nabla P \approx \mu \nabla^2 V$$

where P is the pressure, μ is viscosity, and V is the velocity vector. Considering pressure induced flow through the tissue section and appropriate scales for pressure, velocity, and dimensions, this is rewritten as

$$\frac{\rho g h}{L} \approx \mu \frac{V}{\varepsilon^2}$$

where ρ is density, g is gravity, h is the pressure head, L is the section length, and ε is a characteristic pore/channel size in the section. Rearranging and substituting for velocity, a Reynolds number relationship is found,

$$V \approx \frac{\rho g h \varepsilon^2}{\mu L} \qquad \mathrm{Re} = \frac{\rho V \varepsilon}{\mu} \qquad \rightarrow \qquad \mathrm{Re} = \frac{\rho^2 g h \varepsilon^3}{L \mu^2} = \frac{\rho P_{inlet} \varepsilon^3}{L \mu^2}$$

For the scaled physical models, if the pressure head, h is held constant while only the solid dimensions of the section (L and ε) are scaled 1000×, then viscosity must also be scaled 1000× to maintain Reynolds number. Thus, in a second set of experiments, silicone oil with 1000× viscosity of water is used to incorporate the scaling factor (balance inertial and viscous forces) into the permeability measurements. Here, a pressure drop adapted from the literature[16] as described below along with a channel radius ε = 0.4mm (see Ch. 3), ρ = 1000 kg/m3, and μ = 1 kg/ms, yields a Reynolds number of 0.00032. For each set of experiments the physical model is filled with the perfusate and a vacuum was applied to the section to achieve complete saturation, thus eliminating surface tension or capillary effects.

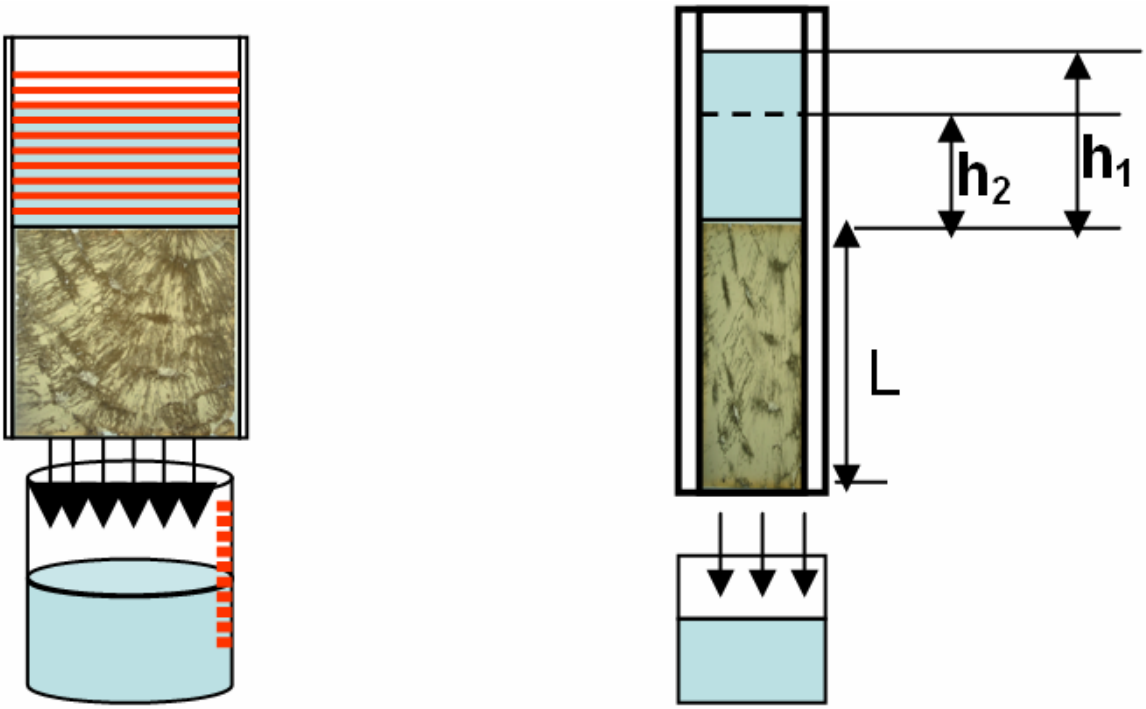

Figure 2.4: (a) Experimental permeability setup for transverse flow under pressure driven conditions, with non-flow surfaces sealed. (b) Falling head permeability setup and measured time interval for given parameters.

By incorporating the scaling coefficient for all variables in the experiment, the pericellular space permeability is determined by scaling down to the cellular length scale the permeabilities measured in the scaled up physical models. Using Darcy's Law, the volume flow rate through a medium, Q, is related to the hydraulic conductivity, κ, area A, fluid height h, and specimen length L, by

$$Q = \frac{\kappa A h}{L}$$

where intrinsic permeability (units of m^2), k, is substituted for hydraulic conductivity using the relationship

$$k = \frac{\kappa \mu}{\rho g} \qquad Q = \frac{k \rho g A h}{L \mu}$$

where μ is viscosity, ρ is fluid density, and g is gravity. If the height of the fluid above the medium is variable, then the volume flow rate can be described by

$$Q = A \frac{dh}{dt}$$

Equating these relations for Q and canceling terms yields an equation for k,

$$k = \frac{L \mu}{\rho g h} \frac{dh}{dt}$$

The integration of the above relation gives

$$k t = \frac{L \mu}{\rho g} \ln(h) + C$$

where $h=h_1$ at $t=0$ and $h=h_2$ at $t=t$, and thus $C = -\frac{L \mu}{\rho g} \ln(h_1)$. Substituting for C and including h_2, an equation for permeability using the falling head form of Darcy's Law is derived,

$$k = \frac{L\,\mu}{t\,\rho\,g} \ln\left(\frac{h_1}{h_2}\right) \quad (1)$$

For the physical specimen, the time taken for the mass of fluid to travel from h_1 to h_2 (h_1 = 0.239 m, h_2 = 0.169 m) is recorded along with section dimensions and fluid properties. The experiment is repeated ten times for both water and silicone oil, and a mean permeability is calculated (using both water and silicone oil). Finally, an uncertainty analysis is carried out for the experimental measurements in order to determine the uncertainty in measured permeability and the individual contributions to the uncertainty for each measured parameter (see Appendix A).

Computational modeling and permeability calculation

In order to validate the order of magnitude of the permeability found in the experimental measurements of the scaled physical model, as well as to predict the influence of cellular and pericellular structures on permeability measurements, four idealized computational models are created and fluid flow is simulated using computational fluid dynamics (*CFD-ACE*, CFDRC, Huntsville, AL) (Fig. 2.5). Models are created for both simple and complex unit cells (lacunae), as well as an interconnected network of cells (lacunar and canalicular cavities). Additionally, the effects of both cellular and pericellular structures on the permeability predictions are investigated via parametric analysis of the simple unit cell (Fig 2.5a). Dimensions of the computational models are based on geometrical values from the literature[16] and are scaled-up (both 100× and 1000×) in order to evaluate the effect of scaling on permeability. All models are created with structured grids, where a parametric study is used to ensure grid independence[16,17]. The resultant mesh densities for the computational models are 6825, 21907, 20475, and 1989607 cells for the models

in Fig. 2.5 (a-d) respectively. A second-order upwind discretization scheme is used for finite volume simulation with a relative iteration convergence criterion of 0.00001. For all simulations, fluid flow is induced via pressure at the inlet and outlet for constant viscosity and steady-state conditions as well as no-slip conditions with completely saturated sections for perfusate mediums of both water and silicone oil (for 100× and 1000× viscosity of water), as used in the experimental measurements. Based on mass and momentum conservation, flow is calculated using continuity and Navier-Stokes equations

$$\nabla \cdot V = 0 \tag{2}$$

$$0 = -\nabla P + \mu \nabla^2 \boldsymbol{V} \tag{3}$$

where V is velocity vector and P is fluid pressure. Since a constant pressure head is applied in the computational models, Darcy's Law can be adapted to determine permeability using the calculated mass flow rate,

$$k = \frac{\dot{m} L \mu}{A P \rho} \tag{4}$$

The scaling factor is then determined from permeability data of the computational models, and an estimate is made for permeability of the original physical specimen by coupling this information with that found in the experimental measurements. The appropriate scaling factor is validated computationally and used to scale the experimental permeability back down the physiologic level; this allow for evaluation of permeability for the pericellular network.

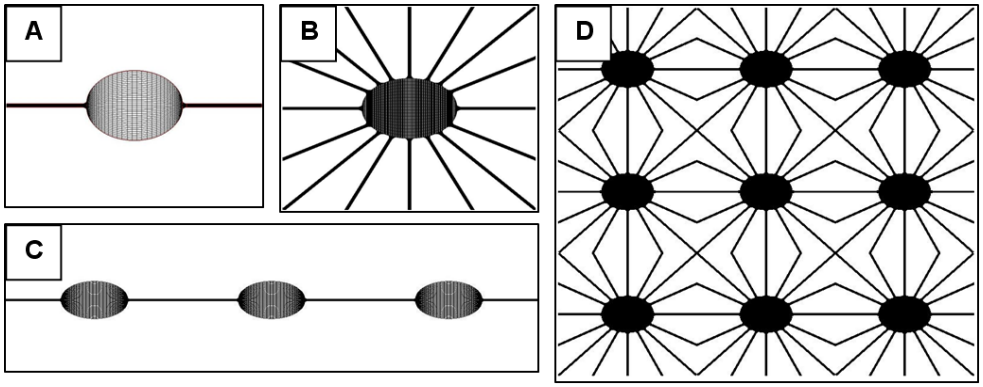

Figure 2.5: Computational models of hollow, idealized lacunocanalicular network geometry used for both 1× and 1000× length scales: (a) simple unit lacuna, (b) complex unit lacuna, (c) simple lacuna network, (d) complex lacuna network.

Of particular interest is the question: how does the presence of cellular structures within the pericellular network affect permeability measurements? Since it is not possible to include these structures in the scaled up physical model of the pericellular network, a computational parametric study is conducted where both cellular and pericellular structures are added sequentially to the hollow unit-cell configuration. The parametric analysis consisted of three configurations representing increasing complexity of cellular and pericellular structures included in the model. This is done by meshing the pericellular and cellular spaces and assigning fluid and/or solid properties to each of two mesh volumes. The first of these, the 'Hollow' arrangement, corresponds to the baseline experimental setup on the pericellular network, in which cellular structures are not accounted for; for this case, both the cellular and pericellular volumes are assigned water-like fluid properties (Fig. 2.2). The second model accounted for inclusion of a cell within the pericellular network as is referred to as 'Filled'; solid, impermeable properties are assigned to the cellular volume of this model, while the pericellular space is treated as in the 'Hollow' arrangement, in which it is assigned the properties of a water-like fluid as well as unrestricted permeability. Finally, the third model accounts for the inclusion of pericellular structure (such as a fluid-filled macromolecular network) in the pericellular

fluid space and is referred to as "PCM" for pericellular matrix; this is implemented by decreasing the permeability of the pericellular space assigned to the "Filled model". The PCM permeability has been predicted previously to be 1.40×10^{-15} m^2 with 25% porosity[18,19]. The current study implements a range of values[1,18,19] from a maximum PCM permeability of 3.30×10^{-15} m^2 and minimum of 2.20×10^{-17} m^2; the porosities implemented range from 12.5% to 50%.

In addition to varying the composition of the two distinct volumes of the unit-cell models, the size of the pericellular space is varied in the parametric analysis to account for potential variation in cell size. To estimate permeability in the presence of cells (cells obstruct up to 65% of the pericellular volume available for flow, which translates to an 80% obstruction in 2D models), a non-dimensional *spacing ratio* is defined as the ratio of the radius of the cell process, where it diverges from the cell body, to the width of the pericellular space at the same point. For a given cell process with an assumed constant radius of 190 nm, and pericellular gaps of 95 nm, 237.5 nm, and 380 nm, respectively (defining the annular space), the resulting spacing ratios are 0.50, 1.25, and 2.00. The spacing ratios are applied as constants along the entire length of the cell process.

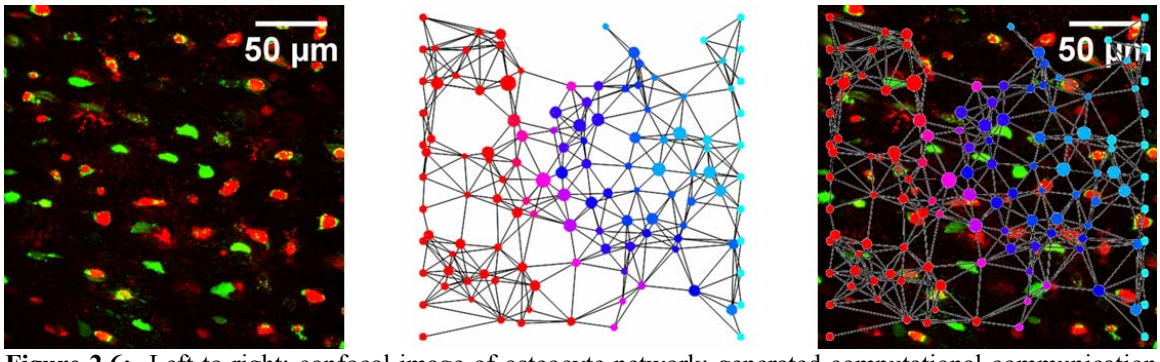

Figure 2.6: Left to right: confocal image of osteocyte network; generated computational communication network between cells; computational network overlay.

Predicting the relationship between connectivity and signal transmission efficiency

Finally, an additional computational network model is built using confocal images (Fig. 2.6) to calculate signaling efficiencies in the pericellular network. Gray scale images are segmented by thresholding at five percent below the maximum intensity value of each respective image. These images are subjected to a particle analysis protocol (NIH ImageJ open source software), where all particles larger than 0.5% and smaller than 4% of the total image area are evaluated and included as data points; these respective areas account for the range of sizes of cells within a cellular network. Using ImageJ, each particle is approximated as an ellipse, and data including the major and minor axis, the total area, and the center of mass of the particle (ellipse, with the respect to the image) is exported to a text file. Then a custom algorithm (written in Mathematica 5.11) is used to create a network of cells (depicted as ellipses connected by lines). Cell volume is calculated by rotating every ellipse in space about its major axis. Another custom algorithm (Mathematica 5.11) is applied to create a cross index of connected osteocytes. Criteria for interface are designed to prevent redundancy and to insure optimal connectivity, resulting in a representation of the cellular network as nodes (cells) interconnected by main transport pathways.

Numerical predictions of transport are made, where diffusive propagation between nodes (cells) is solved discretely over the specified time course of the study. The connections (canaliculi) are generated stochastically between nodes, where for a connection to be generated between two nodes the maximum and minimum allowable distance between nodes is 100 and 25 μm, respectively, for a node diameter of 30 μm.

Convective flow between nodes is solved based on constant internal and external pressures [16] using the analytical pipe flow solution,

$$u = \frac{R^2}{4\mu}\frac{dp}{dz}\left[1-\left(\frac{r}{R}\right)^2\right] \tag{5}$$

where u is axial velocity, R is pipe radius, z is axial coordinate, and r is radial coordinate. Molecular movement is determined as the sum of diffusive and convective propagation, which are added to the current concentration at a given node at each time point (time-step = 0.0001s),

$$\frac{\partial C}{\partial t} + u\frac{\partial C}{\partial z} = D\frac{\partial^2 C}{\partial z^2} \tag{6}$$

where C is concentration, D is diffusion coefficient, and t is time. Initially, concentration is 0, where a step function increases concentration to 100 at one boundary of network. Simulations are run twenty times per data point (total time = 2 ms) based on NO studies. These calculations are repeated in a second step where nodes are randomly removed from the network to simulate loss of connectivity due, *e.g.* to cell death. At the end of the simulation, concentrations are normalized with the "healthy" network, and concentration is depicted graphically as a function of number of nodes removed from the network.

RESULTS

Permeability measurements in scaled-up, physical models

For a scaled-up (1000×), anatomically-correct physical model of the nanoscale network of bone, pericellular permeability in the transverse direction (radially out from an osteon) is experimentally measured for two different fluid viscosities (Fig. 2.7). Using a perfusate of water, the measured mean permeation time is 49.07 s with a standard

deviation of 2.06 s, where the consequent permeability is calculated from (1) to be 1.12 × 10^{-10} m^2 (2.2% uncertainty). Under the same conditions, the 1000× model is tested using viscous silicone oil as the perfusate (1000× viscosity of water) in order to account for the effect of scaling. A mean permeation time of 11,221 s and standard deviation of 78.04 s is measured, and the transverse permeability is calculated to be 2.78 × 10^{-10} m^2 (1.8% uncertainty); a significant change in permeability from measurements carried out with water as the perfusate. For each case, the permeability of the section is found to be independent of the applied pressure head, as suggested by Darcy's Law. However, as noted for water and silicone oil, resultant permeability varies with changing viscosity, albeit within the same order of magnitude.

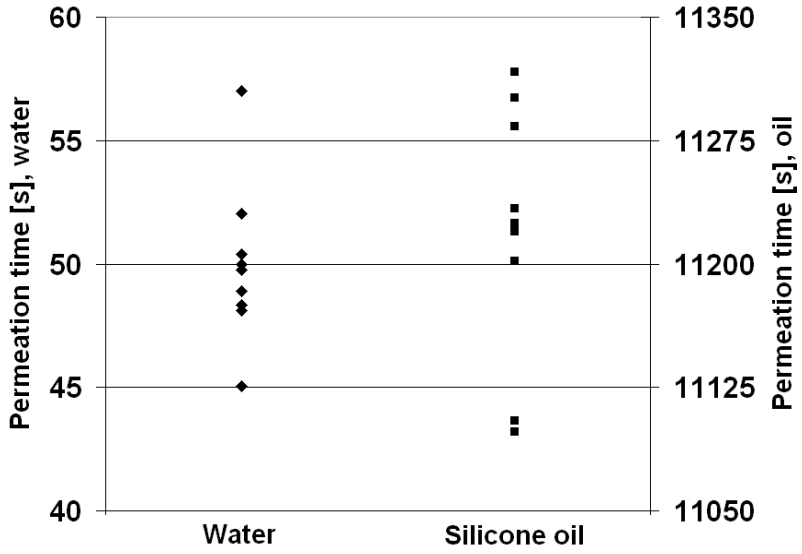

Figure 2.7: Experimental data, mean permeation time for perfusate mediums of water and silicone oil (1000× viscosity of water).

Computational modeling and permeability calculation

When fluid flow is simulated in computational models of similar pericellular geometry as that of the physical model, mass flow rate and corresponding transverse permeability are calculated for four cases (Fig. 2.5). In each case simulations are performed for both water

and silicone-oil and for physiologic dimensions (1×) as well as scaled-up geometries (100×, 1000×). For all models, the calculated permeability is found to increase with the square of the scale factor, regardless of perfusate medium (Table 2.1). Furthermore, the computational models result in permeability within the same order of magnitude as that found in the experimental physical model, where the 1000× scaled geometries yielded permeability on the order of 10^{-10} m^2.

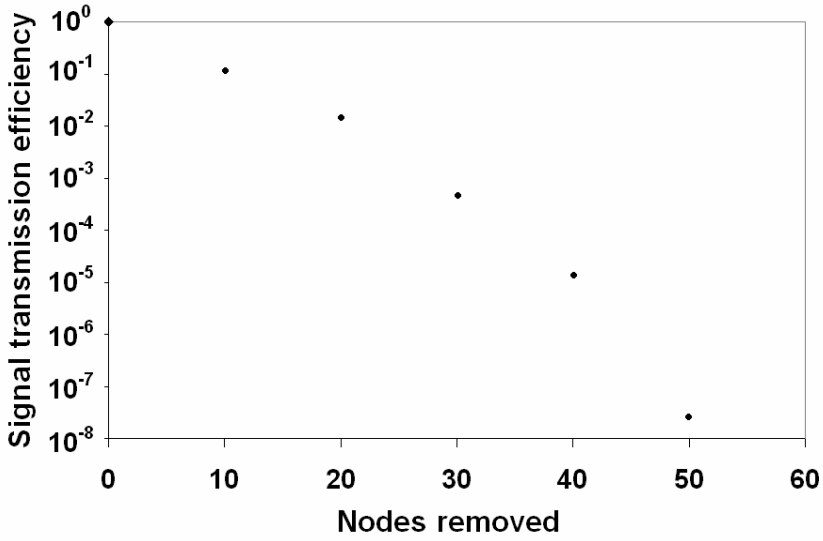

Figure 2.8: Signal transmission efficiency normalized to patent network as a function of removing cells through the bone network. An efficiency of 10^0 or 1 is 100% signal transmission.

	scale	A	B	C	D
water	1×	$1.35\times\mathbf{10^{-16}}$ m^2	$1.37\times\mathbf{10^{-16}}$ m^2	$4.75\times\mathbf{10^{-16}}$ m^2	$4.40\times\mathbf{10^{-16}}$ m^2
	100×	$1.31\times\mathbf{10^{-12}}$ m^2	$1.36\times\mathbf{10^{-12}}$ m^2	$4.74\times\mathbf{10^{-12}}$ m^2	$4.40\times\mathbf{10^{-12}}$ m^2
	1000×	$1.25\times\mathbf{10^{-10}}$ m^2	$1.34\times\mathbf{10^{-10}}$ m^2	$4.65\times\mathbf{10^{-10}}$ m^2	$4.10\times\mathbf{10^{-10}}$ m^2
Silicone oil (w/ scaled μ)	100×	$1.35\times\mathbf{10^{-12}}$ m^2	$1.37\times\mathbf{10^{-12}}$ m^2	$4.75\times\mathbf{10^{-12}}$ m^2	$4.40\times\mathbf{10^{-12}}$ m^2
	1000×	$1.35\times\mathbf{10^{-10}}$ m^2	$1.37\times\mathbf{10^{-10}}$ m^2	$4.75\times\mathbf{10^{-10}}$ m^2	$4.40\times\mathbf{10^{-10}}$ m^2

Table 2.1: Calculated permeability for computational lacunocanalicular models from *Fig. 4*, with varying perfusate μ (viscosity) and dimensional scaling.

For all cases, it is found that the applied pressure head does not influence the resultant permeability for the section, although the variance in viscosity (within a dimensional scale) does have an effect on permeability, as found in the experimental

data. When water is used as the perfusate, a change from the physiologic state (water at 1× scale) is detected with increasing length scale for both the order of magnitude (as expected) and the coefficient (not expected) of permeability. However, when the viscosity of fluid is scaled in proportion to the length scale, as in the silicone oil, the change in permeability is only found in the order of magnitude, coinciding with the square of the scaling factor (1×, 100×, 1000×).

An estimation of permeability for the physical specimen of tissue (1×) can be achieved by taking into account the expected change in permeability due to the effect of scaling. Using the computationally determined scale factor and the mean experimental permeability of the scaled-up (1000×) model with scaled viscosity (1000x), the permeability of the original specimen can be estimated to be 2.78×10^{-16} m^2, where the change in order of magnitude comes from the square of the length scale (1000^2).

Parametric analysis of the unit-cell computational model, accounting for both variations in cellular structure as well as pericellular space, shows a decrease of approximately two orders of magnitude in the predicted permeability when cellular structures are included. For the baseline Spacing Ratio of 1.25, corresponding to a pericellular gap of 237.5 nm, the addition of the cellular structure to the Hollow model causes a reduction in permeability of 84.2%, while the subsequent addition of pericellular obstruction causes a mean decrease of 97.3% from the 'Hollow' configuration. The decrease in permeability associated with mean values of the pericellular matrix are shown to mitigate the effects of the Spacing Ratio. The 'Filled' configuration representing no pericellular obstruction showed a heavy dependence on Spacing Ratio when compared to the 'Hollow' models, ranging from a 73.4% reduction for the largest pericellular gap to a

95.9% reduction for the smallest. In contrast, the reduction associated with the addition of the pericellular (PCM) obstruction ranged from 96.9% to 99.0% when compared to the 'Hollow' models, varying with the properties of the PCM (permeability, porosity).

The computational models allow one to predict experimentally the effect of cellular and subcellular structures on experimentally measured permeability of the pericellular space. Hence, the true permeability of a tissue volume will always be smaller than that measured experimentally on physical specimens not including biological structures that partly obstruct fluid pathways predicted in cases accounting for both the presence of cellular and pericellular structures. For the healthy specimen with an experimental permeability measuring 2.78×10^{-16} m^2, theoretical predictions of permeability that account for the presence of cells albeit not the pericellular matrix decrease by approximately one order of magnitude to 4.40×10^{-17} m^2; if the computational model accounts for the presence of the extracellular (macromolecular) network, the permeability prediction is further reduced an order of magnitude to 7.82×10^{-18} m^2 (Table 2.2). For the case in which the largest pericellular spacing ratio (gap) is modeled, inclusion of the PCM results in a permeability prediction of 8.73×10^{-18} m^2, while the smallest spacing ratio predicts a value on the same order of magnitude, i.e. 2.65×10^{-18} m^2.

Spacing Ratio	Filled	PCM
2.00	7.39×10^{-17} m^2	8.73×10^{-18} m^2
1.25	4.40×10^{-17} m^2	7.82×10^{-18} m^2
0.50	1.13×10^{-17} m^2	2.65×10^{-18} m^2

Table 2.2: Extrapolated permeability values based on the baseline scaled experimental value and the reduction factors derived from the parametric study.

Predicting the relationship between connectivity and signal transmission efficiency

Network signal transmission efficiency decreases with removal of cells; this decrease is exponential when normalized to the output of the equivalent intact cellular network (Fig. 2.8). Furthermore, removal of only ten cells from the network (consisting of > 120 cells initially) reduces its efficiency to 90% of the baseline value. This effect is amplified with removal of increasing numbers of cells, where the rate of decrease in efficiency accelerates on a geometric scale. Efficiency reduces to less than 0.1% when less than 25% of the total cells are removed from the network.

DISCUSSION

A scaled-up (1000×) anatomically-correct physical model of the pericellular network is investigated, where experimental and computational approaches are used to determine the permeability in a volume of porous tissue where direct measurement is impossible. Using experimental data in conjunction with computationally-supported scaling factors, tissue-level permeability in the transverse direction for the scaled-up model is found to be 2.78×10^{-10} m^2, where the permeability of the actual specimen (unscaled) is estimated to be 2.78×10^{-16} m^2. Using the computational analysis for inclusion of cellular and subcellular structures, it is estimated that an intact section (containing cells, etc.) is on the order of 10^{-17} to 10^{-18} m^2. The value of transverse permeability reported in the literature for whole bone is on the order of 10^{-14} m^2 [20,21]. The primary reason for the increase in permeability for whole bone as compared to tissue-level values reported here is attributed to the inclusion of the vasculature, where channel sizes are significantly larger than that

of the nanoscale lacunocanalicular channels. In addition, permeability is expected to be a function of specimen orientation due to the anisotropy of the tissue. However, the transverse direction (in bone) is considered the primary flow direction, as more connections or fluid pathways emanate from cells in this direction and nutrient transport is likely to radiate outward from the vasculature.

In all cases, it is found that in both the experimental and computational analysis, viscosity of the fluid causes the permeability to fluctuate. Experimentally, a significant difference in permeability is found when water is used as the permeating fluid as compared to the silicone oil in the 1000× scaled physical model. This result is also found in the computational models, where differences in permeability due to perfusate medium are detected for all cases. However, if it is assumed that the physiologic state of the pericellular network is considered to be 1× scaling (or unscaled) with a perfusate medium similar to water, it is noted that when the viscosity is scaled with length (as in the silicone oil) permeability changes predictably by an order of magnitude. When water is employed, without scaling viscosity, permeability variance is most likely a result of Reynolds number effects, where imbalances in viscous and inertial forces are introduced.

To address limitations in replicating the impact of physiologically relevant cellular structures in the experimental study, the computational parametric study provides a means to account for the effect of flow obstruction due to cells and their extracellular constituents were included. As expected, the tissue-level permeability shows a strong dependence on the state of the cellular components within the pericellular system, causing a reduction in excess of two orders of magnitude in the predicted values. Depending on the volume percentage of space occupied by the cell, neglecting

extracellular components is predicted to reduce tissue level permeability by a single order of magnitude. Accounting for the pericellular components further obstructs flow, reducing permeability predictions by an additional order of magnitude. Furthermore, it is assumed that deformation of the cell would change the ratio between cellular and pericellular space, causing an insignificant increase in tissue permeability. Interestingly, the predicted dependence of tissue-level permeability on the ratio of the cellular to pericellular space is moderated by the inclusion of these extracellular components. This mitigation may provide cells with a means to moderate flow in their immediate environment, depending on the constituency of their immediate surroundings, as has been suggested by other investigators[24].

An additional limitation arises from the fact that the "leaky" volume of the mineralized bone surrounding the nanofluidic pericellular network has also been excluded; as such fluid penetration through the micropores are not taken into consideration in the scaled physical model. This is due to the fact that the pore size of the leaky volume is less than 10 nm, and thus outside of continuum domain, where scaling-up and measuring flow using classical fluid mechanics would yield inaccurate results. However, due to its small flow-contribution and the fact that cell connectivity can be assessed through pericellular spaces alone, the absence of the microporosity should have little or no bearing on the results of the present studies.

Furthermore, the specificity of the reported permeability to the particular tissue specimens employed in this study also serves as a limitation. It is likely that permeability depends on age, gender, and health status of the specimen measured, because the number and dimensions of fluid pathways (lacunae and canaliculi), channel sizes, tortuosity, and

orientation may vary from specimen to specimen, providing an interesting direction for future studies based on the proposed methodology. However, it is assumed that the specimens utilized in this study are characteristic of healthy human cortical bone and worthy of introducing the proposed methodology; whereas variation in the permeability of this network within other specimens is assumed to be small, the order of magnitude is not expected to change. Interestingly, based on confocal images of osteoporotic tissue, it is expected that connectivity of the osteocyte network is reduced in diseased bone, and thus the permeability would decrease with the onset of disease.

In addition, the geometry of the specimen itself may differ from that of the fabricated scaled-up model due to inherent difficulties in processing "gray" boundaries in the confocal images as well as limitations in resolution of the stereolithography machine. As seen in the confocal images (Fig. 2.3), there is not a definite contrast between the solid (black) and fluid (white) cavities. Thus, an intensity threshold is set to determine the interface between the solid and fluid matrix, where the resulting geometries are compared with physiologic measurements to ensure accurate dimensions of the canalicular and lacunar cavities. However, the resolution of the geometrical dimensions determined through confocal microscopy is not matched by the resolution of the stereolithography, where laser-induced solidification of the liquid resin may result in slight variations in geometry. Nonetheless, the physical model is scaled-up to 1000× that of the original specimen in order to extend beyond this resolution limit, in an effort to render any geometrical variations negligible to the resulting flow. Overall, it is assumed that the reported value of permeability for the hollow pericellular specimen is a high estimate and will represent the upper-limit of physiologic tissue due to the exclusion of

key attributes; other limitations are assumed to be relatively negligible to the bulk-permeability of the tissue-level.

This study has introduced an approach that uses scale-modeling to investigate the fluid environment of the nanoscale pericellular network, and provides experimental measurement as a basis for computational studies. At this level, experimental observations are limited if not impossible, and physiologic geometry is often "lost" in idealized computational models of tissue- and cell-level flow. For the first time to our knowledge, this approach has been employed to measure permeability of this network in an effort to understand fluid parameters at the tissue- and cell-level of bone as well as yield an understanding of connectivity of the osteocyte network using physiologic geometry. Scaled-up physical models of bone tissue can be created relatively quickly and easily, while retaining the complex geometry of the network. Thus, experimental measurements in these physical models in conjunction with computationally-supported data on scaling factors and cellular obstruction can be used to estimate tissue-level permeability in actual specimens of bone as well as to validate computational models.

Overall, permeability is a description of connectivity within a porous tissue where the pericellular space plays an important role in cell signaling, transport, remodeling, and the overall health of the tissue. In particular, permeability of bone tissue can be seen as a measure of osteocyte connectivity and communication. Such an understanding of fluid transport and connectivity in physiologic tissue may aid in improving computational models of this network and serve to predict fluid phenomena in the pericellular space which have yet to be elucidated. Thus, investigating fluid mechanics through scaled

biological tissues holds many important implications for understanding bone physiology as well as advancements in tissue engineering.

ACKNOWLEDGEMENTS

This study has been funded in part by National Institutes of Health and The Whitaker Foundation. The authors would like to acknowledge and thank Dr. Malcolm Cooke for his support in creating the rapid prototype experimental models, and Dr. Joseph Prahl for his comments and suggestions. This investigation was conducted in a facility constructed with support from Research Facilities Improvement Program Grant Number C06 RR12463-01 from the National Center for Research Resources, National Institutes of Health.

REFERENCES

1. Knothe Tate ML, 2003. "Whither flows the fluid in bone?" An osteocyte's perspective. J Biomech 36:1409-1424.

2. Sorkin AM, Dee KC, Knothe Tate ML, 2004. "Culture shock" from the bone cell's perspective: emulating physiological conditions for mechanobiological investigations. Am J Physiol Cell Physiol 287:C1527-1536.

3. Knothe Tate ML, Niederer P, Knothe U, 1998. In vivo tracer transport through the lacunocanalicular system of rat bone in an environment devoid of mechanical loading. Bone 22:107-117.

4. Fleury ME, Boardman KC, Swartz MA, 2006. Autologous morphogen gradients by subtle interstitial flow and matrix interactions. Biophys J 91:113-121.

5. Biot MA, 1941. General theory of three-dimensional consolidation. J Applied Physics 12:155-164.

6. Bridgman P, 1922. Dimensional Analysis. Yale University Press, New Haven.

7. Astarita G, 1997. Dimensional analysis, scaling, and orders of magnitude. Chem Eng Sci 52:4681-4698.

8. Leonardo da Vinci, 1508. Ms. F. In: Johnstone RE, Thring MW (eds.) Pilot plants, models, and scale-up methods in chemical engineering, McGraw-Hill, New York

9. Einstein A, 1911. Elementare betrachtungen ueber die termische molecular bewegungen in festen korpern. Ann Phys 35:679-694.

10. Reynolds O, 1893. An experimental investigation of the circumstances which determine whether the motion of water shall be direct or sinuous, and of the law of resistance in parallel channels. Phil Trans R Soc Lond 174:935-982.

11. Reynolds O, 1895. On the dynamical theory of incompressible viscous fluids and the determination of the criterion. Phil Trans R Soc Lond 186:123-164.

12. Rayleigh L, 1892. On the question of the stability of the flow of fluids. Phil Mag 34:59-70.

13. Rayleigh L, 1904. Fluid friction on even surfaces. Phil Mag 8:66-67.

14. Rayleigh L, 1915. The principle of similitude. Nature 95:66-68.

15. Knothe Tate ML, 2002. Micropathoanatomy of osteoporosis – Indications for a cellular basis of bone disease. Adv Osteoporotic Fract Mgmt 2:9-14.

16. Anderson EJ, Kaliyamoorthy S, Alexander JID, Knothe Tate ML, 2005. Nano-micro scale models of periosteocytic flow show differences in stresses imparted to cell body and processes. Ann Biomed Eng 33:52-62.

17. Anderson EJ, Falls TD, Sorkin AM, Knothe Tate ML, 2006. The imperative for controlled mechanical stresses in unraveling cellular mechanisms of mechanotransduction. Biomed Eng Online 5:27.

18. Weinbaum S, Cowin SC, Zeng Y, 1994. A model for the excitation of osteocytes by mechanical loading-induced bone fluid shear stresses. J Biomech 27:339-360.

19. You L, Cowin SC, Schaffler MB, Weinbaum S, 2001. A model for strain amplification in the actin cytoskeleton of osteocytes due to fluid drag on pericellular matrix. J Biomech 34:1375-1386.

20. Liebschner M, Keller T, 1998. Hydraulic strengthening affects the stiffness and strength of cortical bone. Comp Meth Bioeng 20:761-762.

21. Johnson MW, Chakkalakal DA, Harper RA, Katz JL, 1980. Comparison of the electromechanical effects in wet and dry bone. J Biomech 13:437-442.

22. Cayley G, 1804. Unpublished data.

23. Wenham FH, 1872. Unpublished data.

24. Alexopoulos LG, Setton LA, Guilak F, 2005. The biomechanical role of the chondrocyte pericellular matrix in articular cartilage. Acta Biomater 1:317-325.

CHAPTER 3

Nano-microscale models of periosteocytic flow show differences in stresses imparted to cell body and processes

Eric J. Anderson[1,2], Sathya Kaliyamoorthy[2], J. Iwan D. Alexander[1],
Melissa L. Knothe Tate[1,2,3]

[1]Dept. of Mechanical & Aerospace Engineering, Case Western Reserve University, Cleveland, OH
[2]Orthopaedic Research Center, The Cleveland Clinic Foundation, Cleveland, OH
[3]Dept. of Biomedical Engineering, Case Western Reserve University, Cleveland, OH

Published in *Annals of Biomedical Engineering,* Vol. 33, No. 1, January 2005 pp. 52-62

ABSTRACT

In an effort to understand how local changes in mechanical environment are translated into cellular activity underlying tissue level bone adaptation, flow regimes at small scales such as the osteocytes are explored. Recent developments in computational fluid dynamics (CFD) provide impetus to elucidate periosteocytic flow through development of a nano– microscale model to study local effects of fluid flow on the osteocyte cell body, which contains the cellular organelles, and on the osteocyte processes, which connect the cell to the entire cellular network distributed throughout bone tissue. For each model, fluid flow is induced via a pressure gradient and the velocity profile and wall shear stress at the cell-fluid interface are calculated using a CFD software package designed for nano/micro-electro-mechanical-systems device development. Periosteocytic flow is modeled, taking into consideration the nanoscale dimensions of the annular

channels and the flow pathways of the periosteocytic flow volume, to analyze the local effects of fluid flow on the osteocyte cell body (within the lacuna) and its processes (within the canaliculi). Based on the idealized model presented in this article, the osteocyte cell body is exposed primarily to effects of hydrodynamic pressure and the cell processes (CP) are exposed primarily to fluid shear stress, with highest stress gradients at sites where the process meets the cell body and where two CP link at the gap junction. Hence, this model simulates subcellular effects of fluid flow and suggests, for the first time to our knowledge, major differences in modes of loading between the domain of the cell body and that of the cell process.

INTRODUCTION

Bone is subjected to a dynamic environment in which functional adaptation is necessary for survival of the tissue and, ultimately, of the organism. Bone tissue health depends on the ability of bone cells to recognize and respond to mechanical, electrical and chemical stimuli, a process referred to as mechano-electro-chemical transduction. Remodeling activity, coordinated between osteocytes, osteoclasts, and osteoblasts, provides a basis for adaptation. Osteocytes, the most abundant cells in bone, are actively involved in maintaining the bony matrix, and osteocyte death is often followed by matrix resorption[1] In addition, osteocytes are thought to be mechanosensors[2,3]. Transmission of mechanical signals to the osteocyte cytoskeleton via cell surface receptors can occur directly through the solid matrix structure of the tissue as well as indirectly via fluid pressure and shear stresses imparted by fluid moving through the lacunocanalicular system due to load-

induced fluid flow (see Knothe Tate[4] for recent review). Translation of mechanical signals at the cellular level may further involve triggering of integrin force receptors and/or changes in the conformation of membrane bound proteins that affect membrane fluidity and trafficking. In addition to these mechanical signals, chemical signals, modulated through diffusive, convective and active transport mechanisms, are transported intracellularly as well as through the extracellular fluid in which the cells are immersed.[5] The so-called lacunocanalicular system, or pericellular space, provides an ideal milieu for transfer of exogenous and endogenous signals via mechanical, electrical, and chemical mechanisms. However, the fluid flow regimes that modulate this signal conveyance within the lacunocanalicular system are not understood; this is due in part to difficulty in understanding flow through a nanoscale system of pericellular pathways and to limitations in understanding the morphology and physiology of the osteocytes themselves.

Computational models provide a tool to understand the solid and fluid mechanics within systems that are challenging to study *in situ*. Tissue level computational models of fluid flow through bone have been developed based on Biot's theory of poroelasticity.[3,6-13] Data from tissue level *in vivo* models implicate a relationship between load-induced fluid flow and bone-tissue adaptation.[14] Taken together, computational and experimental models show that mechanical loading modulates local flow distribution and molecular concentration profiles within the tissue.[14,12] Additional tissue level models indicate that local differences in geometry, orientation, and resistance to flow/permeability of flow pathways are likely to modulate interstitial fluid flow distribution and mass transport at the cellular level, providing a means to maintain cell viability and modulate signaling

mechanisms[9,15,16] necessary for advantageous repair and regeneration of tissue throughout the lifecycle of the organism. Although tissue level models are particularly valuable for identifying temporospatial relationships among loading, fluid flow, and functional adaptation (via remodeling) smaller scale models are necessary to elucidate cellular mechanisms underlying the remodeling response.

Cellular level computational models include those calculating flow at the osteonal level[9,15,17-22] down to flow through subcellular regions of the lacunocanalicular system.[17,23,21] Higher order osteonal models suggest that convective transport through pericellular fluid flow augments transport between the blood supply and osteocytes.[9] At smaller scales, subcellular models suggest a key role of the pericellular matrix (PM) as a mechanotransducer, i.e., in transferring mechanical signals from the pericellular fluid to the more rigid structures of the cytoskeleton,[21] and as a molecular sieve with low-pass filter function.[24] Experimental studies show that both the local flow regime, e.g., oscillatory vs. steady flow,[25] as well as the pericellular milieu, e.g., presence or lack of specific molecules in the cell coat (including proteoglycans)[26] or in the cytoskeleton,[27] modulate cell activity associated with fluid flow. Although pericellular flow is likely to affect cellular behavior, actual *in vivo* flow regimes remain a conundrum because they are so difficult to observe and measure *in situ*. Pericellular flow regimes are difficult to understand because osteocytes are remote. Furthermore, the degree to which continuum theory applies at such small length scales is unknown.

In order to begin to understand periosteocytic flow regimes, it is important to understand the geometry, boundaries, and molecular interactions of the region through

which the fluid flows; this region is bounded by the cell and the mineralized extracellular matrix. The osteocyte's immediate pericellular environment has been described as a *Grenzscheide, Lamina Limitans*, or limiting membrane, and consists of proteoglycans, and extravascular fluid.[28,29] This unmineralized area may aid in maintaining the integrity of osteocytes and their processes[28] by serving as a buffer zone to prevent encroachment of mineral into the lacunar space. Increasing mineralization of the pericellular space results in a concomitant narrowing of the periosteocytic "buffer zone." Osteocytes show acid phosphatase activity and other lysosomal hydrolytic enzymes with the capacity to digest proteins and glycosaminoglycans; these are presumed to confer a means to modulate the pericellular buffer zone and to mobilize calcium in the PM.[30] An active role for this pericellular zone in enzymatically controlled depolymerization and repolymerization of proteoglycans has been suggested but not yet proven.[31] Furthermore, osteocytes in culture have the capacity to modulate their extracellular matrix environment through the production of matrix proteins including osteocalcin, osteonectin, and osteopontin; not only would such modulation of the extracellular matrix be expected to result in changes to the biochemical milieu of the cell, but it may also provide a strategy for adaptation of the mechanical environment at a cellular level.[32] Hence, a unique feature of bone matrix is that it mineralizes, which results in the formation of a transport network of least resistance between the blood supply and cells (Fig. 3.1). This pericellular territory is protected from mineralization, providing an efficient conduit for macromolecular transport between cells as well as a cell-specific network for mechanical and chemical signals across the tissue.[33] This flow volume comprises the roughly annular space between the walls of lacunae and canaliculi and the surface of osteocytes and their

processes (postulated dimension 14–100 nm).[34,35] From the cell's perspective, the pericellular flow volume is bounded by the cell coat that is interwoven with the surrounding matrix by linkage proteins including integrins. Furthermore, it is attached

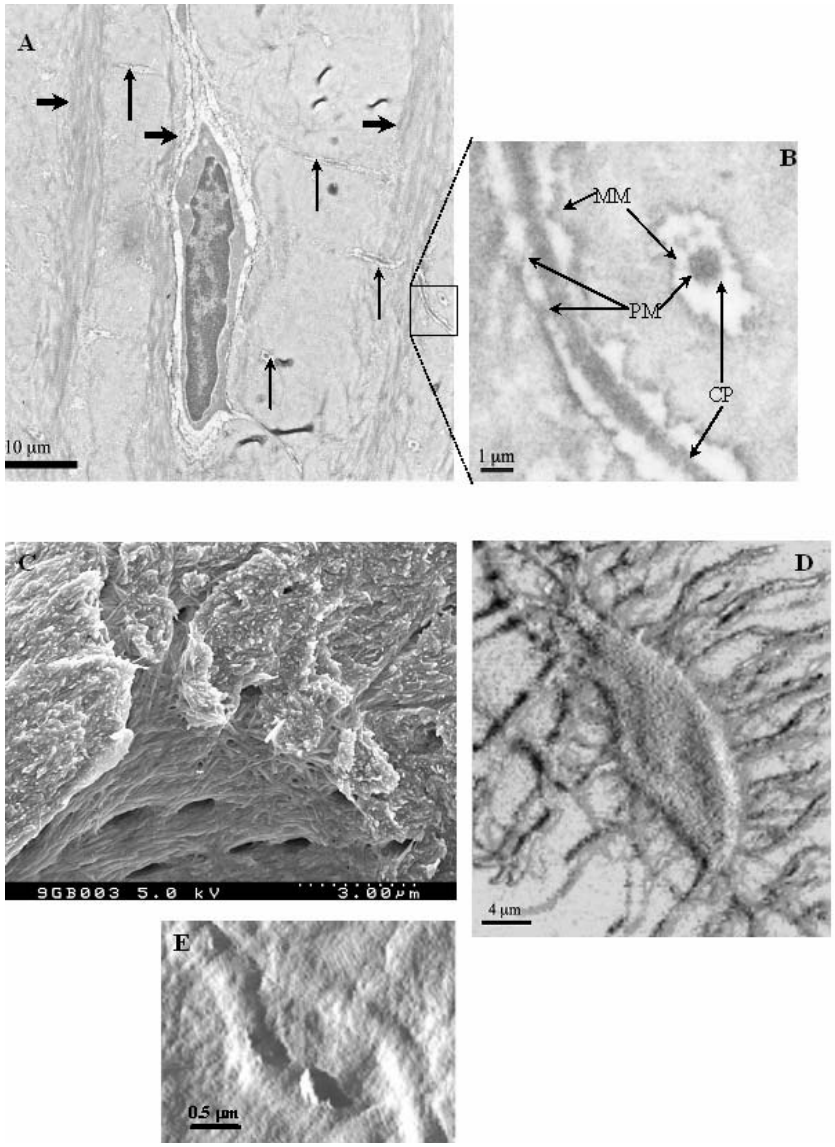

Figure 3.1: The pericellular milieu. **A:** Electron micrograph of a rat metacarpus in cross section showing three osteocyte lacunae in one plane (thick arrows). An osteocyte is present in the middle lacuna and the other two lacunae show the collagenous lining between the surface of the mineralized matrix and the cell; the osteocytes themselves are either further in or out of the section plane. Numerous cell processes extend from cell to cell within the plane and orthogonal to the section plane (thin arrows). **B:** Under further magnification, the undulating, encroaching walls of the mineralized matrix (MM) are visible as is the unmineralized pericellular matrix (PM) and actin bundle filled cell processes (CP). **C:** A scanning electron image of a lacuna with canaliculi extending in and out of the image plane. **D:** A three-dimensional reconstruction of a confocal image stacks showing an osteocyte *in situ* in the tissue of a skeletally mature rat. **E:** Two branches of canaliculi, showing collagen fibrils at the smallest observable length scale.

through cellular adhesion sites to PM molecules. The cells themselves produce enzymes and matrix metalloproteases that play a role in breaking down the PM throughout the lifetime of the cell. The presence of linkages between the cell and its surroundings as well as the capacity to modulate the contents and stiffness of the PM confers the ability to regulate the flow regime around the cell. In short, the pericellular milieu is in constant flux but, for the purpose of computational modeling, can be assumed to be in a relative steady state in times of health. From the perspective of the mineralized matrix (MM), the flow volume is bounded by undulations in the mineralized portion of the matrix, the surface of which is lined with collagen and matrix protein fibers.[36] The space between the cell coat and the lacuna or canaliculus wall is likely to be partially occupied by a molecular network, e.g., of collagens and proteoglycans that influence osmotic pressure and flow conditions *in situ*.

Flow conditions within the annular pericellular space depend not only on the state of the molecular network filling the flow volume but also on the viscosity of the fluid as well as morphological characteristics including the surface roughness of the canalicular wall, the presence of junctions between the cell surface and the canalicular wall and/or fibril networks (e.g., proteoglycans) within the fluid space, as well as physicochemical surface interactions.[37] Based on atomic force microscopy measurements of methyl methacrylate filled casts of the lacunocanalicular system, canaliculi are up to 500–600 nm in diameter. Their wall structure is dominated by collagen fibrils that may be arranged regularly and form ridges spaced approximately 100 nm apart.[36] The canalicular wall is smooth, but the regular dips and ridges caused by the collagen that lines the wall are a source of roughness, which may influence shear stresses imparted by the fluid on

the cell surface as well as mixing of solutes within the lacunocanalicular system. Finally, the collagen lining may affect molecular charge interactions between the fluid and bone matrix.[38,37]

In order to understand the manner in which local changes in mechanical environment are translated into cellular activity underlying tissue level adaptation, fluid behavior needs to be explored at small scales such as the osteocyte. Recent developments in the area of micro and nanofluidics lend themselves for such studies; we have used a computational fluid dynamics (CFD) package designed for nano/microelectro-mechanical-systems device development to model periosteocytic flow, taking into consideration the nanoscale dimensions of the annular channels and the flow pathways of the periosteocytic flow volume, to analyze the local effects of fluid flow on the osteocyte cell body (within the lacuna) and its processes (within the canaliculi).

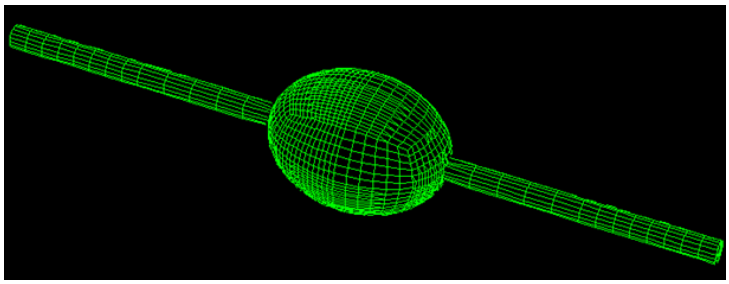

Figure 3.2: Lacunocanalicular mesh with two canaliculi.

METHODS

In order to explore fluid flow at the length scale of the cell, two respective models were developed to study (i) flow regimes within the annular space of a single canaliculus and (ii) within the pericellular space of a lacunocanalicular system including a highly idealized osteocyte and cell processes (CP; Fig. 3.2). Flow through the matrix

microporosity was not included at this stage of modeling. For the single canaliculus model, it was assumed that fluid flows through the nanoscale annular space between the canaliculus wall and the corresponding osteocyte process. A flow regime under these conditions can be idealized as annular pipe flow, which is a common idealization at macroscopic scales. When scaling down to the cellular or subcellular level, for a given pressure gradient, low velocities and, hence, low Reynolds (Re) numbers prevail.[7] For these conditions, flow fields at very low Re numbers are considered laminar with high rates of shear. Nonetheless, a similitude analysis was carried out to determine the effect of annular gap size on the Re number for flow in the nanoscale channels of the lacunocanalicular network with a channel length of 10 μm and a pressure drop of 30 Pa per μm. Based on these principles and dimensional data found in literature,[4] Re was calculated as a function of pericellular gap size for a pericellular gap in the range of 10–1000 nm. Thereafter, computational models of the canaliculus and lacuna were created and implemented to study the nanoscale fluid behavior in the canalicular and lacunocanalicular, pericellular space.

Fluid meshing

A meshing program (Truegrid, XYZ Scientific Applications, Livermore, CA) was used to recreate the canalicular and lacunar geometry as a fluid mesh, where "fluidic blocks" were projected to geometries of dimensions reported in the literature.[29,4,37] The single *canaliculus model* included the geometry of the cell process, canalicular wall and pericellular space, spanning the region between the gap junction (connecting two osteocytes) and the cell body of a single osteocyte, contained within a lacuna (Fig. 3.1a).

This geometry was idealized as a tapered annulus, where the radii of the canaliculus and process increase as they approach the cell body. The annular gap size between the osteocyte process and canalicular wall was defined to be 0.1 μm at the inlet and increasing to 1.5x at the osteocyte cell body, the core diameter was 0.2 μm at the inlet and increased to 1.5x at the cell body, and the channel length was 10 μm, respectively. These dimensions were approximated based on micrograph data.

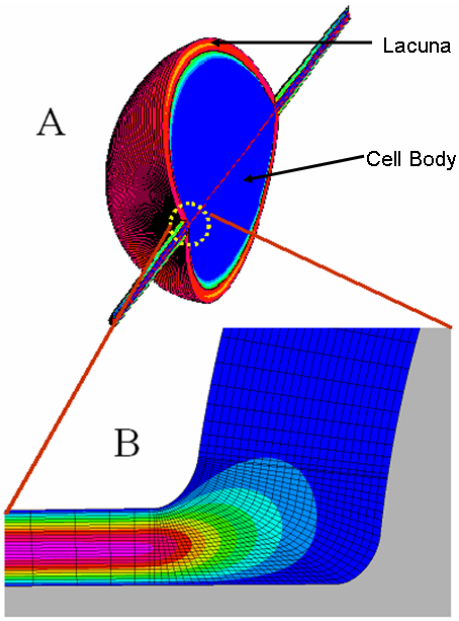

Figure 3.3: (a) CFD simulation of lacunocanalicular model with two canaliculi and (b) mesh density at process/cell body interface.

The *lacunocanalicular model* was idealized in one of three ways, each of which included an ellipsoid lacuna, containing the osteocyte body, and two or more canaliculi that radiated outward from either end of the lacuna (case I-V) or at 90° intervals from the midplane of the lacuna. The lacunar ellipsoid was defined to have a major diameter = 6 μm, and minor diameters of 4 μm, with a gap size = 0.5 μm between the osteocyte and lacuna wall. The dense mesh placed in the gap between the osteocyte and lacuna acts as the fluid volume found within the annular pericellular space, where flow regimes can be simulated under various conditions. The design of this mesh is critical to the simulation

of fluid flow, as the quality of meshing found at the interfaces or boundaries between geometries (e.g., between the lacuna and canaliculi) determines the node locations where each calculation is made and, in addition, sets the conditions for flow continuity (Fig. 3.3b). For this reason, the mesh was created in such a way as to space the nodes evenly within the model, and to ensure smooth transition between geometries. After creation of the model, flow through the pericellular volume was calculated for four cases (see Figs. 3.5–3.8), the simplest of which included two canaliculi that served as an inlet and outlet for flow, respectively. Two variations of this model were implemented where fluid flow was induced across two different axes. In three further iterations of the model, three canaliculi were joined to the lacuna and calculations were run (i) for the case where two canaliculi served as inlets and one as an outlet and (ii) for the case where one canaliculus served as an inlet and two as outlets for fluid flow, as well as a case (iii) where 52 canaliculi were attached to a three-dimensional ellipsoid (6x4x2 μm).

Computational fluid dynamics

Once the mesh for each model was created, a CFD package (CFD-ACE+, CFDRC, Huntsville, AL) was utilized to import the files and to begin the flow simulation process. Flow simulations were based on calculations using the Navier–Stokes equations, assuming conservation of mass and momentum at a minimum annular gap of 100 nm, which has been shown experimentally and in molecular dynamics simulations to be within the continuum domain of classical fluid mechanics.[39] The equations that represent conservation of mass and momentum for an incompressible Newtonian fluid with constant properties are, respectively, given by

$$\frac{\partial u_r}{\partial r} + \frac{u_r}{r} + \frac{\partial u_z}{\partial z} = 0 \tag{1}$$

$$\begin{aligned} 0 &= -\frac{\partial P}{\partial z} + \mu\left[\frac{\partial^2 u_z}{\partial r^2} + \frac{1}{r}\frac{\partial u_z}{\partial r} + \frac{\partial^2 u_z}{\partial z^2}\right] \\ 0 &= -\frac{\partial P}{\partial r} + \mu\left[\frac{\partial^2 u_r}{\partial r^2} + \frac{1}{r}\frac{\partial u_r}{\partial r} - \frac{u_r}{r^2} + \frac{\partial^2 u_r}{\partial z^2}\right] \end{aligned} \tag{2}$$

The simulations were used to calculate velocity components and wall strain rate for each model. From this data, the fluid shear stress at the surface of the process and cell body could be calculated

$$\tau_{wall} = \mu\dot{\gamma} = \textit{wall strain rate} \text{ x } \textit{viscosity} \tag{3}$$

Here u is the velocity, P is the fluid pressure, τ is shear stress, γ is strain rate, z is the axial coordinate, and r is the radial coordinate. In non-axisymmetric models, the continuity and Navier-Stokes equations are modeled in three-dimensions for low-Re flow.

For each model, volume and boundary conditions were specified based on approximations or measurements from the literature.[4] For both the case of the *canaliculus model* and the *lacunocanalicular model*, the interstitial fluid was idealized as water-like and appropriate properties were assigned to the fluid volumes, including density = 993 kg/m^3 and viscosity = 0.000855 kg/m-s. For the osteocyte, material properties were not taken into account, as the body was defined as rigid, where only the fluid shear stresses that would be imparted to the cell surface were calculated. The boundary conditions were then set for the inlet and outlet of each model, where both the *canaliculus* and *lacunocanalicular* models (Fig. 3.3) were assigned an inlet pressure of 300 Pa and an outlet pressure of 150 Pa for the *canaliculus* model and 0 Pa for the *lacunocanalicular* models.[9,10] Velocity conditions at each inlet/outlet were set for annular pipe flow with the

above pressure drop and dimensions. In addition, the grids at the process/cell body interfaces were also given the predicted velocity profile for annular pipe flow as a boundary condition as to ensure continuity and to aid the solver in convergence.

These initial and boundary conditions were applied to each model and calculations for steady flow were carried out, as outlined above, to determine fluid velocity, shear stress, strain, and pressure at each node within each model. These values were depicted graphically in areas of key interest, including the interface between the osteocyte and the surrounding fluid layer as well as the fluid profile within the canaliculi.

Annular gap size (nm)	Max. velocity (m/s)	*Re*
1000	5.848×10^{-4}	6.82×10^{-4}
500	1.462×10^{-4}	8.52×10^{-5}
250	3.655×10^{-5}	1.07×10^{-5}
100	5.858×10^{-6}	6.82×10^{-7}
75	3.289×10^{-6}	2.88×10^{-7}
50	1.462×10^{-6}	8.52×10^{-8}
25	3.655×10^{-7}	1.07×10^{-8}
10	5.848×10^{-6}	6.82×10^{-10}

Table 3.1: Reynolds number for narrow canaliculi containing water.

RESULTS

For the gap size range found within the lacunocanalicular network, e.g., 10–1000 nm, the resulting Reynolds numbers are extremely low (Table 3.1). Thus creeping flow is assumed and gradients of shear are predicted to be very high at the interface between the fluid and the cell surface.

In the *canaliculus model*, the both the pressure and shear stress are found to decrease with increasing annular radius, as expected. Wall shear stress displays a large gradient along the channel length of 10 μm (Fig. 3.4), where values range from 7 to

nearly 1.75 dyn/cm^2 from inlet to outlet. Similarly, the pressure within the canaliculus is found to decrease along the channel, from 300 to 150 Pa, with distance from inlet to outlet, respectively, as governed by the given pressure gradient.

For all cases of the *lacunocanalicular model* the osteocyte surface was subjected to a nearly constant hydrodynamic pressure within the lacuna, with decreased shear stress values as compared to the osteocyte processes. Neither the number of canaliculi nor their designation as inlet or outlet had a significant effect on the qualitative relationship between the hydrodynamic pressures, which exerted a dominant effect, and the shear stresses at the surface of the cell body. However, the models did vary quantitatively, as the hydrodynamic pressure varied as a function of number of canaliculi, respectively, inlets, and outlets.

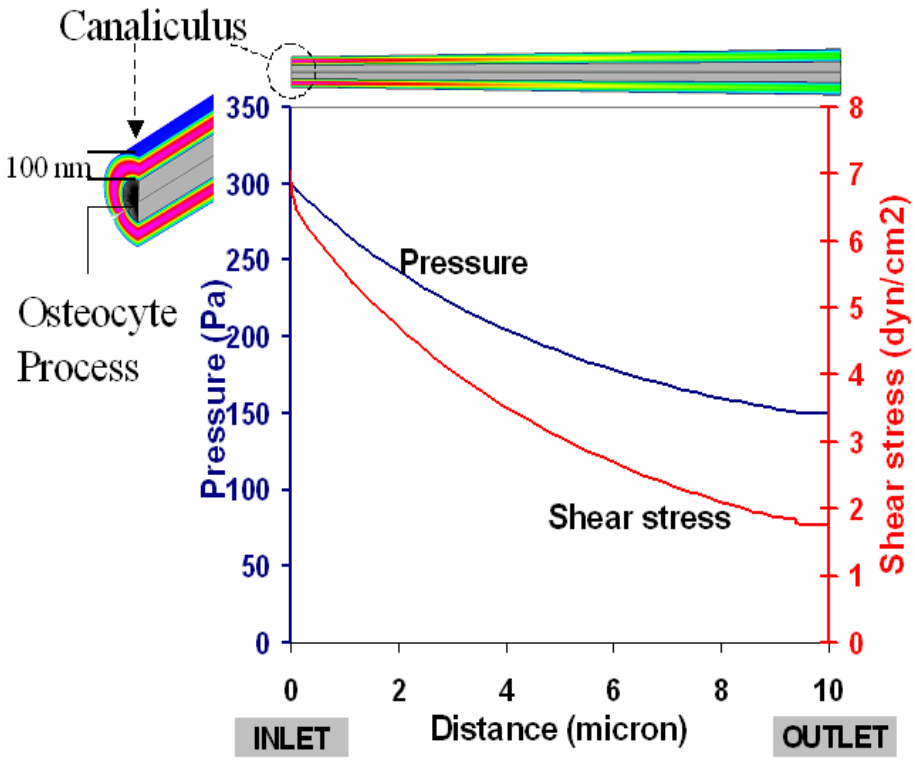

Figure 3.4: Canaliculus model with osteocyte process and annular flow, decreasing gap size with increasing distance from cell body.

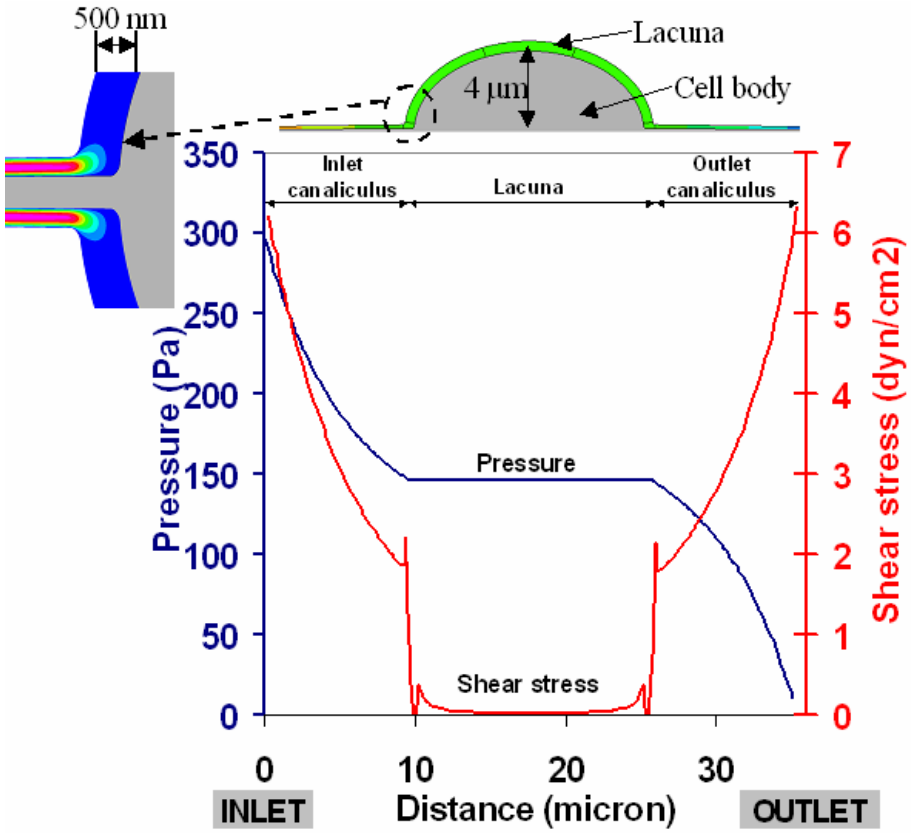

Figure 3.5: Lacunocanalicular model I with osteocyte and two canaliculi.

In comparison with the *canalicular model*, the *lacunocanalicular models* with two canaliculi reveals similar results for fluid flow in each canaliculus; however, the variance in pressure abruptly ceases within the lacuna, where reduced stresses are sustained (Fig. 3.5). As the fluid moves from inlet to outlet, the pressure descends from 300 Pa, as predicted in the first model; however, as the fluid reaches the lacuna, a sustained hydrodynamic pressure (~150 Pa) persists throughout the lacuna. The pressure reduces again upon reentry into the "outlet" canaliculus. The abrupt disruption of flow at the transition zone, i.e., between annular flow of the canaliculus and the lacuna, influences greatly the fluid dynamics within the lacuna and, hence, the surface forces imparted to the osteocyte itself. Furthermore, as the pressure is sustained across the lacuna, the shear stresses decrease to near zero values. Thus, the model does not predict high gradients of

stress along the surface of the osteocyte. From the inlet toward the lacuna, the wall shear stress decreases with pressure as observed in *canaliculus model* described above. However, upon entering the lacuna, shear stress is held at a reduced value until reaching the second canaliculus, at which point it increases with pressure to nearly 6.2 dyn/cm^2 at the outlet.

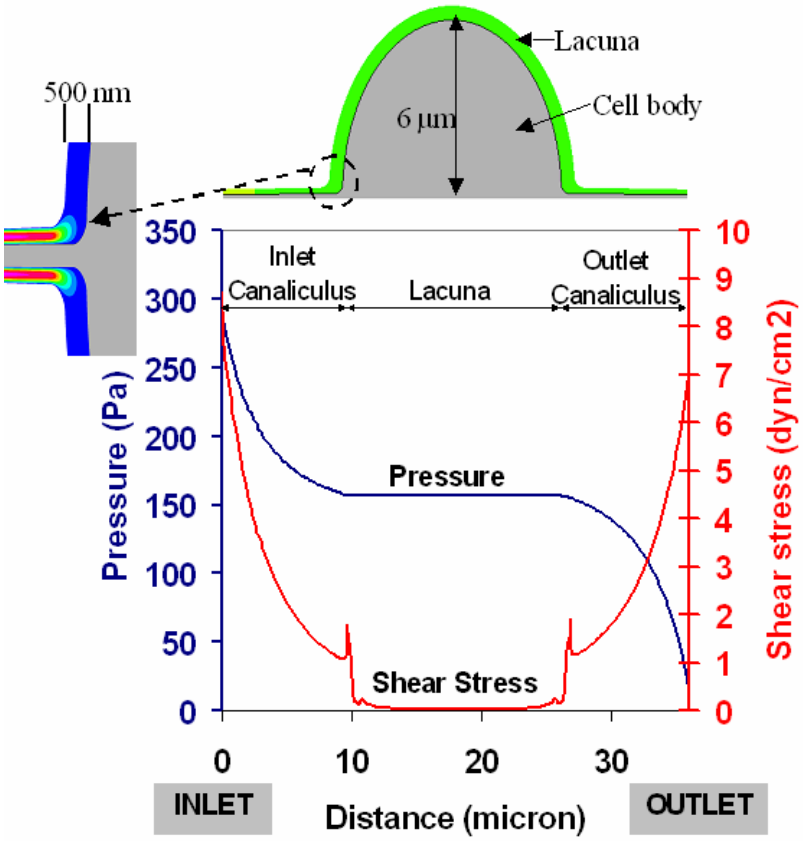

Figure 3.6: Lacunocanalicular model II with flow along perpendicular axis (two canaliculi).

The second version of the two-canaliculi model induced fluid flow across the axis perpendicular to that of the previous model. In this simulation, the resulting pressure and shear stress variations are nearly identical to that of the previous model, where the qualitative relationship between shear stress in the canaliculi and lacuna is found (Fig. 3.6). Magnitudes of fluid shear stress and pressure throughout the fluid-filled gap are also analogous, where a sustained hydrodynamic pressure in the lacuna yields near zero

values of shear stress at the surface of the osteocyte cell body. These similarities are to be expected since the applied pressure gradient, gap sizes, channel lengths, and mass flow rates were identical to that of the previous model.

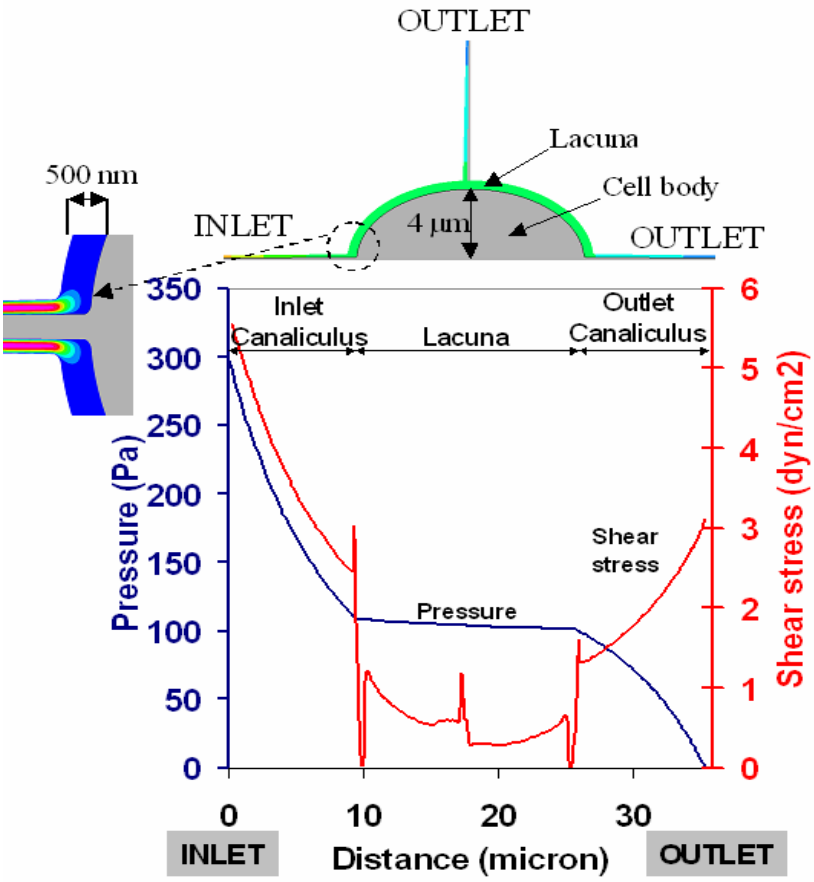

Figure 3.7: Lacunocanalicular model III with one inlet, two outlets.

In the third case of the *lacunocanalicular model*, a third canaliculus was added as an outlet with a pressure of 0 Pa and corresponding mass flow rate (Fig. 3.7). Thus, the CFD was setup as to provide a pressure of 300 Pa across one inlet and two outlets. This simulation produced similar findings as in previous models, where the addition of a canaliculus served as a "sensitivity test" of the model to different geometries. With the addition of an extra outlet, the pressure within the lacuna decreased slightly from that of the previous model, where the chosen pathway was from the inlet canaliculus to the

opposite outlet canaliculus (similar to the previous model), as the chosen pathway shows no difference in the qualitative relationship between the canaliculus and lacuna. In this case, the hydrodynamic pressure within the lacuna is nearly sustained (slight drop across lacuna) at approximately 105 Pa, and the value of shear stress decreases to a reduced value on the osteocyte surface with an exception where the added canaliculus resides. Here, a sharp rise in fluid shear stress is found as fluid escapes through the new channel. This additional canaliculus causes the overall shear stress found within the lacuna to be higher than that of the previous models, where it varies between 0.3 and 1 dyn/cm^2. It can also be noted that the gradient of shear stress in the first half of the lacuna is higher than the second half. This is due to the additional canaliculus, which allows fluid to leave, thus, reducing the pressure, mass flow rate, velocity, and the consequential shear stresses. The flow regime within each canaliculus parallels that found in the *canaliculus model*, where high gradients of stress are present. Furthermore, a disruption of flow in the lacuna parallels that observed in the simple lacunocanalicular model (with two canaliculi).

Analogous to the third lacunocanalicular model, the fourth case of the *lacunocanalicular model* showed a nearly sustained (slight drop throughout lacuna) hydrodynamic pressure within the lacuna with a decrease in wall shear stress at the cell surface (Fig. 3.8). Again, this model was created with the addition of a third canaliculus where the chosen pathway was from the left-most canaliculus to the opposite outlet canaliculus; in this case the new channel was characterized as an inlet with a pressure of 300 Pa. Therefore, simulations were carried out with a pressure gradient across two inlets of flow and one outlet. These results corroborate the previous findings, as the

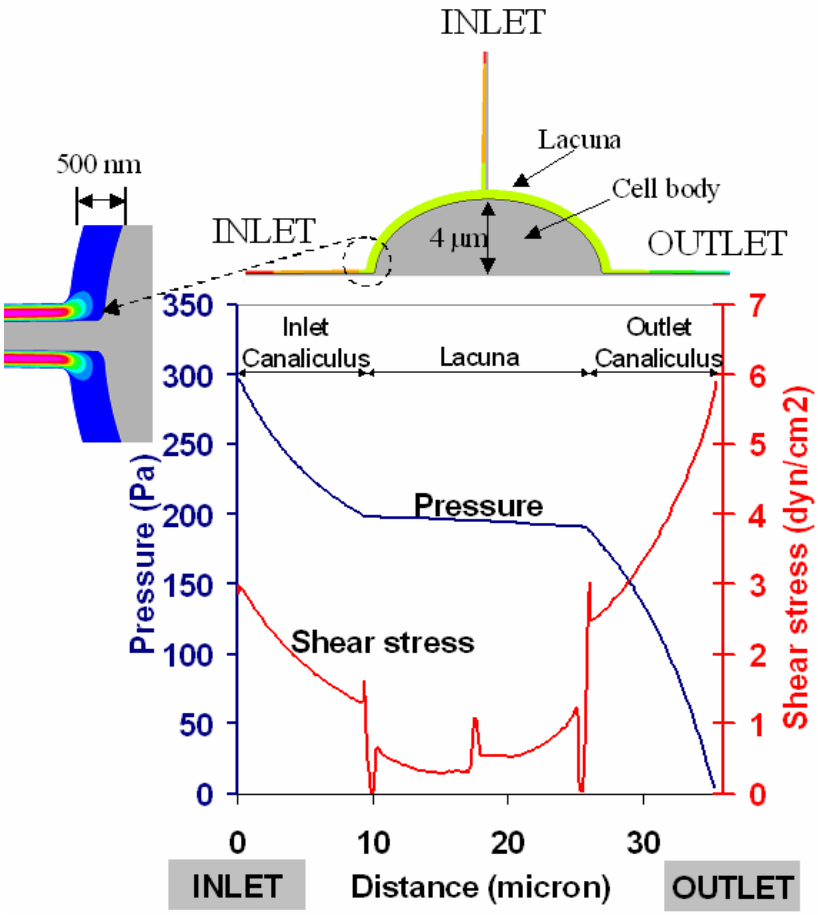

Figure 3.8: Lacunocanalicular model IV with two inlets, one outlet.

hydrodynamic pressure varies slightly between 205 and 195 Pa within the lacuna, and fluid shear stress again sees a sharp rise in the region of the incoming flow from the additional canaliculus. The change in shear stress in the lacuna is opposite to that calculated in the previous case, where a slightly lower gradient of stress is found in the first half of the lacuna, with a higher gradient in the following section. This is to be expected as the added channel introduces flow at this point. This increases the mass flow rate, velocity, and, thus the wall shear stress magnitude at the osteocyte surface. A high gradient of shear stress is again found in the canalicular channels, analogous to the previous lacunocanalicular models.

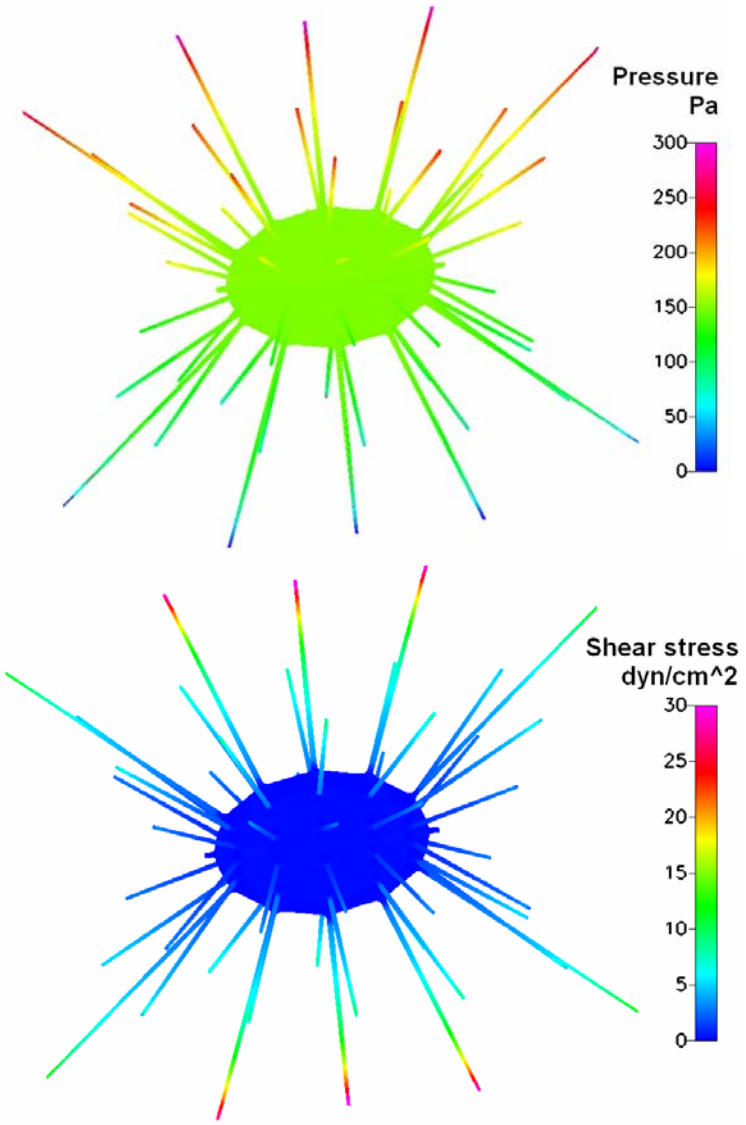

Figure 3.9: 3D multi-canaliculi lacuna model (V), where (top) pressure gradient and (bottom) shear stress on cell are similar to previous models (dyn/cm^2).

Finally, a three-dimensional model containing 52 canaliculi is modeled with the same pressure drop to investigate a physiologic number of cell processes. Here, the pressure gradient is similar to the previous models with a sustained hydrodynamic pressure across the cell body (Fig. 3.9). As a result, the shear stress is again nearly zero across the cell body although there is an increase to 0.4 dyn/cm^2, slightly higher than previous models. Similarly, high gradients of shear stress are found on cell processes, where orientation dictates the specific gradient.

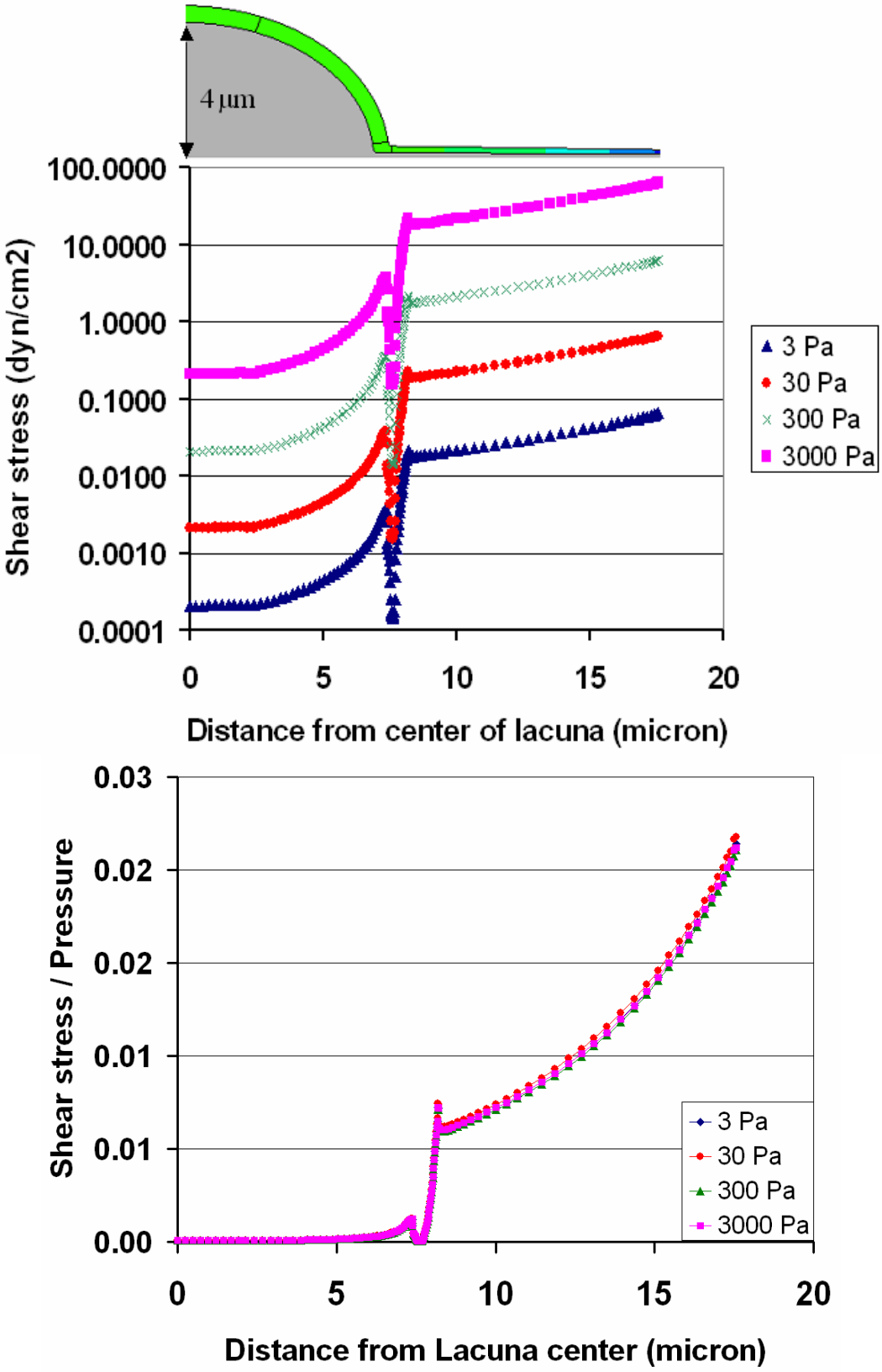

Figure 3.10: (left) Shear stress from center of lacuna through canaliculus, (right) collapsed curve, non-dimensionalized with shear stress divided by pressure.

In order to determine the robustness of the model, the variance in shear stress was determined corresponding to a range of pressures varying by an order of magnitude (3, 30, 300, and 3000 Pa). As in previous cases, the lacuna was subjected to sustained values of stress where high gradients of shear were found to increase with distance from the cell body (Fig. 3.10). The stresses within the lacunae were comparable to the previous models, whereby magnitudes changed proportionally with pressure.

DISCUSSION

Based on the results of this new nano–micro level CFD model of flow through the pericellular space of a single osteocyte, the osteocyte cell body is exposed primarily to effects of hydrodynamic pressure within the lacuna and CP are exposed primarily to shear stresses within the canaliculi, with a local peak in shear stress at the junction between the cell process and cell body. In the *canaliculus model*, where a pressure gradient equal to 150 Pa was applied to a 10 μm channel, the wall shear stress decreases from nearly 7 Pa to 1.8 Pa along the length of the channel. However, in the rigid-body *lacunocanalicular models*, where a single lacuna encapsulating a cell body is attached to canaliculi on either side of its ellipsoidal geometry, fluid flows from the inlet of the first canaliculi, along the radially-expanding channel to the lacuna, where flow is disrupted and forced around the osteocyte body and finally proceeds to exit through the opposite canaliculus. In the entering and exiting canaliculi, the fluid behaves analogous to the fluid in the *canaliculus model*, where pressure and shear stress are proportional to the radius of the annulus. Conversely, within the lacuna itself, fluid shear stresses exerted at the cell surface are nearly constant albeit reduced in magnitude. After decreasing from

the inlet along the length of the canaliculus, the pressure levels off at the junction with the cell within the ellipsoidal geometry of the lacuna cavity. Here, it appears that hydrodynamic pressure is sustained (~150 Pa for one inlet and outlet) throughout the lacuna, thus subjecting the osteocyte cell body primarily to hydrodynamic pressure at the surface.

The predominant loading modes remain the same for the cell body and cell process, regardless of how many canaliculi connect to the lacuna. However, with increasing numbers of canaliculi, the range of pressures and shear stresses imparted to the cell body and processes increases. Furthermore, if the cell were to be treated as a compliant rather than as a rigid body, in a model with multiple canaliculi, the cell would most likely change shape in order to accommodate the locally imparted wall shear stresses.

The size, length and organization of the pericellular channels as well as the mean path distance from the blood supply to osteocytes, appears to be optimized to promote both fluid flow and molecular transport.[18,15] Interestingly, osteocytes may have the capacity to regulate the resistance to flow through the annular channels by modulating the production of PM as described in *in vitro* studies.[32] This may also confer the capacity to control the size of the annular pericellular gap by preventing encroachment of the mineralization front into the pericellular space.[30] Yet the pericellular space associated with the osteocyte body appears much larger than that associated with the osteocyte process. Taken in context with *in vitro* data [40,41] the results of this study provoke examination of the subcellular function of the osteocyte body and osteocyte processes, because it is expected that the plasma membrane of the osteocyte body and osteocyte

processes are subjected to very different flow regimes, and further, the membranes may be divided into functional subdomains to optimize transduction of the specific mechanical signals to which they typically are subjected.

Further, considering that osteocytes are nonmotile cells deriving from motile osteoblasts that, when laying down osteoid, are polarized with apical and basal plasma membranes, one may consider the osteocyte as a polarized cell with distinct plasma membrane domains. While osteoblasts require a cytoskeleton for chemotaxis, entrapped preosteocytes use the same cytoskeletal machinery to extend pseudopodia and CP, thus maintaining orientation and connectivity with cells near the cement line and blood supply, respectively.[42] During transformation of the osteoblast to the nascent osteocyte, CP first radiate toward the mineralizing matrix; these processes are thick and pseudopod-like, and are thought to be involved in the extrusion of calcifying matrix vesicles.[43] Once the mineralization front surrounds the cell, CP of a longer, thinner nature are observed on the vascular side of the cell. These processes bear an uncanny resemblance to dendrites. In the mature state, there is generally more CP oriented toward vascularity than toward the mineralization front.[43] Hence, considering that osteocytes may exhibit specific domain structure much like epithelial and nerve cells, domain specific stress regimes could augment specialization of domains for extracellular signal transmission and regulation of membrane traffic. This postulate can be tested both through further refinement of the CFD model presented here as well as through identification of lipids and proteins in osteoblasts and osteocytes that are targeted to specific domains of, e.g., endothelial, epithelial and nerve cells, since these cells have been shown to use remarkably similar strategies to respond to mechanical forces resulting in functional

adaptation to their dynamic environments.

From a computational perspective, for the postulated dimensional range of the osteocyte and its pericellular space (14 – 100 nm), fluid flow remains within the continuum domain, as supported by simulation down to gaps around 10nm. This could facilitate the use of conservative laws and classical fluid mechanics equations to arrive at analytical solutions. The above solutions were carried out for 100 nm inlet gaps, and thus understood to be within the range of Navier–Stokes equations.[39] However, processes actually branch and become smaller with increasing distance from the cell body, thus the pericellular space also reduces in size. Therefore, the lower bound on the pericellular space does play an important role. However, as the gap size is decreased to 14 nm, solution convergence becomes very difficult, and one must be very attentive to flow and conservation between each interface within the mesh. In this study, we took advantage of CFD software as a tool to calculate flow regimes and imparted stresses for different modeling cases, although it should be noted that a solution at 14 nm is on the very limit of where classical fluid mechanics can be applied.

As with any idealized model, there are certain limitations that should be taken into consideration when interpreting the results. First, the model geometries are highly idealized; in particular they are modeled as a few, smooth, straight channels, whereas physiologically they are numerous, coarse, tortuous, and branching (Fig. 3.1).[29] Secondly, due to the lack of literature on the properties of interstitial fluid, water, a Newtonian fluid was used as the closest match in the simulations. It is expected that bone fluid is slightly more viscous than water, and this is take into account in the simulations. Thirdly, the macromolecular mesh found in the annular gap between

osteocyte process and canalicular wall was not included in the models. Thus, these pathways may be lacking in structures that aid in slowing down or providing resistance to the flow within these spaces. Also, the osteocyte and its processes were defined as rigid-bodies, and thus deformation within each was not taken into account, as this study was designed to study the fluid pathways in the annular gap around these bodies. It can be assumed that deformation will have an influence on the imparted forces, as the cell body would react to the fluid shear stresses presented above in order to change its environment. However, we felt it was important to first analyze the fluid regimes within these spaces before attempting to study their effect on cell-body reaction. Furthermore, the matrix microporosity was not modeled; the presence of this porosity makes the whole system "leaky" to some extent and will relax to a degree the formation of stark pressure gradients. Finally, flow simulation was performed under steady-state conditions, where loading frequencies may have an unperceived affect on the results. Physiologically, we would expect flow regimes to vary with time and load-induced pressure gradients. Thus, these models give insight into the subcellular flow regimes at a specific window defined by a pressure gradient of 300 Pa.

This was a computational study, as observation of fluid flow within the lacunocanalicular network and around osteocytes and their processes is not technically feasible at this time. Scaled and microanatomically correct models are in development to aid in validation of this model for the bone cell network.[44,45] Nonetheless, based on sensitivity analyses these results should hold true for flow regimes on the scale of the cell. Furthermore, refined models including complex networks of cells will allow for the delineation of exact flow regimes under dynamic loading, at the cellular level.

Based on the data from the *canaliculus* and *lacunocanalicular* models, the idealization of annular pipe flow within the canaliculi was appropriate. These models also give insight into the fluid mechanics and type of forces experienced within the lacuna, particularly at the osteocyte surface. The lacuna models with additional canaliculi were also found to yield similar results to that of the two-canaliculi simulation, which serves as a sensitivity test for the simplified geometry. Through this agreement of pressure and stresses within the lacuna cavity, it can be deduced that a more complex geometry of the osteocyte and its processes would yield similar results.

In conclusion, based on this new, nano–microscale CFD model, the osteocyte cell body is exposed primarily to effects of hydrodynamic pressure within the lacuna and the CP are exposed primarily to shear stresses within the canaliculi, with highest gradients in stress between the cell body and the gap junctions to other cells. Hence, this model simulates subcellular level effects of fluid flow and shows, for the first time to our knowledge, major differences in modes of loading between cellular regions remote to (i.e., CP) and near (i.e., cell body) cell-surface receptors and the cytoplasmic domain. This is expected to have profound implications for cell signaling and is being explored in a parallel, experimental study.

ACKNOWLEDGEMENTS

This study is supported through a grant from The National Institutes of Health, National Institute of Arthritis and Musculo Skeletal and Skin Diseases (NIAMS) (AR049351-01). This investigation was conducted in a facility constructed with support from Research

Facilities Improvement Program Grant Number C06 RR12463-01 from the National Center for Research Resources, National Institutes of Health.

REFERENCES

1. Junqueira LC, Carneiro J, Kelley RO, 1995. "Bone, In Basic Histology." Upper Saddle River, NJ: Prentice-Hall, pp. 132-151.

2. Aarden EM, Burger EH, Nijweide PJ, 1994. Function of osteocytes in bone. J Cell Biochem 55:287-299.

3. Burger EH, Klein-Nulend J, Smit TH, 2003. Strain-derived canalicular fluid flow regulates osteoclast activity in a remodelling osteon-a proposal. J Biomech 36:1453-1459.

4. Knothe Tate ML, 2003. "Whither flows the fluid in bone?" An osteocyte's perspective. J Biomech 36:1409-1424.

5. Knothe Tate ML, Adamson JR, Tami AE, Bauer TW, 2004. The osteocyte. Int J Biochem Cell Biol 36:1-8.

6. Biot MA, 1941. General theory of three dimensional consolidation. J Appl Phys 12:155-164.

7. Chin WC, 2001. Computational Rheology for Pipeline and Annular Flow. Woburn: Gulf Professional Publishing, pp. 1-257.

8. Knothe Tate ML, Knothe U, 2000. An ex vivo model to study transport processes and fluid flow in loaded bone. J Biomech 33:247-254.

9. Knothe Tate ML, Niederer P, 1998. Theoretical FE-based model developed to predict the relative contribution of convective and diffusive transport mechanisms for the maintenance of local equilibria within cortical bone. Advances in Heat and Mass Transfer in Biotechnology. 362:133-142

10. Manfredini, P, Cocchetti G, Maier G, Redaelli A, Montevicchi FM, 1999. Poroelastic Finite Element Anasysis of a Bone Specimen Under Cyclic Loading. J Biomech 32:135-144.

11. Steck R, Niederer P, Knothe Tate ML, 2000. A finite difference model of load-induced fluid displacements within bone under mechanical loading. Med Eng Phys 22:117-125.

12. Steck R, Niederer P, Knothe Tate ML, 2003. A finite element analysis for the prediction of load-induced fluid flow and mechanochemical transduction in bone. J Theor Biol 220:249-259.

13. Zhang D, Weinbaum S, Cowin SC, 1998. Estimates of the Peak Pressures in Bone Pore Water. J Biomech Eng 120:697-703.

14. Knothe Tate ML, Steck R, Forwood MR, Niederer P, 2000. In vivo demonstration of load-induced fluid flow in the rat tibia and its potential implications for processes associated with functional adaptation. J Exp Biol 203:2737-2745.

15. Mishra S, Knothe Tate ML, 2003. Effect of lacunocanalicular architecture on hydraulic conductance in bone tissue: Implications for bone health and evolution. Anat Rec 273A:752-762.

16. Tami AE, Nasser P, Verborgt O, Schaffler MB, Knothe Tate ML. 2002. The role of interstitial fluid flow in the remodeling response to fatigue loading. J Bone Miner Res 17:2030-2037.

17. Johnson MW, 1984. Behavior of Fluid in Stressed Bone and Cellular Stimulation. Calcif Tissue Int 36:72-76.

18. Kufahl RH, Saha S, 1990. A Theoretical Model for Stress-Generated Fluid Flow in the Canaliculi-Lacunae Network in Bone Tissue. J Biomech 23:171-180.

19. Mak AFT, Huang DT, Zhang JD, Tong P, 1997. Deformation-induced hierarchical flows and drag forces in bone canaliculi and matrix microporosity. J Biomech 30:11-18.

20. Srinivasan S, Gross TS, 2000. Canalicular fluid flow induced by bending of a long bone. Med Eng Phys 22:127-133.

21. You L, Cowin SC, Schaffler MB, Weinbaum S, 2001. A model for strain amplification in the actin cytoskeleton of osteocytes due to fluid drag on pericellular matrix. J Biomech 34:1375-1386.

22. Zeng Y, Cowin SC, Weinbaum S, 1994. A fiber matrix model for fluid flow and streaming potentials in the canaliculi of an osteon. Ann Biomed Eng 280-292.

23. Weinbaum S, Cowin SC, Zeng Y, 1994. A model for the excitation of osteocytes by mechanical loading-induced bone fluid shear stresses. J Biomech 27:339-360.

24. Tami AE, Schaffler MB, Knothe Tate ML, 2003. Probing the tissue to subcellular level structure underlying bone's molecular sieving function. Biorheology 40:577-590.

25. Jacobs CR, Yellowley CE, Davis BR, Zhou Z, Cimbala JM, Donahue HJ, 1998. Differential effect of steady versus oscillating flow on bone cells. J Biomech 31:969-976.

26. Reilly GC, Haut TR, Yellowley CE, Donahue HJ, Jacobs CR, 2003. Fluid flow induced PGE2 release by bone cells is reduced by glycocalyx degradation whereas calcium signals are not. Biorheology 40:591-603.

27. Ajubi NE, Klein-Nulend J, Alblas MJ, Burger EH, Nijweide PJ, 1999. Signal transduction pathways involved in fluid flow-induced PGE2 production by cultured osteocytes. Am J Physiol 276:E171-E178.

28. Cowin SC, 1999. Bone poroelasticity. J Biomech 32:217-238.

29. Knothe Tate ML, 2001. Mixing mechanisms and net solute transport in bone. Ann Biomed Eng 29:810-811.

30. Baud CA, 1968. Submicroscopic structure and functional aspects of the osteocyte. Clin Orthop 56:227-36.:227-236.

31. Lipp W, 1954. New studies of bone tissues; morphology, histochemistry and the effects of enzymes and hormones on the peripheral autonomic nervous system. Acta Anat (Basel) 22:151-201.

32. Aarden EM, Wassenaar AM, Alblas MJ, Nijweide PJ, 1996. Immunocytochemical demonstration of extracellular matrix proteins in isolated. osteocytes. Histochem Cell Biol 106:495-501.

33. Steck R, Knothe Tate ML, 2005. In silico stochastic network models that emulate the molecular sieving characteristics of bone. Ann Biomed Eng 33:87-94.

34. Cooper RR, Milgram JW, Robinson RA, 1966. Morphology of the osteon. An electron microscopic study. J Bone Joing Surg Am 48:1239-1271.

35. Weinger JM, Holtrop ME, 1974. An ultrastructural study of bone cells: the occurrence of microtubules, microfilaments and tight junctions. Calc Tissue Res 14:15-29.

36. Knapp HF, Reilly GC, Stemmer A, Niederer P, Knothe Tate ML, 2002. Development of preparation methods for and insights obtained from atomic force microscopy of fluid spaces in cortical bone. Scanning 24:25-33.

37. Reilly GC, Knapp HF, Stemmer A, Niederer P, Knothe Tate ML, 2001. Investigation of the morphology of the lacunocanalicular system of cortical bone using atomic force microscopy. Ann Biomed Eng 29:1074-1081.

38. Anderson JC, Eriksson C, 1968. Electrical properties of wet collagen. Nature 218:166-168.

39. Cheng JT, Giordano N, 2002. Fluid flow through nanometer-scale channels. Phys Rev 65:31206.

40. Bhagyalakshmi A, Berthiaume F, Reich M, Frangos JA, 1992. Fluid shear stress stimulates membrane phospholipid metabolism in cultured human endothelial cells. J Vasc Res 29:443-449.

41. Ferraro JT, Daneshmand M, Bizios R, Rizzo V, 2004. Depletion of plasma membrane cholesterol dampens hydrostatic pressure and shear stress-induced mechanotransduction pathways in osteoblast cultures. Am J Physiol Cell Physiol 286:C831-C839.

42. Dudley HR, Spiro D, 1961. The Fine Structure of Bone Cells. J Biophys Biochem Cyto 11:627-649.

43. Palumbo C, 1986. A three-dimensional ultrastructural study of osteoid-osteocytes in the tibia of chick embryos. Cell Tissue Res 246:125-131.

44. Anderson EJ, Knothe Tate ML, 2004. Measuring permeability of bone in the lacunocanalicular network via scaled physical models. Transactions of BMES.

45. Anderson EJ, Knothe Tate ML, 2005. Lacunocanalicular permeability measurements in healthy and osteoporotic patients: An experimental fluid mechanics approach using scaled physical models. Trans ORS 2005, 1126.

CHAPTER 4

Impact of physiologic geometry in predicting forces imparted locally to cells through load-induced fluid flow

Eric J. Anderson[1], Melissa L. Knothe Tate[1,2]

[1]Dept. of Mechanical & Aerospace Engineering, Case Western Reserve University, Cleveland, OH
[2]Dept. of Biomedical Engineering, Case Western Reserve University, Cleveland, OH

To be submitted to the *Journal of Bone and Mineral Research*

ABSTRACT

Computational models have been used to understand flow around an osteocyte, however due to the complex nature of bone, models are often created with idealized geometries. These idealizations of pericellular flow may influence our predictions of the mechanical environment of the osteocyte and potentially may be responsible for the difference in the discrepancy between magnitudes in mechanical cell-stimulation observed between *in vitro* and *in vivo* models. Hence, the purpose of this study is to investigate the impact of physiologic geometry on imparted forces to the cell, and to determine the effects of idealization using computational fluid dynamics analyses on models with physiologic (complex) geometries. High-resolution images from a previous study are used to create 2- and 3-dimensional models of flow through a canaliculus of physiologic and idealized geometries. Computational fluid dynamics is used to calculate the resultant velocity, pressure, and shear stress on the cell surface, and statistical analysis is also carried out to determine the mean and standard deviation of the cell process diameter and fluid gap size

between the process and canalicular wall. It is found that idealization of the canalicular geometry causes a reduction in both magnitude and distribution of shear stress on the cell process. Physiologic protrusions of the mineralized matrix cause localized stress spikes on the cell surface, with values up to 5× the idealized case. Statistical analysis shows that the fluid spacing is highly variable, with mean dimensions similar to values reported in the literature. Overall, inclusion of anatomically-correct subcellular geometries influences the nano-scale flow regimes predicted in bone, where local stresses are likely higher and more variable than previously thought and peak shear stresses approach magnitudes shown to trigger cell activity in *in vitro* models. Thus, physiologic geometry can possibly bridge the gap between *in vivo* and *in vitro* models, and help elucidate the cellular mechanisms of bone adaptation.

INTRODUCTION

Osteocytes are the putative mechanosensors in bone, in which their fluid milieu provides a means for effective transfer of both mechanical and biochemical signals via fluid flow and associated convective transport[1-5]. However, despite the current acceptance of the osteocyte's role in bone biology, we know surprisingly little about the mechanical environment of these cells, which are the most abundant cells in bone. An understanding of mechanisms underlying osteocytes' mechanobiology could provide critical insights into novel therapies for prevention or reversal of pathological changes that occur early in development of bone disease such as disuse, osteopenia, or osteoporosis.

Whereas, the best way to understand the mechanobiological environment of the cell would be to observe the cells *in situ* during physiological activity, experimental

observations of solid and fluid dynamics at the length scale of a mineral-encased osteocyte are limited. Currently, observations of the pericellular fluid environment are not possible with off-the-shelf imaging modalities due to bone's opacity as well as the relative remoteness and pore-size of the periosteocytic annular spacing[6]. Thus, as a countermeasure for *in vivo* experimental limitations, *in vitro* studies and *in vivo* predictive computer models have been employed to explicate the pericellular space and help focus experimental efforts[7-10].

In silico computational models provide a promising platform to elucidate the dynamic fluid environment and underlying mechanisms of mechanotransduction associated with osteocytes. However, even in virtual recreations of the pericellular space, geometrical complexity at the nano- and microscale levels causes model creation and simulation to be both temporally- and computationally-expensive. Thus, as is common in numerical research, the convolution of bone geometry has necessitated idealization of geometries (relative to their physiologic counterparts) used in computational models. Depending on the degree to which actual structures are idealized, this removal or negligence of geometrical divergence in models of bone tissue could affect the range of imparted forces predicted to occur at a subcellular level.

Recently, surface roughness and naturally occurring encroachments (protrusions) of the mineralized matrix, or *lamina limitans,*[11] along the length of the canaliculi have been implicated as critical in determining fluid behavior in the pericellular space[12,13]. Nonetheless, no published study has examined these potentially important effects in a quantitative way. Hence, it is unclear how well these macroscopic, or top-down, highly

idealized computational models predict the physiologic fluid environment at the length scale of a single cell.

Reducing the number or scale of matrix protrusions could potentially alter nano-scale flow regimes and consequently reduce the imparted forces to the cell process. This reduction could play a major role in the paradox found in bone fluid flow between predicted *in vivo* stresses and the necessary *in vitro* stresses for cell stimulation[14]. The mechanical signal required to trigger cell activity above baseline has been shown to be nearly an order of magnitude higher in *in vitro* studies[15-23] than is predicted in *in vivo* models[14,24,10,8]. Thus, the gap that exists between observed and predicted mechanical stimulation or shear stress, may in part be due to geometrical idealizations made at the cellular and subcellular level.

In order to determine what, if any, impact physiologic geometry of the lacunocanalicular network would have on model predictions of the periosteocytic fluid space, this study investigates fluid flow around an osteocyte where geometries are obtained from actual micrographs of bone tissue. High resolution electron micrographs are acquired to model precisely actual osteocyte geometries, and computational fluid dynamics is used to calculate flow in the pericellular space under physiologic loading conditions. Parametric studies are then carried out to elucidate the effect of wall encroachments on model predictions. In addition, microcrack damage to the physiologic geometry is also modeled to investigate its effect on the resulting fluid environment and imparted forces.

A statistical analysis of the micrograph geometries is also performed to investigate variation in the lacunocanalicular dimensions and provide inferences on

possible effects to computational modeling. Measurements of the annular fluid space in the canaliculus as well as the cell process diameter are taken from high resolution micrographs, where their overall variation and dimension determined as a function of location. Observations are then coupled with computational modeling to understand changes in the fluid environment as well as forces imparted to the cell surface.

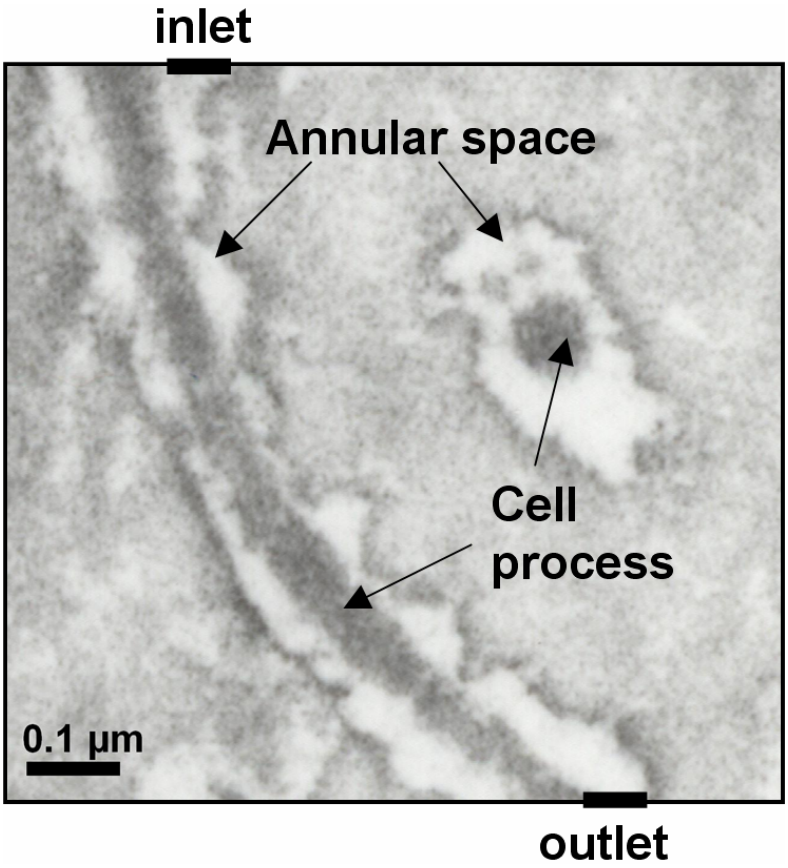

Figure 4.1: TEM image of canaliculus, including cell-process and surrounding matrix microporosity.

Using these computational models of flow through locally-complex geometries, in conjunction with the knowledge of how these structures vary on a global-complexity, a reduced set of models is utilized to describe the impact of physiology geometry on predicting load-induced fluid dynamics at the level of the osteocyte. Thus, this study provides a quantitative analysis of the importance of physiologic geometry in pericellular

flow, as well as allows the accuracy of idealized model predictions from previous studies to be assessed. Improvements in our understanding of the osteocyte's fluid environment and that of mechanotransduction, enhances our ability to develop treatments for prevention and reversal of bone disease through healing and maintenance of overall bone health.

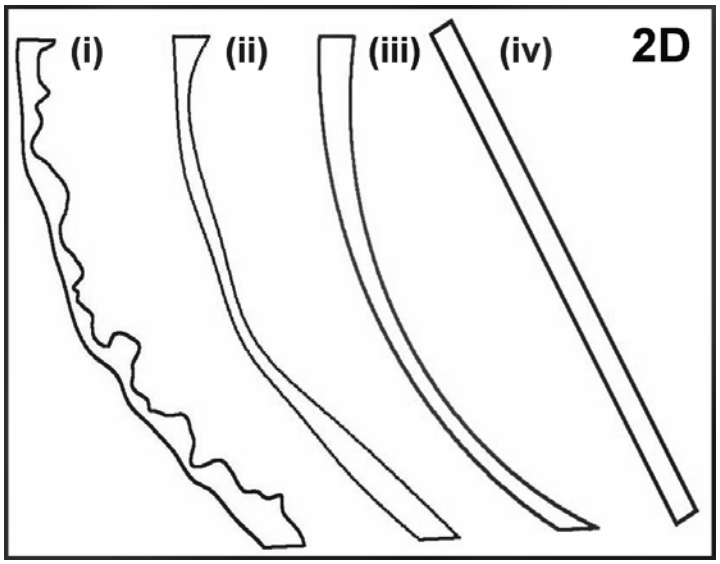

Figure 4.2: Computational models of pericellular space for (i) physiologic geometry, (ii) smoothed canalicular wall, (iii) arc-function wall, and (iv) completely-idealized straight channel.

METHODS

In order to investigate the complex geometry in the pericellular space and create complex models of canalicular flow, high resolution imaging of the pericellular network was carried out using transmitted electron microscopy (TEM). For the canalicular geometry analysis, specimens were taken from the rat femora of three different animals, where gender, age, and pathology were controlled to reduce sample variance. Following sample harvest each received one of three fixation methods (mpb8, mpb7, kpb7), and TEM images were acquired at five magnification levels. Each micrograph containing at least

one canaliculus and cell process is used for the statistical analysis, where only the best representative image is exported for fluid simulation.

Using an image containing the subcellular complexity of a canaliculus, as this is predicted to be an area of increased shear stress[8], computational models are built to simulate load-induced flow and elucidate the effect of idealization on the fluid environment (Fig. 4.1). In order to investigate the effects of idealization, four variations of the geometry are created to represent "stepped" changes from a physiologic state to a highly-idealized model (Fig. 4.2a-d). The first case is considered to be similar to the perceived physiologic state, where encroachments of the mineralized canalicular wall are included in detail, and the nodal mesh is created by tracing the micrograph geometry. In a second model, idealization is introduced through smoothing the rough canalicular wall. Here, a polynomial function is used to create a "smoothed" geometry from a series of points taken along the complex mineralized matrix. As a result, only two elongated protrusions are created along the wall of the canaliculus. Subsequently, in the third case, the wall is reduced to three points consisting of the inlet, midpoint, and outlet that are used to create an "arc" wall profile, yielding a completely smooth wall and an even higher level of idealization. Finally, the most highly-idealized case is created as a straight channel representing the canalicular and process walls, where the channel spacing is taken as an average of the physiologic dimensions and varied from 0.05 μm to 0.1 μm to estimate ranges in imparted forces. Nodal meshes for each model variation consisted of a structured grid and were adapted systematically until solutions are found to be grid independent. For the four canalicular models (Fig. 4.2a-d), node densities are 18557, 4776, 11976, and 171 respectively.

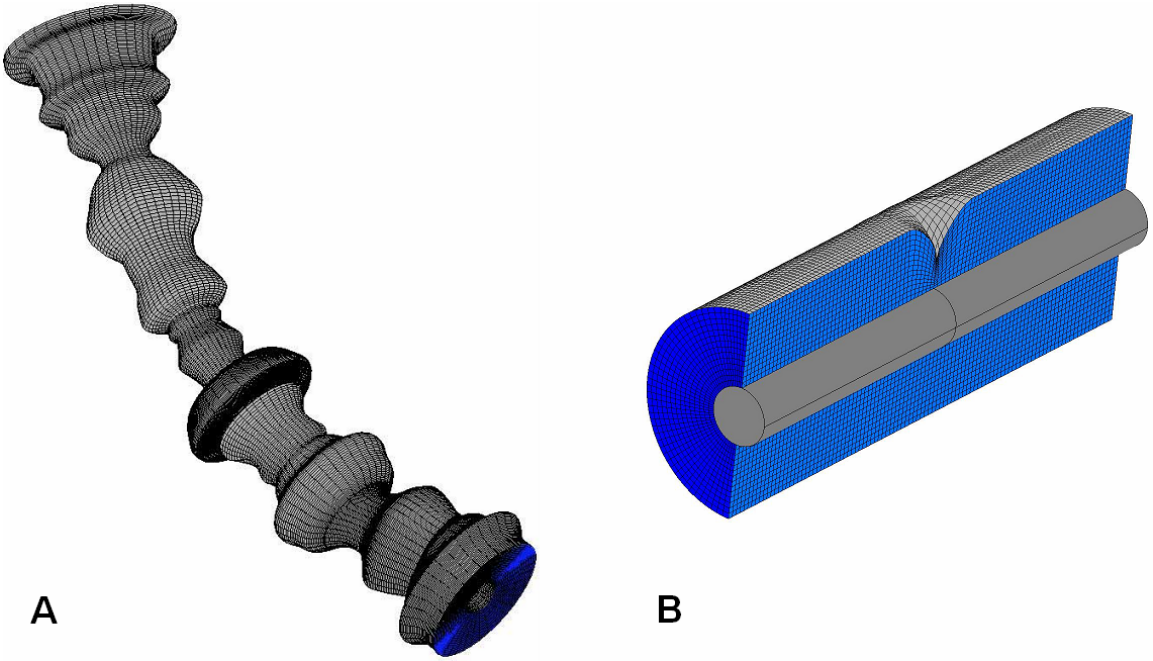

Figure 4.3: Three-dimensional models of pericellular space: (a) axisymmetric physiologic geometry, (b) non-axisymmetric geometry containing a single protrusion point.

Since the lacunocanalicular geometry is inherently three-dimensional, supplemental models are also created with both axisymmetric and non-axisymmetric geometries in three dimensions. However, current imaging capabilities do not allow for three-dimensional images of the sub-canalicular geometry at the required resolution, and thus as a first approximation, the two-dimensional physiologic geometry is revolved about the process axis creating an axisymmetric geometry (Fig. 4.3). This idealized model allows for the quantification of the third-dimension as a supplement to the previous models from above. However, it is expected that the canalicular geometry is not axisymmetric, as protrusions from the canalicular wall are variable and non-uniform. Thus, an annular model with a non-axisymmetric single-protrusion point is created in three-dimensions to investigate flow around non-uniform geometry. Although, protrusion dimensions are thought to be variable, only one specific geometry is modeled, providing a supplemental qualitative understanding of non-uniform protrusions.

The physiologic geometry of damaged bone is also modeled, where microcrack dimensions are based on a previous study[25], and the opening of the crack is on the order of the annular gap spacing. Here, the TEM image of physiologic geometry is again used; however a microcrack is inserted into the geometry and serves a discontinuity in the canalicular wall (Fig. 4.4). The process length is identical to the previous cases, however the relative placement of the mineralized matrix and protrusions are shifted due to the insertion of the microcrack. It is expected that the microcrack is orthogonal to the canalicular geometry, however in two-dimensions, it serves as a flow sink.

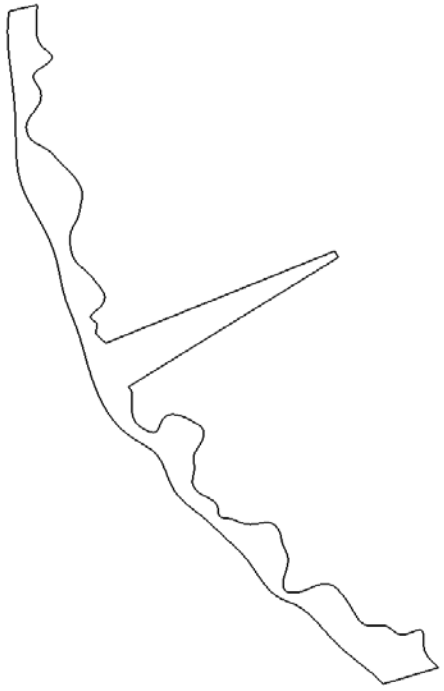

Figure 4.4: Physiologic model with included microcrack geometry.

In all cases, simulations of canalicular flow were obtained using a 2nd-order finite-volume method (CFD-ACE, Huntsville, AL), where the continuity (1) and low-Reynolds (Re<<1) Navier-Stokes' equations (2) in two dimensions were solved for each model,

$$\nabla \cdot V = 0 \tag{1}$$

$$0 = -\nabla P + \mu \nabla^2 V \tag{2}$$

where V is the velocity vector, P is local fluid pressure, and μ is viscosity. Since pressure gradients at the level of the canaliculus are oscillating and encompass a range of values[8], dimensionless variables are used to describe pressure, velocity, and shear stress, where a general solution is found regardless of physiologic load. Defining the following dimensionless variables and substituting into (1, 2), scales for pressure, velocity and shear stress are found for an arbitrary pressure at the inlet (assuming outlet pressure is set to zero),

$$P^* = \frac{P}{\mathrm{P}} \qquad u^* = \frac{u}{U} \qquad x^* = \frac{x}{L} \qquad y^* = \frac{y}{D} \qquad v^* = \frac{v\,L}{U\,D}$$

$$0 = -\frac{\mathrm{P}}{L}\frac{\partial P^*}{\partial x^*} + \mu\frac{U}{L^2}\left[\frac{\partial^2 u^*}{\partial x^{*2}} + \frac{L^2}{D^2}\frac{\partial^2 u^*}{\partial y^{*2}}\right]$$

$$0 = -\frac{\mathrm{P}}{D}\frac{\partial P^*}{\partial y^*} + \mu\frac{UD}{L}\left[\frac{1}{L^2}\frac{\partial^2 v^*}{\partial x^{*2}} + \frac{1}{D^2}\frac{\partial^2 v^*}{\partial y^{*2}}\right]$$

$$U = \frac{\mathrm{P}\,D^2}{\mu L} \qquad \frac{\partial P^*}{\partial y^*} = 0$$

$$u^* = \frac{\mu L}{\mathrm{P}\,D^2}u \qquad v^* = \frac{\mu\,L^2}{\mathrm{P}\,D^3}v \qquad P^* = \frac{P}{\mathrm{P}} \qquad \tau^* = \frac{\tau}{\mathrm{P}}\left(\frac{L}{D}\right)$$

where u is axial velocity, v is transverse velocity, x is axial dimension, y is transverse dimension, U is maximum transverse velocity, L = 1.3μm is axial length of model, D = 0.082μm is inlet height of model, P is applied inlet pressure, τ is wall shear stress on cell process. Using pressure-induced flow, boundary conditions at the inlet and outlet for dimensionless pressure are given as 1 and 0, respectively, and the no-slip velocity condition is instituted at the canalicular and process walls. The fluid medium is assumed to be slightly more viscous than water at 310K (ρ = 993 kg/m^3, μ = 0.001 kg/ms), although the set viscosity only affects the dimensionless velocities, not the wall shear stress (see scales above). All structures are considered to be rigid or non-deforming, and

fluid shear stress on the process wall is calculated as the product of laminar viscosity and wall strain rate. Conservation of mass and momentum are satisfied as solutions are found to converge to a criterion of 0.00001 in each case.

A Statistical analysis is also carried out using the TEM micrographs in order to understand variation in canalicular and process diameters, and consequently the annular fluid spacing (See Appendix B). Using imaging software (OpenLab 4.0.3), electronic measurements of the process diameter and annular-fluid spacing at the same locations are recorded in 0.1 μm intervals where possible. In addition, where applicable, measurements are also recorded as a function of distance from the cell body to yield possible inferences about variation along process length. In all cases, parameters are recorded as a function of animal (1-3), fixation (1-3), and magnification (1-5) for a total of 16 images. Measurements are exported for analysis of variance (ANOVA) testing. Specifically, the analysis was carried out to determine: (1) variance of the annular-gap size in the pericellular network; (2) variance in process diameter; (3) variance of annular-gap size with process diameter; and (4) process diameter and annular-gap size as a function of distance from the cell body.

RESULTS

In the two-dimensional models created from TEM micrographs, the effects of idealization on predictions of the mechanical environment are profound. Simplifying pericellular geometry from a physiologic to highly-idealized state yields a step-wise reduction in both the variance and magnitude of shear stress imparted to the cell process surface. In the

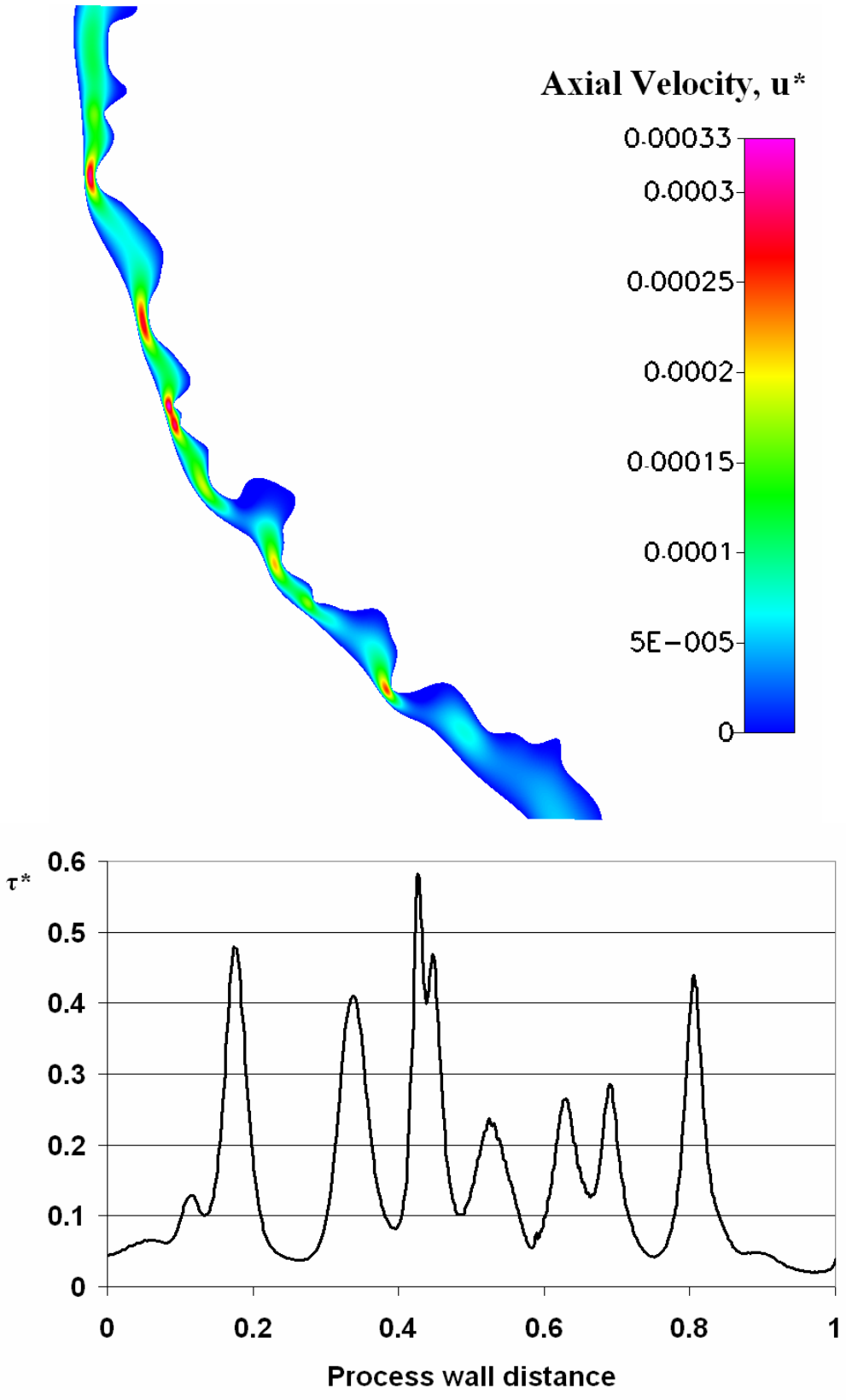

Figure 4.5: Physiologic model: non-dimensional (top) axial velocity, and (bottom) shear stress on cell process surface from inlet to outlet (top to bottom). High variation in shear stress due to protrusions.

physiologic model, where anatomical geometry is traced from the actual micrograph, a perturbed pressure gradient is found in the pericellular space where matrix protrusions cause sharp increases in the magnitude of axial velocity due to continuity (Fig. 4.5). In correspondence to location of these protrusions, and the velocity increases, the shear stress imparted to the cell surface is highly variable and reaches a maximum point or spike up to 0.58, where the variability in the canalicular wall geometry yields seven spikes in shear stress (Fig. 4.5).

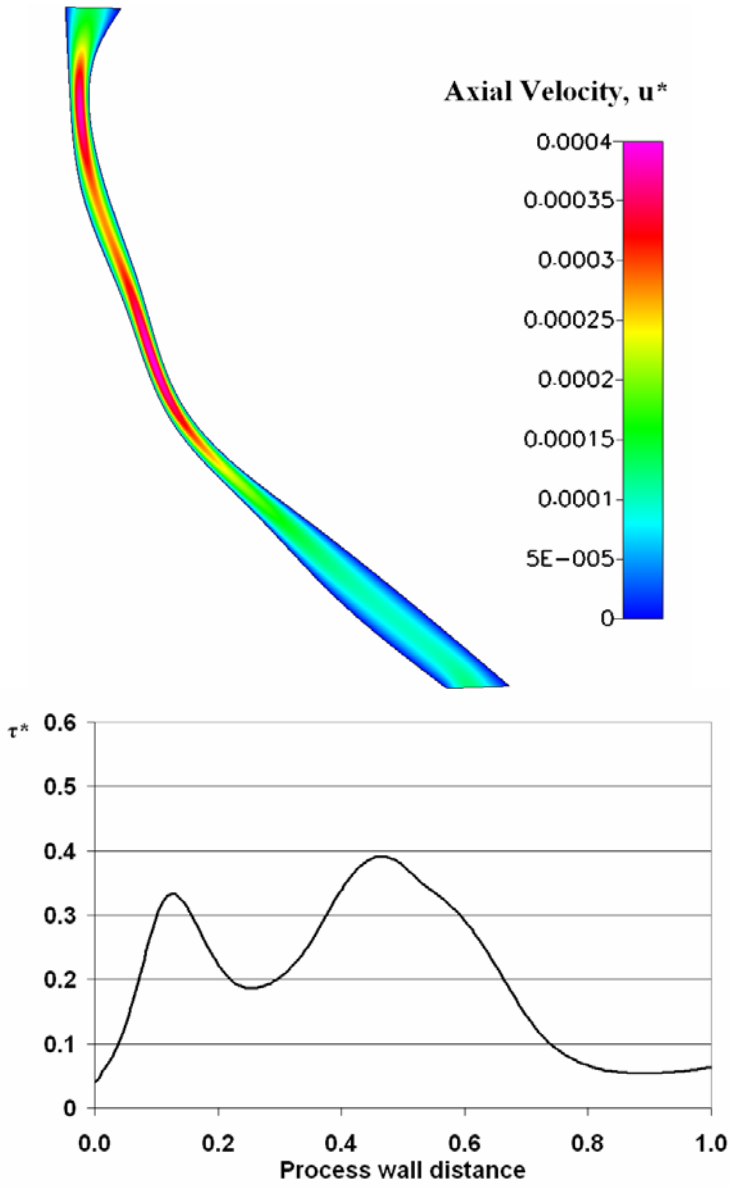

Figure 4.6: Smoothed model: non-dimensional (top) axial velocity, and (bottom) shear stress on cell process surface from inlet to outlet (top to bottom). Reduced stress magnitude and variation.

In the first step of idealization, with the smoothed canalicular wall, the magnitude and variance of shear stress on the cell process is reduced from the physiologic case (Fig. 4.6). Two elongated protrusions of the smoothed wall cause only two increases in velocity and thus only two spikes in the stress along the process wall. Also, because the manipulation of the pericellular space increases the gap between the cell surface and mineralized matrix (*lamina limitans*), the magnitude of shear stress at the spikes is also reduced from 0.58 (physiologic) to 0.39 (smoothed).

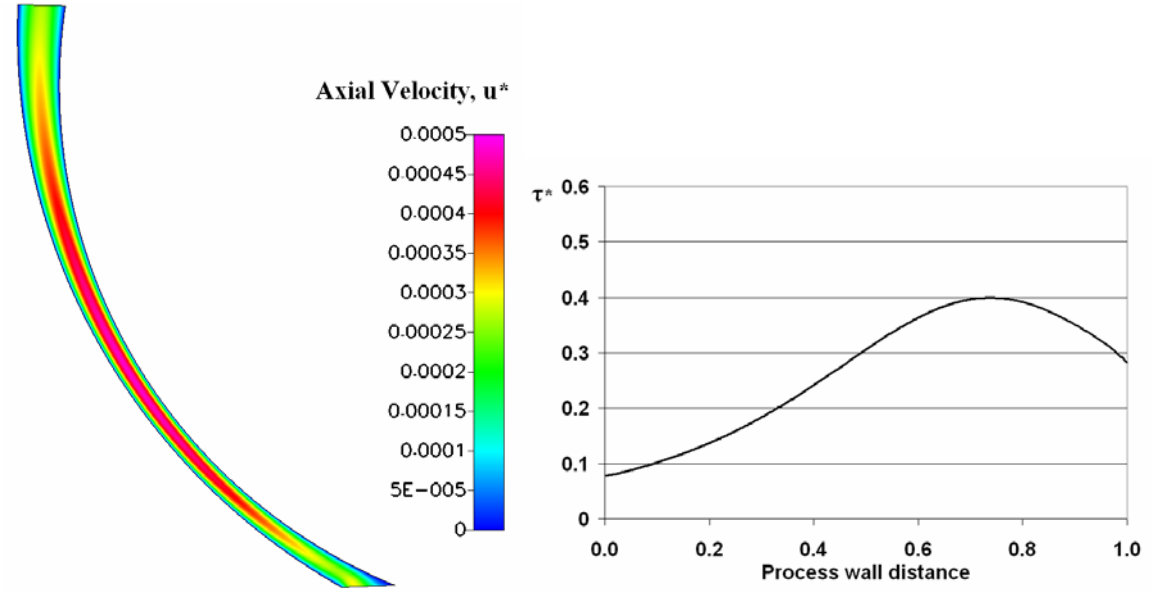

Figure 4.7: Arc model: non-dimensional (left) axial velocity, and (right) shear stress on cell process surface from inlet to outlet (top to bottom). Reduced stress variation, similar magnitude to smoothed model.

Using an arc function for the canalicular wall in the next step of idealization, matrix protrusions are dissipated and the spikes in shear stress on the cell surface are eliminated (Fig. 4.7). The arced-wall causes an increase in velocity near the middle to second-half of the model, where the reduction in gap size between the process and matrix near the model outlet yields a single peak in stress of 0.40. Although the magnitude is similar to the previous model, the variation or stress spikes are reduced to zero.

In the completely idealized case, a straight channel yields a total loss in variation with a constant shear stress along the process wall, where the magnitude depends on the chosen gap size between the process and mineralized matrix (Fig. 4.8). Without the variation in axial geometry, the velocity profile is constant along the pericellular space, and thus the shear stress imparted to the cell surface is constant. A range of gap sizes (0.05 -0.1μm) yields a band of possible constant shear stress between 0.3 and 0.6.

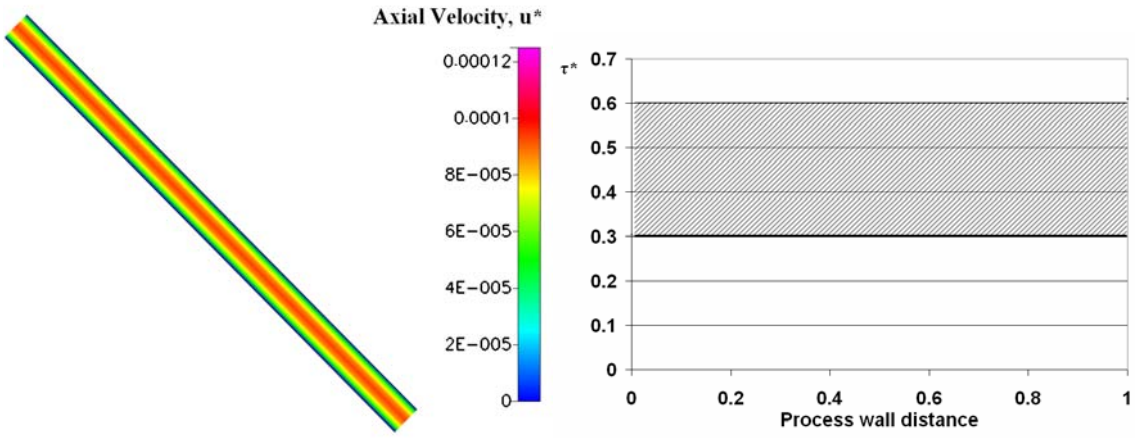

Figure 4.8: Complete idealization, straight channel model: non-dimensional (left) axial velocity, and (right) constant shear stress on cell process surface from inlet to outlet for a range of pericellular spacings. Complete loss of stress variation, possible loss of peak magnitudes.

In an axisymmetric three-dimensional model of the physiologic geometry, the added dimension results in similar but amplified profiles of velocity and shear stress. Along the same plane as in the two-dimensional case, the axial velocity is analogous, with increases corresponding to each protrusion (Fig. 4.9a). Consequently, the shear stress imparted to the cell process wall is similar, where three-dimensional variance along the surface is found (Fig. 4.9b). Comparing profiles from the same plane of wall shear stress in the two- and three-dimensional models, the added dimension amplifies the imparted stress up to 2x that of the previous case (Fig. 4.9c). The maximum stress spike magnitude increases from 0.58 to 0.77 in the axisymmetric geometry.

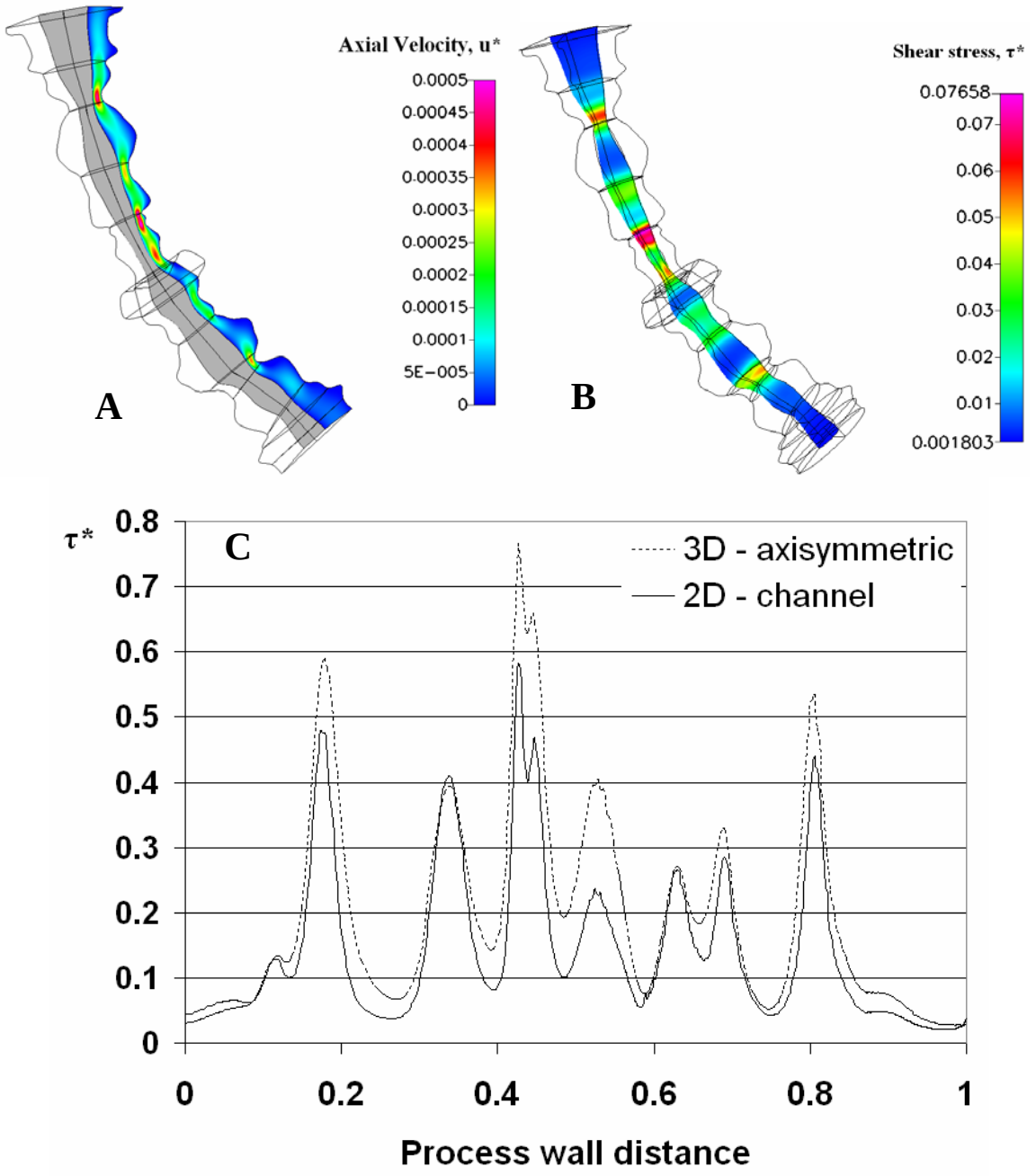

Figure 4.9: 3D axisymmetric physiologic model: non-dimensional (a) axial velocity, (b) shear stress on cell process surface, (c) comparison plot of two- and three-dimensional shear stress.

However, in the non-axisymmetric three-dimensional case, fluid is allowed to flow around the single protrusion point contrary to previous models. Following the path of least resistance, the fluid moves around the matrix protrusion where the axial velocity beneath the protrusion decreases while the transverse and radial velocities increase due to

continuity (Fig. 4.10a-c). Although, with the reduction gap size at the protrusion location, the derivative of velocity still increases at this point, and thus the shear stress on the process wall spikes directly below the protrusion point (Fig. 4.10-11). Interestingly, shear stress along the axial direction is also found to drop from baseline immediately before the protrusion, thus adding to the relative increase in magnitude at the stress spike (Fig. 4.11).

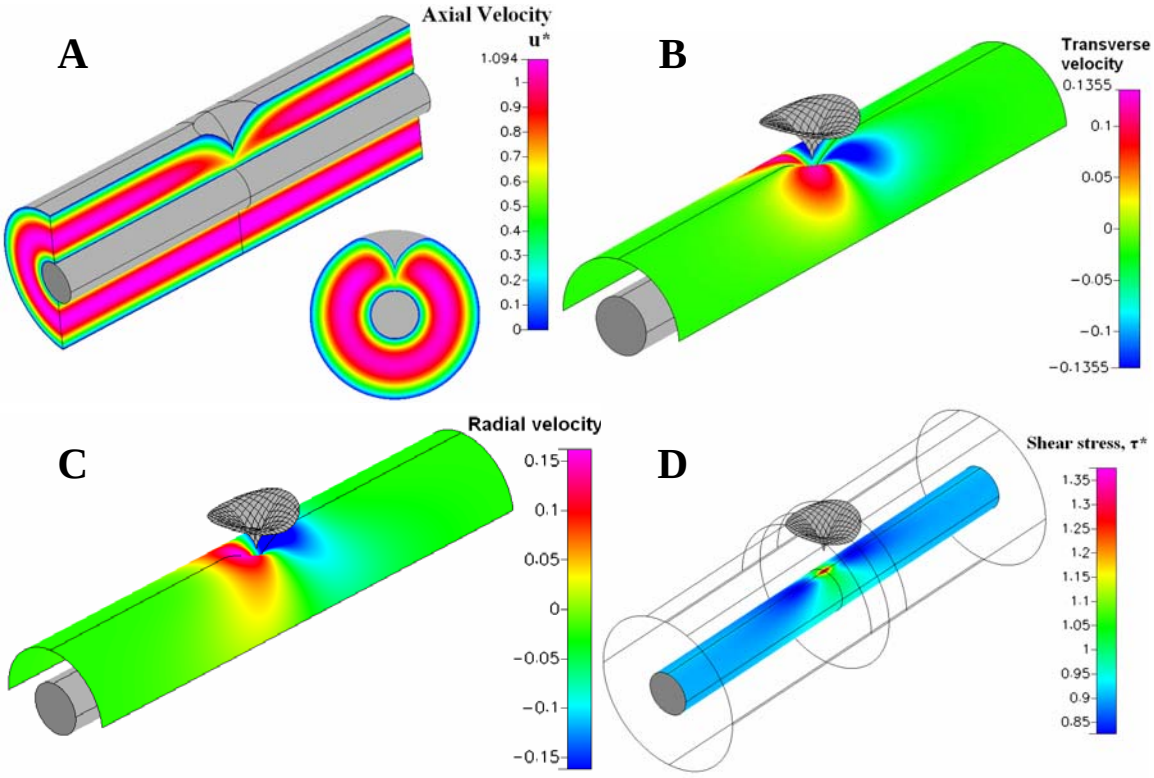

Figure 4.10: 3D non-axisymmetric model, with single protrusion: non-dimensional (a) axial velocity, (b) transverse velocity, (c) radial velocity all scaled with maximum velocity of 3.28×10^{-5} m/s, (d) shear stress on process wall.

Including microcrack geometry in the physiologic model, the axial velocity decreases at the crack location (Fig. 4.12). As a result, the shear stress on the process surface decreases at the corresponding location. However, due to shifting of the mineralized matrix and protrusions, the stress profile along the cell surface is shifted as well. Depending on the ending protrusion location, the wall shear stress is found to

increase or decrease relative to the normal physiologic model, where in this case increases in magnitude are found up to 0.8 (Fig. 4.12).

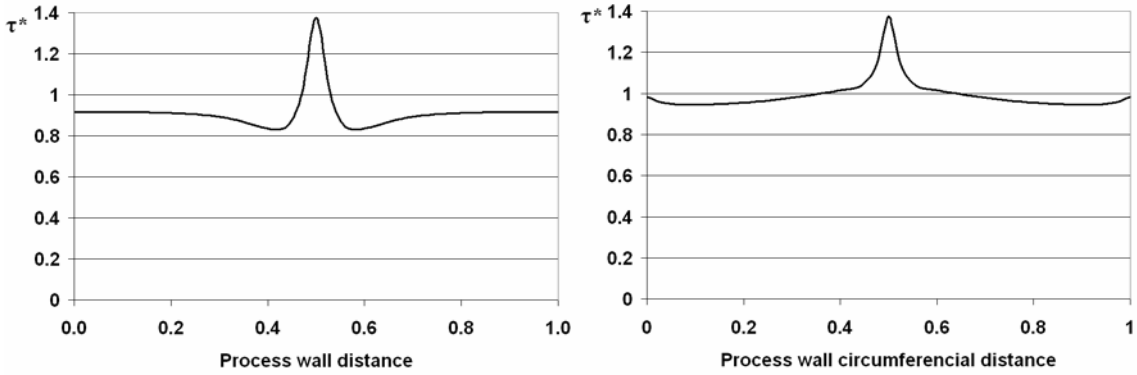

Figure 4.11: (left) Shear stress on cell-process surface, (right) plots of shear stress along (top) axial and (bottom) circumferential directions.

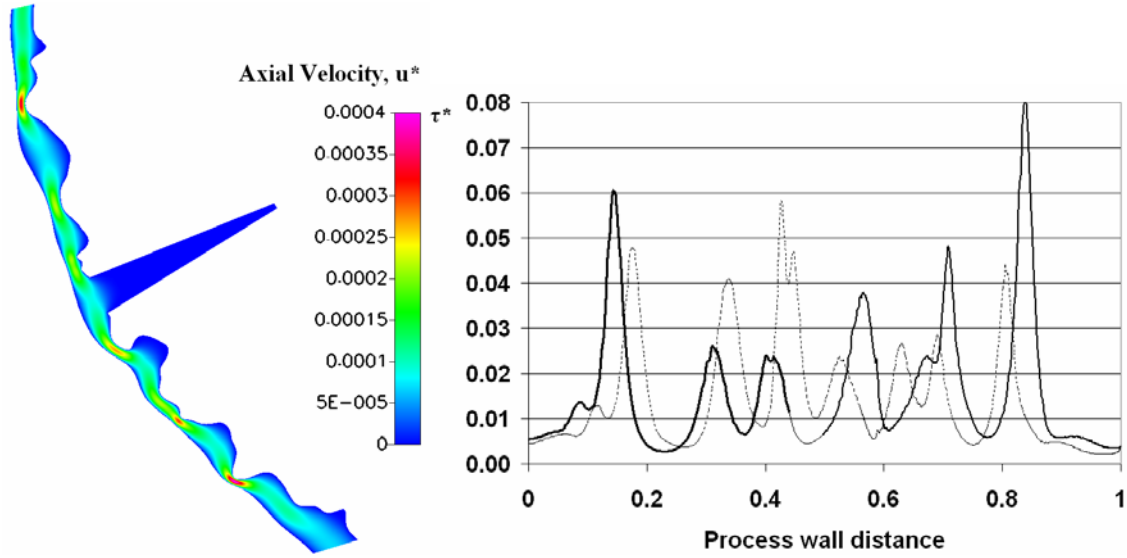

Figure 4.12: Microcrack-physiologic geometry: non-dimensional (left) axial velocity, and (right) shear stress on process surface, comparison with healthy physiologic model. Shear stress profile due to microcrack is shifted with the protrusion locations, as a result peak stresses increase and decrease; stress at the microcrack decreases.

Statistical analysis of the physiologic geometry shows that both the pericellular space between the process wall and the mineralized matrix as well as the cell process diameter are highly variable, similar to geometry of the physiologic model. Based on sixteen images, the pericellular space has a mean gap size of 0.131 μm with standard deviation of 0.056 μm. In addition, the mean cell-process diameter is found to be 0.099

μm and standard deviation of 0.029 μm. ANOVA testing shows that the dimensions are not dependent on animal or fixation method for this study (see Appendix B). Furthermore, the pericellular gap size is found to be proportional to the cell process diameter, where regression analysis yields R^2 = 59% (Fig. 4.13a). As well, both the gap size and process diameter are found to decrease as a function of distance from the cell body, where a high correlation is found for the cell process diameter (R^2 = 78%). However, the high variability of the pericellular gap size yields a significantly lower correlation, where regression analysis gives R^2 = 55% (Fig. 4.13b, c).

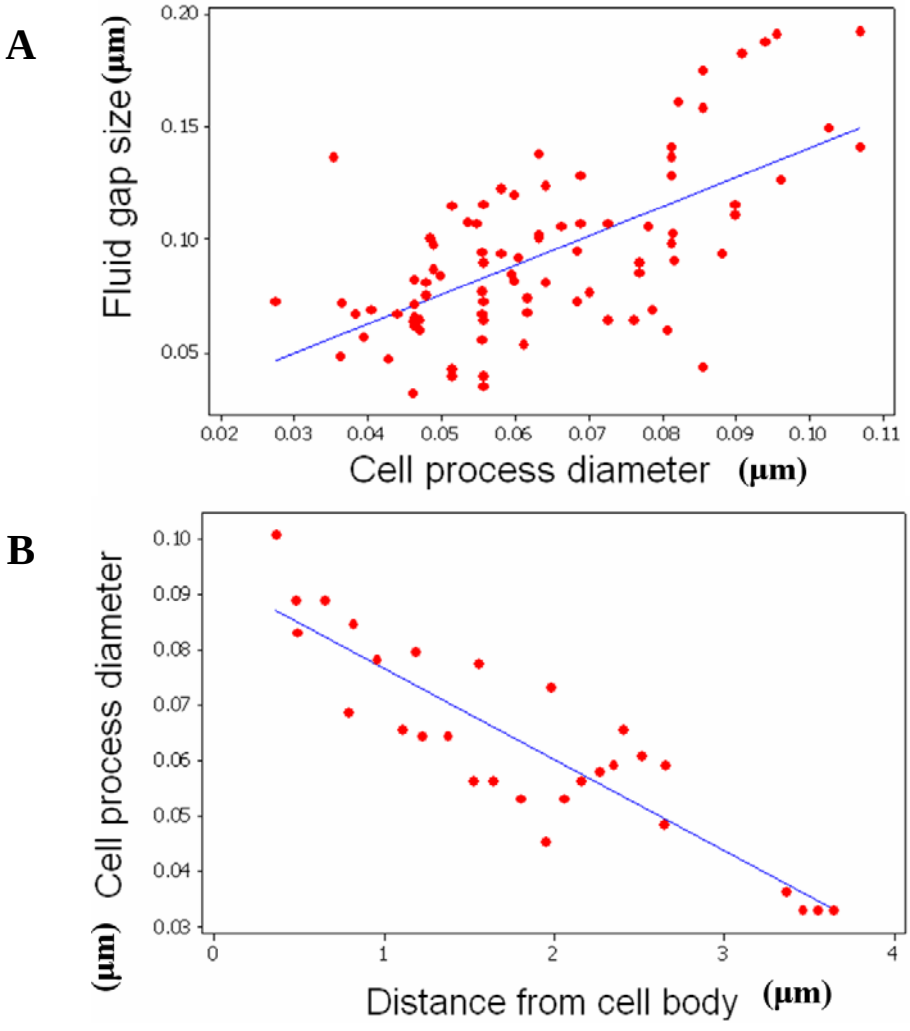

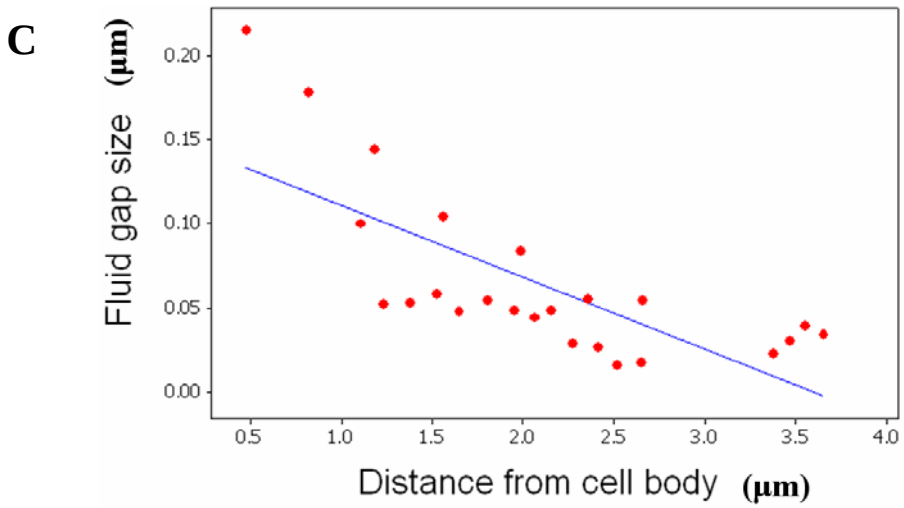

Figure 4.13: Statistical calculations from image analysis: (a) fluid gap size as a function of cell process diameter ($R^2 = 59\%$), (b) cell process diameter as a function of distance from the cell body ($R^2 = 78\%$), and (c) fluid gap size as a function of distance from the cell body ($R^2 = 55\%$).

DISCUSSION

In an effort to understand the mechanical environment of the osteocyte computational models have been used to predict periosteocytic flow *in vivo*[8]. However, due to the geometrical complexity of the lacunocanalicular network in bone, highly idealized models have been created to minimize both temporal and computational expense. Yet, these idealizations may have an effect on the predictions of the osteocyte's mechanical environment, especially if one considers the paradox that exists between *in vitro* observations of the mechanical stimulation necessary to exhibit a cellular response and the *in vivo* magnitudes of mechanical stimulation that are predicted to be present. Thus, the purpose of this study is to investigate the effects of geometric idealizations in computational modeling of pericellular flow using physiologic geometries acquired from high-resolution micrographs of the lacunocanalicular network, and determine whether or not it is necessary to incorporate anatomically correct geometries into computational models.

Overall, idealization of pericellular geometry is shown to reduce both the magnitude and variance of the predicted shear stress on a cell process. In the two-dimensional models, each level of idealization decreases the size and number of protrusions from the mineralized matrix. Consequently, smoothing of the canalicular wall opens the channel spacing between the process surface and the mineralized matrix which causes a decrease in the magnitude of stress below protrusion points, as well as a decrease in the overall change in shear stress along the process wall.

The inclusion of physiologic geometry, or specifically the protrusions of the mineralized matrix from the canalicular wall, causes large variations in flow and shear stress, where stress spikes are found to be up to 5× the most idealized case. In the two-dimensional and axisymmetric models, both velocity and stress on the process wall increases dramatically below each protrusion point. The axisymmetric third-dimension further amplifies the shear stress imparted at the cell surface. Thus, any results acquired in the two-dimensional models are assumed to be representative of the influence of matrix geometry on flow, where reported magnitudes likely increase for three-dimensional flow. However, in the non-axisymmetric 3D model, fluid is expectedly allowed to flow around the protrusion point, decreasing velocity magnitude, but increasing the derivative. Even though the velocity differs from between the two- and three-dimensional cases due to continuity, the shear stress still increases at the protrusions. Thus, analyzing geometry idealization using two-dimensional models is validated for shear stress predictions, and suffices to yield an understanding of the influence of anatomically-correct geometry on flow. In addition, it is interesting to note that the shear stress before and after the protrusion is actually lower than the “baseline”

stress found on the process wall in areas devoid of matrix protrusions. Thus, the amplification or increase in shear stress is even more dramatic when compared to the immediate-surrounding process geometry, suggesting possible implications in cell-process physiology.

In models with idealized geometries, the range of predicted shear stress may encompass the average values from the physiologic cases, but they consequently yield lower maximum values and a decreased variance along the cell surface. This reduction in predicted mechanical force on the cell process is a direct result of the elimination of matrix protrusions from the canalicular wall. It is shown using statistical analysis of the micrograph geometries that these protrusions are present within the canalicular geometry, where pericellular space between the process wall and mineralized matrix (canalicular wall) has a mean value similar to that reported in the literature (0.131 μm), but is highly variable (sd = 0.056 μm). This high variability in the pericellular spacing is representative of the rough, complex canalicular wall, as well as the inherent protrusions or encroachments of the mineralized matrix. In addition, the pericellular gap size, as well as the cell process diameter, is found to decrease with distance from the cell body, tapering off as they approach the gap junction; this validates previous models of periosteocytic flow from the literature[8].

For damaged bone tissue, or that with included microcrack geometry, shifts in canalicular geometry cause both increases and decreases in peak stresses on the cell process. Depending on orientation and final location of the protrusions (due to crack formation), the imparted stress to the cell surface varies relative to the normal physiologic case. In the model presented, decreases in stress are still above baseline; however

increases in stress are significantly higher than in the healthy geometry. If it is proposed that peak stresses on the cell process trigger the mechanosensors of the cell, it is reasonable to assume that large peaks such as those found in microcrack geometry could trigger bone remodeling in damaged areas of bone. The behavior of bone remodeling due to microcrack induction and its effects have been hypothesized and tested in previous studies[25], and are in agreement with the results presented here.

Limitations in this study arise from the difficulty in acquiring high-resolution images of subcellular canalicular geometry in which all of the desired structures are visible. Currently, it is not possible to obtain a three-dimensional image of both cellular and matrix geometry at this resolution without the introduction of artifacts. However, using a combination of two-dimensional models from micrograph geometries in conjunction with three-dimensional factors, the imparted forces to the cell are assessed, at least as a first approximation. Also, microcrack models are created for a specific geometry, where variance in geometry shifting could affect the resultant changes in wall shear stress. However, its is assumed that regardless of the shift in geometry, both potential increases and decreases in stress would occur as a result, where any increases would provide a stronger signal for bone remodeling. In addition, although care is taken to reduce artifacts and maintain the cell process and *lamina limitans*, certain structural components such as the pericellular matrix (PCM) are lost. Thus, pericellular models do not include these structures definitively, but instead the pericellular space is given values for parameters such as porosity and permeability of the PCM based on data from the literature[26,27,10], where the results are unaffected by the inclusion of the PCM. Furthermore, this study purely deals with the imparted fluid forces due to the mineralized

canalicular wall and not the solid dynamics associated with cellular structures, as many studies can be found in the literature. However, this study shows how the imparted forces to the cell can be amplified dramatically using only the canalicular geometry, where it can be used in parallel with solid mechanics models to obtain a complete picture of periosteocytic flow.

Overall, in understanding how protrusions from the mineralized matrix affect process-wall shear stress along with the knowledge of variability of the pericellular space, not only are predictions of the mechanical environment of the osteocyte altered, but local shear stresses on the cell process *in vivo* are likely to be higher and more variable than previously predicted. Inclusions of anatomically-correct subcellular geometries are found to influence the nano-scale flow regimes predicted in bone and around the osteocyte beyond what is predicted using simplified or idealized models, which only give a description of the kinds of imparted forces as well as their location on the cell (ie. processes, body). Inclusion of more physiologic geometries in computational models results in predictions of peak shear stresses on the cell process that approach magnitudes shown to trigger cell activity in *in vitro* models[15-21]. Thus, a major implication of this study is that physiologic subcellular geometries can possibly bridge the gap between *in vitro* and *in vivo* models, where up to an order of magnitude difference has been predicted in the past, and lead to the elucidation of the cellular mechanisms of bone adaptation.

ACKNOWLEDGEMENTS

The authors would like to thank Dr. Gautschi of University of Zurich for his contribution. This study was supported by The Whitaker Foundation. This investigation was conducted in a facility constructed with support from Research Facilities Improvement Program Grant Number C06 RR12463-01 from the National Center for Research Resources, National Institutes of Health.

REFERENCES

1. Peinkowski D, Pollack SR, 1983. The origin of stress-generated potentials in fluid-saturated bone. J Orthop Res 1:30-41.

2. Knothe Tate ML, 2001. Interstitial fluid flow. In: Cowin SC (ed.) Bone Biomechanics Handbook, 2nd ed. CRC Press, New York, NY, USA, pp. 1-29.

3. Knothe Tate ML, 2003. "Whither flows the fluid in bone?" An osteocyte's perspective. J Biomech 36:1409-24.

4. Reich KM, Frangos JA, 1991. Effect of flow on prostaglandin E2 and inositol trisphosphate levels in osteoblasts. Am J Physiol 261:C428-32.

5. You L, Cowin SC, Schaffler MB, Weinbaum S, 2001. A model for strain amplification in the actin cytoskeleton of osteocytes due to fluid drag on pericellular matrix. J Biomech 34:1375-86.

6. Sorkin AM, Dee KC, Knothe Tate ML, 2004. "Culture shock" from the bone cell's perspective: emulating physiological conditions for mechanobiological investigations. Am J Physiol Cell Physiol 287:C1527-C1536.

7. Anderson EJ, Falls TD, Sorkin AM, Knothe Tate ML, 2006. The imperative for controlled mechanical stresses in unraveling cellular mechanisms of mechanotransduction. Biomed Eng Online 5:27.

8. Anderson EJ, Kaliyamoorthy S, Alexander JID, Knothe Tate ML, 2005. Nano-microscale models of periosteocytic flow show differences in stresses imparted to cell body and processes. Ann Biomed Eng 33:52-62.

9. Steck R, Knothe Tate ML, 2005. In silico stochastic network models that emulate the molecular sieving characteristics of bone. Ann Biomed Eng 33:87-94.

10. Han Y, Cowin SC, Schaffler MB, Weinbaum S, 2004. Mechanotransduction and strain amplification in osteocyte cell processes. Proc Natl Acad Sci 101:16689-94.

11. Scherft JP, 1972. The lamina limitans of the organic matrix of calcified cartilage and bone. J Ultrastruct Res 38:318-31.

12. Knothe Tate ML, 2001. Mixing mechanisms and net solute transport in bone. Ann Biomed Eng 29:810-811.

13. Reilly GC, Knapp HF, Stemmer A, Neiderer P, Knothe Tate ML, 2001. Investigation of the morphology of the lacunocanalicular system of cortical bone using atomic force microscopy. Ann Biomed Eng 29:1074-81.

14. Rubin CT, Lanyon LE, 1984. Regulation of bone formation by applied dynamic loads. J Bone Joint Surg Am 66:397-402.

15. Burger EH, Veldhuijzen JP, 1993. Influence of mechanical factors on bone formation, resorption and growth in vitro. In: Hall BK (ed.) Bone, vol. 7. CRC Press, Boca Raton, FL, USA, pp. 37-56.

16. Almekinders LC, Banes AJ, Ballenger CA, 1993. Effects of repetitive motion on human fibroblasts. Med Sci Sports Exerc 25:603-7.

17. Klein-Nulend J, van der Plas A, Semeins CM, Ajubi NE, Frangos JA, Nijweide PJ, Burger EH, 1995. Sensitivity of osteocytes to biomechanical stress in vitro. FASEB J 9:441-5.

18. Guilak F, Ratcliffe A, Mow VC, 1995. Chondrocyte deformation and local tissue strain in articular cartilage: a confocal microscopy study. J Orthop Res 13:410-21.

19. Owan I, Burr DB, Turner CH, Qiu J, Tu Y, Onyia JE, Duncan RL, 1997. Mechanotransduction in bone: osteoblasts are more responsive to fluid forces than mechanical strain. Am J Physiol 273:C810-5.

20. Smalt R, Mitchell FT, Howard RL, Chambers TJ, 1997. Induction of NO and prostaglandin E2 in osteoblasts by wall-shear stress but no mechanical strain. Am J Physiol 273:E751-8.

21. You J, Yellowley CE, Donahue HJ, Zhang Y, Chen Q, Jacobs CR, 2000. Substrate deformation levels associated with routine physical activity are less stimulatory to bone cells relative to loading-induced oscillatory fluid flow. J Biomech Eng 122:387-93.

22. McGarry JG, Klein-Nulend J, Mullender MG, Prendergast PJ, 2005. A comparision of strain and fluid shear stress in stimulating bone cell responses—a computational and experimental study. FASEB J 19:482-4.

23. Nicolella DP, Moravits DE, Gale AM, Bonewald LF, Lankford J, 2006. Osteocyte lacunae tissue strain in cortical bone. J Biomech 39:1735-43.

24. Fritton SP, McLeod KJ, Rubin CT, 2000. Quantifying the strain history of bone: spatial uniformity and self-similarity of low-magnitude strains. J Biomech 33:317-25.

25. Tami AE, Nasser P, Verborgt, O, Schaffler MB, Knothe Tate ML, 2002. The role of interstitial fluid flow in the remodeling response to fatigue loading. J Bone Miner Res 7:2030-7.

26. Weinbaum S, Cowin SC, Zeng Y, 1994. A model for the excitation of osteocytes by mechanical loading-induced bone fluid shear stresses. J Biomech 27:339-60.

27. You LD, Weinbaum S, Cowin SC, Schaffler MB, 2004. Ultrastructure of the osteocyte process and its pericellular matrix. Anat Rec A Discov Mol Cell Evol Biol 278:505-13.

CHAPTER 5

The imperative for controlled mechanical stresses in unraveling cellular mechanisms of mechanotransduction

Eric J. Anderson[1], Thomas D. Falls[2], Adam M. Sorkin[2], Melissa L. Knothe Tate[1,2]

[1]Dept. of Mechanical & Aerospace Engineering, Case Western Reserve University, Cleveland, OH
[2]Dept. of Biomedical Engineering, Case Western Reserve University, Cleveland, OH

Published in *Biomedical Engineering Online* 2006, 5:27

ABSTRACT

In vitro mechanotransduction studies are designed to elucidate cell behavior in response to a well-defined mechanical signal that is imparted to cultured cells, *e.g.* through fluid flow. Typically, flow rates are calculated based on a parallel plate flow assumption, to achieve a targeted cellular shear stress. This study evaluates the performance of specific flow/perfusion chambers in imparting the targeted stress at the cellular level. To evaluate how well actual flow chambers meet their target stresses (set for 1 and 10 dyn/cm^2 for this study) at a cellular level, computational models were developed to calculate flow velocity components and imparted shear stresses for a given pressure gradient. Computational predictions were validated with micro-particle image velocimetry (μPIV) experiments. Based on these computational and experimental studies, as few as 66% of cells seeded along the midplane of commonly implemented flow/perfusion chambers are subjected to stresses within $\pm$10% of the target stress. In addition, flow velocities and

shear stresses imparted through fluid drag vary as a function of location within each chamber. Hence, not only a limited number of cells are exposed to target stress levels within each chamber, but also neighboring cells may experience different flow regimes. Finally, flow regimes are highly dependent on flow chamber geometry, resulting in significant variation in magnitudes and spatial distributions of stress between chambers. The results of this study challenge the basic premise of *in vitro* mechanotransduction studies, *i.e.* that a *controlled* flow regime is applied to impart a *defined* mechanical stimulus to cells. These results also underscore the fact that data from studies in which different chambers are utilized can not be compared, even if the target stress regimes are comparable.

INTRODUCTION

Mammalian cells inhabit a variety of biochemical and biophysical environments within the body, many of which are defined by exposure to distinct and dynamic fluid media. Flow of fluid plays a key role in mechanotransduction via direct transfer of mechanical forces from the fluid to the membranes of cells as varied as those found in the vascular endothelium[1], bone interstitium[2], and renal proximal tubules[3]. Whether induced by contraction of cardiac muscle, mechanical loading, or accumulation of renal filtrate, these flows create shear stresses at the fluid/cell interface that have been hypothesized to strain the cytoskeleton, trigger cellular force receptors and/or affect the conformation of membrane bound proteins implicated in numerous healthy, inflammatory, or disease state signaling pathways[4-6]. Indirectly, local flows influence mechanochemical transduction by

regulating the chemical environment that governs cell activity through both the early development of and subsequent remodeling of tissues[7-11]. By modulating chemokinetic gradients and osmotic pressure, fluid flow may affect receptor binding kinetics[12], membrane porosity[13] as well as chemotaxis[14, 15]. The fluid-structure interactions at the cellular level of many tissues are poorly understood yet they appear to be universal across tissue types and may hold the key to unraveling mechanisms of mechanotransduction at a cellular and subcellular level. Knowledge of such mechanisms could be applied not only to understand etiology of different diseases but also to develop prophylactic measures to prevent such diseases[16-18].

Due to practical difficulties in studying fluid flow *in situ* during normal physiologic activity, cell perfusion chambers have been developed to simulate such physiologic fluid flow and to observe cellular responses *in vitro*. In particular, the pressure driven parallel-plate perfusion chamber design has been implemented[19-23] and optimized[24-27] for application of known fluid shear stresses and correlation to cell activity and adaptation[28]. Variations of the parallel-plate chamber design have become commonplace in cell biological research and provide a basis for current *in vitro* modeling of physiologic flow regimes including those relevant to bone[20,21,28-31], articular cartilage[32], connective tissue[33], vascular endothelium[34], leukocyte recruitment[14,35], as well as pathologies specific to renal dysfunction[36], and respiratory distress[37]. In addition, flow perfusion chambers have been implemented to characterize cell-biomaterial interactions[27,38,39], improve tissue engineered implant [40], and develop novel biomedical applications[41]. While this approach has obvious advantages for investigating effects of fluid shear in diverse biomedical arenas, it is not known how well these *in vitro* flow

chambers perform, *e.g.* in achieving a desired stress at the cell level or in emulating physiologic flow regimes[42].

The ability to study cells in a controlled environment which mimics the conditions found *in vivo* is essential to understanding many basic cellular mechanisms, such as the cellular response to applied shear stress. As computational models have been developed to predict flow within the examined chambers, it is also necessary to examine the flow experimentally. In order to use a parallel plate flow chamber as a test bed for further studies, it is essential to know how close the stresses actually imparted at the cellular level match the target stresses.

Hence, the purpose of this study was to compare flow regimes in three commercially available cell flow/perfusion chambers to evaluate their efficacy in providing a defined flow regime and shear stress to cultured cells. For each chamber, the principal velocity component and local shear stress imparted through fluid flow were calculated for a target shear stress of 1 and 10 dyn/cm^2 used typically for osteoblast stimulation[31]. Special attention was paid to local flow regimes in the vicinity of cells within the chambers. Computational results for velocity were validated using microparticle image velocimetry (μPIV) for cases with and without cells seeded in the chambers.

METHODS

3-D modeling

Computational fluid models were created for three commercial cell flow/perfusion chambers (FCS, Oligene GmbH; FCS2, Bioptechs; RC-30HV, Warner

Instruments) to elucidate the effect of their specific design parameters on flow fields and resulting stress regimes that are imparted to cells seeded within the chambers (Figure 5.1). First, dimensions of all surfaces that define the fluid geometry (inlets, outlets, and chamber walls) were measured using a precision caliper and micrometer. Then the fluid was mapped to track the flow from inlet to outlet. Thereafter, for each commercial chamber, flow regimes were analyzed and compared for two target fluid shear stress magnitudes representative of those typically imparted to an osteoblastic monolayer (1, 10 dyn/cm^2).

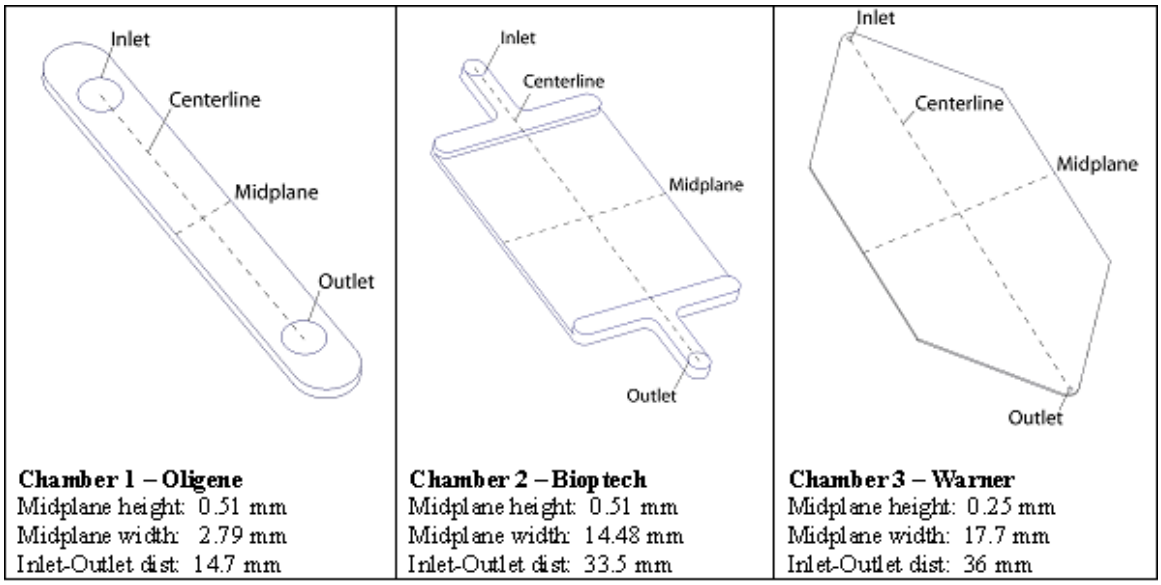

Chamber 1 – Oligene
Midplane height: 0.51 mm
Midplane width: 2.79 mm
Inlet-Outlet dist: 14.7 mm

Chamber 2 – Bioptech
Midplane height: 0.51 mm
Midplane width: 14.48 mm
Inlet-Outlet dist: 33.5 mm

Chamber 3 – Warner
Midplane height: 0.25 mm
Midplane width: 17.7 mm
Inlet-Outlet dist: 36 mm

Figure 5.1: Schematic diagrams demonstrating characteristic dimensions of the flow chambers studied (not to scale).

Fluid meshing

The creation of the fluid mesh is critical to the computational analysis, as it delineates interfaces between fluid cavities as well as node locations where each calculation is made by the solver. Care was taken to place node locations in the critical areas throughout the model, in particular at flow transition areas such as at inlets, outlets, and points of flow expansion or contraction. This procedure not only ensures the

accurate description of flow through the channels, but it also reduces the computational requirements of the simulation. Hence, the mesh includes only fluid volumes within the chamber itself and not flow volumes within inlet/outlet tubing or volumes outside of the device. Two sets of models were created, accounting for (*i*) the chamber geometries without cells seeded on the bottom surface (for all chambers), and (*ii*) the chamber geometries with an array of cells modeled on the lower surface of the flow chamber. Similar to previous studies on flow over cell-shaped protrusions, the cells were modeled as rigid spheroid protrusions on the chamber surface, with dimensions typical of osteocytes (height = 10 μm, radius= 15 μm)[43,45,50]. The number of nodes used in each chamber was 64000, 480000, and 89000 for chambers 1, 2, 3 respectively, where the average finite volume modeled was on the order of 10^{-13} m^3. Finally, the mesh, which provides a visual map of the flow geometry, was imported into a computational fluid dynamics (CFD) package (CFD-ACE, CFDRC), to allow for the definition of boundary conditions and simulation of flow regimes for targeted stress magnitudes.

Computational fluid dynamics

For each chamber, the velocity profile and pressure variation were determined at the inlet and outlet, for a corresponding maximum target shear stress 1 and 10 dyn/cm^2, at the location where cells are placed within the chamber (*i.e.* bottom surface of chamber). These were then applied as boundary conditions, to focus simulations on the interior of the chamber cavity where the cells are cultured. Using a discretization convective-upwind scheme, velocity profiles were calculated from the continuity equation and Navier-Stokes equations in three dimensions (3D),

$$\nabla \cdot V = 0 \tag{1}$$

$$\rho\left(V \cdot \nabla V\right) = -\nabla P + \mu \nabla^2 V \tag{2}$$

where V is velocity vector, μ is the fluid viscosity, p is pressure, and ρ is density. Pressure and velocity at the center of each finite volume are decoupled by linear interpolation, where instabilities are avoided by averaging the Navier-Stokes equations for each volume face and relating the face velocity to the pressure gradient. Reynolds number, Re,

$$\mathrm{Re} = \frac{\rho u_m D_h}{\mu} \tag{3}$$

was also calculated for each case to further characterize the flow. Values calculated based on the mean velocity, u_m, and hydraulic diameter, D_h, at the midplane of the chambers are estimated to be on the order of 1 - 4. As this Re number falls well within the laminar region (laminar flow, Re<1400), viscous-dominated flows are anticipated. Using velocity components and pressure from above, the fluid shear stress, τ, at the surface of the chamber was calculated from the viscosity and rate of strain, $\dot{\gamma}$,

$$\tau_{wall} = \mu\dot{\gamma} \tag{4}$$

The perfusion medium was idealized as water with appropriate constant fluid properties: μ = 0.001 kg/m-s and ρ = 1000 kg/m^3. A no-slip boundary condition was used for all chamber walls, and the inlet/outlet conditions were determined for standard pipe (tubing) flow with a laminar parabolic velocity profile and corresponding pressure gradient. Simulations were carried out using a finite-volume numerical method under steady flow conditions, with a convergence criterion of 0.0001, for the solution of each velocity component and pressure gradient per finite volume. The resulting calculations included

3D spatial resolution of the velocity profiles, pressure gradients along the flow direction (axial), and the shear stress at the bottom surface. These data were recorded for each chamber.

Node densities were increased at the center of the chamber in order to track flow and stress fields at higher resolution in the area where cells are seeded in mechanotransduction studies. The volume of fluid directly above this center section was isolated for each case and the velocity profile and pressure gradient were magnified in this section to increase resolution and to extract maximum and minimum values. Shear stresses experienced at the surface were then determined for each flow chamber. Thus, accurate comparisons could be made between global flow regimes in the commercial perfusion chambers as well as local flow regimes that impart stresses to cells within the chamber.

μ-PIV validation

In order to validate the velocity and shear stress components found in the computational models, microparticle image velocimetry (μPIV) techniques were performed to measure the rate of flow found within each chamber design. A Leica DMIRE-2 (Leica Microsystems, Inc, Bannockburn, IL) inverted epifluorescent microscope with integrated (hardware and software) Scan IM 100 x 120 automated stage (Marzhauser GmbH & CO, Wetzlar-Steindorf, Germany) and Retiga EXi camera (Q-Imaging, Burnaby, BC, Canada) were used to image TetraSpeck fluorescent microparticles (4 μm diameter; excitation wavelengths 365/505/560/660 nm; emission wavelengths 430/515/580/680 nm; T-7283, Molecular Probes, Eugene, OR) as they

traveled through the chamber in a 2.8 x 10^4 microspheres per ml DH_2O suspension. As the suspension moved through the flow channel, an automated imaging routine (implemented in OpenLab 4.0.3, Improvision Inc, Lexington, MA) captured images of a grid containing the entire flow field. This procedure was then repeated 5 times consecutively to capture the maximum number of particles, and to minimize sampling error. This process was then repeated at several planes spaced 50-100 μm apart through the depth the flow channel. The microspheres appeared in the images as streaked lines of varying length, where the length of the streak was equal to the distance traveled during the exposure time interval.

The same set of procedures was also used to perform another μPIV study to determine any effects that seeded cells might have on flow fields within the chamber. The Oligene chamber (chamber 1) was implemented for this set of experiments. Degreased silica glass coverslips were etched with sodium hydroxide for 1 hour, and then covered with a 0.15 mg/mL solution of a collagen/acetic acid solution for 1 hour. After rinsing, MLO-Y4 osteocyte-like cells (a generous gift from Lynda Bonewald, University of Missouri-Kansas City) were seeded onto the coverslips at a density of approximately 5500 cells/cm^2. The cells were then incubated for 48 hours before being fixed in a 3.7% solution of formaldehyde for 10 minutes.

The particle velocities within each chamber were calculated using a combination of image processing and symbolic mathematical manipulation software. After conversion to gray-scale, the images were auto-leveled in Adobe Photoshop CS (Adobe Systems, Inc.) to enhance contrast between the particle streaks and background noise. Image thresholding and particle analysis was completed using ImageJ 1.34 (NIH, Bethesda,

MD). After exclusion parameters were applied to remove any artifacts (too large or small to be particles), the output data file for each image was processed using a Mathematica (Wolfram Research, Inc.) notebook file. Velocity was calculated as the distance traveled per duration of imaging (i.e. shutter speed). The sequential data at each point was combined to create an array of sample-averaged velocities, and used to generate a vector field depicting particle velocity through the entire flow field. The measured profiles were then compared to the calculated velocity components obtained from the CFD models for flow rates equivalent to the target shear stresses in order to validate the computational results.

Particular care was taken to ensure repeatability of trials as well as to minimize random error. Using the automated stage and OpenLab, the exact position of the flow channel (with respect to the stage adapter) was recorded in the software for each chamber. This allowed for the automations to be repeated using the same image coordinates each time. Any random errors that were introduced when capturing the particle streaks were minimized by running the automation five times consecutively for each focal depth, in order to capture the maximum number of particle streaks possible. Two-times binning, which acquires 2 × 2 adjacent pixels as one large pixel, was used to increase the speed of image (and particle streak) capture. Pixel size is 0.5 × 0.5 μm for the 20× objective and 1.0 × 1.0 μm for the 10× objective. Hence, binning, which is implemented to minimize any lag time in real-time imaging, could potentially introduce an error of 1-2% in measurement of microsphere displacement, *e.g.* considering a 100 μm total displacement. During image processing, particle streaks attributable to background

noise or particles not moving with the rest of the fluid flow were identified as being outside of the range of lengths possible for the given flow regime and were removed.

RESULTS

In each chamber, the *velocity component* of the flow field varies as a function of location within the area of cell seeding. As a result, the local shear stress imparted to the cells varies as a function of location as well. Only a limited area is exposed to the target stress level (Table 5.2). Furthermore, the *range* of imparted wall shear stresses vary from chamber to chamber by up to 2-fold along the midplane without cells (Figures 5.2-7). When cells are included within a specific chamber, the imparted stress at the wall (on cell body) increases by 3-fold (Figures 5.8, 5.9). Finally, the *location* of the area where the targeted shear stress (1 and 10 dyn/cm^2) is achieved varies from chamber to chamber. Details for each chamber with a target stress of 1 dyn/cm^2 are described below; results with a greater target stress (10 dyn/cm^2) yielded similar profiles, with increased magnitude, and are summarized at the end of this section.

Chamber	Flow rate (ml/min) 1 dyn/cm^2	Magnification	Camera Shutter Speed (ms)
Oligene FCS	0.774	20×	20
Oligene FCS (with cells)	0.774	20×	20
Bioptechs FCS2	3.624	10×	20
Warner RC-30	1.278	10×	10

Table 5.1: Flow rates needed for 1 dyn/cm^2 shear stress, magnification used and camera shutter speed used for each of the three chambers tested (including the Oligene chamber with the cells seeded on the coverslip). Note: The eyepiece objective of the microscope used was 1x.

Table 5.2: Computational results: percentage of the region of interest for each chamber that is within the specified ranges of the target wall shear stress; definitions of midplane and centerline for each chamber are shown in Figure 1.

Chamber	Region of interest	Within 5% of target stress	Within 10% of target stress	Within 50% of target stress
Oligene FCS	Midplane	49%	72%	96%
	Centerline	75%	81%	92%
Bioptechs FCS2	Midplane	92%	94%	98%
	Centerline	35%	42%	67%
Warner RC-30HVS	Midplane	96%	97%	100%
	Centerline	10%	28%	58%

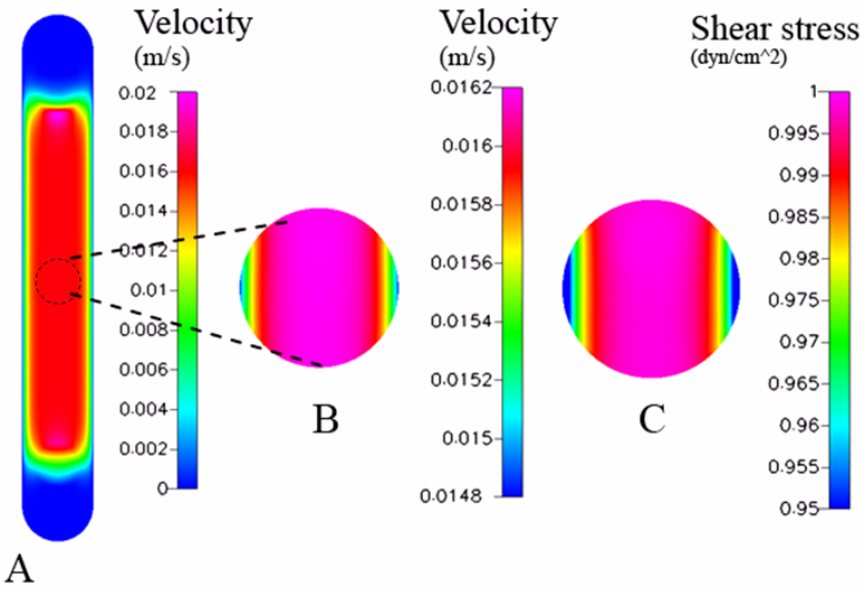

Figure 5.2: Chamber 1 (Oligene) – computational model predictions showing velocity profiles at midplane and wall shear stress profiles at the midplane and centerline of the chamber.

Chamber 1(Oligene) – 1 dyn/cm^2

In the first chamber studied, the calculated velocity magnitudes remain constant along the centerline, with a maximum velocity of 0.0152 m/s for a Reynolds number of 4 (Figure 5.2). The corresponding wall shear stress magnitudes vary midplane, along the width of the chamber floor (which is narrower than the others studied, *i.e.* 2.8 mm as compared to ~14.5 and ~17.7 mm, for chambers 2 and 3 respectively). Looking into the depth of the chamber (Figure 5.3), wall shear stress magnitudes along the lower surface range from 0.2 - 1.05 dyn/cm^2 with a mean stress of 0.89 dyn/cm^2 (measured midplane between the inlet and outlet). Only 49% of midplane data points (evenly spaced) were

within ±5% of the target shear stress; however 72% of the midplane data points fell within 10% of the target stress (Table 5.2). Shear stress peaks near the inlet/outlet of the chamber but remains nearly constant (1.02 dyn/cm^2) along the centerline of the chamber. The resultant stress deviates increasingly from the target shear stress, with increasing distance from the centerline of the chamber.

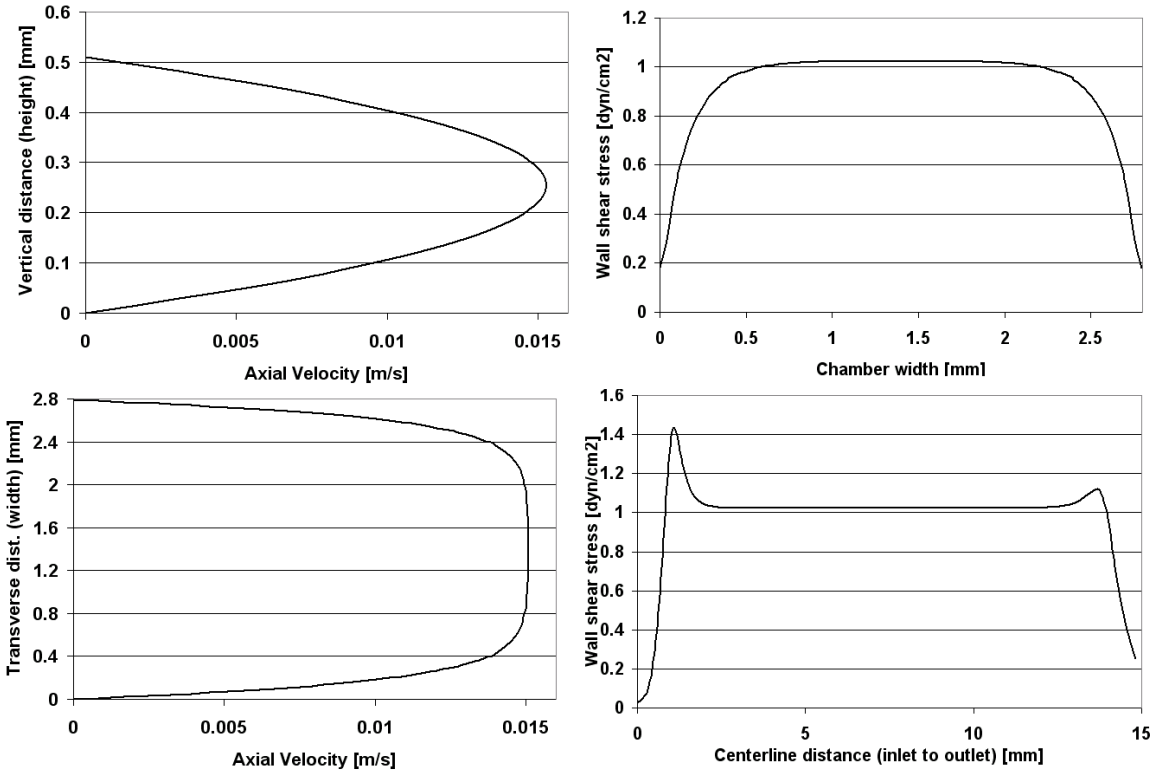

Figure 5.3: Chamber 1 (Oligene) – computational model predictions are shown for the velocity profile [m/s] at the center of the chamber (maximum velocity) and wall shear stress [dyn/cm^2] along chamber surface, within the region of interest for cell mechanotransduction studies.

The experimentally measured flow profile shows a peak in fluid velocity at the center of the channel, which increases with proximity to the side walls (Figure 5.10). Furthermore, actual fluid velocities measured with PIV rarely reached target velocities (calculated as 0.0151 m/s and predicted to produce the 1 dyn/cm^2 target shear stress) in the area where cells are seeded (Table 5.3). None of the 26 data points examined was within ±10% or ±25% of the target velocity, and only 7 out of 26 (26.92%) data points

were within ±50% of the target velocity (Table 5.3). It should be noted that the region of interest in this chamber is approximately one fourth of the size of the other two chambers (Oligene: 2mm, Bioptechs and Warner: 8mm). A similar number of data points were obtained by imaging the PIV experiments at a magnification of 20×.

Chamber	Within ±10%	Within ±25%	Within ±50%
Oligene FCS	0%	0%	26.92%
# data points/total	(0/26)	(0/26)	(7/26)
Bioptechs FCS2	20.00%	73.33%	96.67%
# data points/total	(6/30)	(22/30)	(29/30)
Warner RC-30HVS	21.43%	39.29%	85.71%
# data points/total	(6/28)	(11/28)	(24/28)

Table 5.3: Experimental: number of data points within ± 10, 50 and 100 % of the target value for each of the three chambers tested. The regions of interest used are depicted in Figures 10-12.

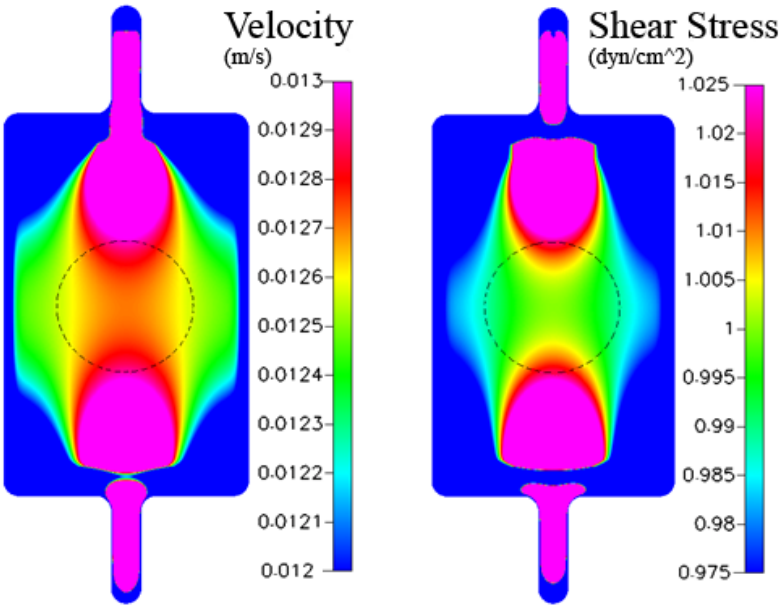

Figure 5.4: Chamber 2 (Bioptechs) – computational model predictions are shown for the velocity profile [m/s] at the center of the chamber (maximum velocity) and wall shear stress [dyn/cm^2] along chamber surface, within the region of interest for cell mechanotransduction studies.

Chamber 2 (Bioptechs) – 1 dyn/cm^2

In the second chamber studied flow profiles are dominated by the inlet and outlet expansion and nozzle zones, respectively (Figure 5.4). Here, the midplane velocity varies

only slightly across the width of the chamber (14.4 mm), where the maximum velocity is 0.0127 m/s; however greater variations in velocity are found between the inlet and outlet (along centerline), corresponding to Reynolds number of 4 (Figure 5.5). The range in wall shear stress that would be experienced by the cells at the surface, along the midplane (0.15 – 1 dyn/cm^2), is lower than that of the previous chamber at comparable locations. Ninety-four percent of the midplane region experiences stresses within $\pm$10% of the target stress (Table 5.2); the mean stress comprises 0.91 dyn/cm^2. However, along the centerline, only 35% of the region is within $\pm$10% of the target, and only 67% within $\pm$50% of the target, respectively.

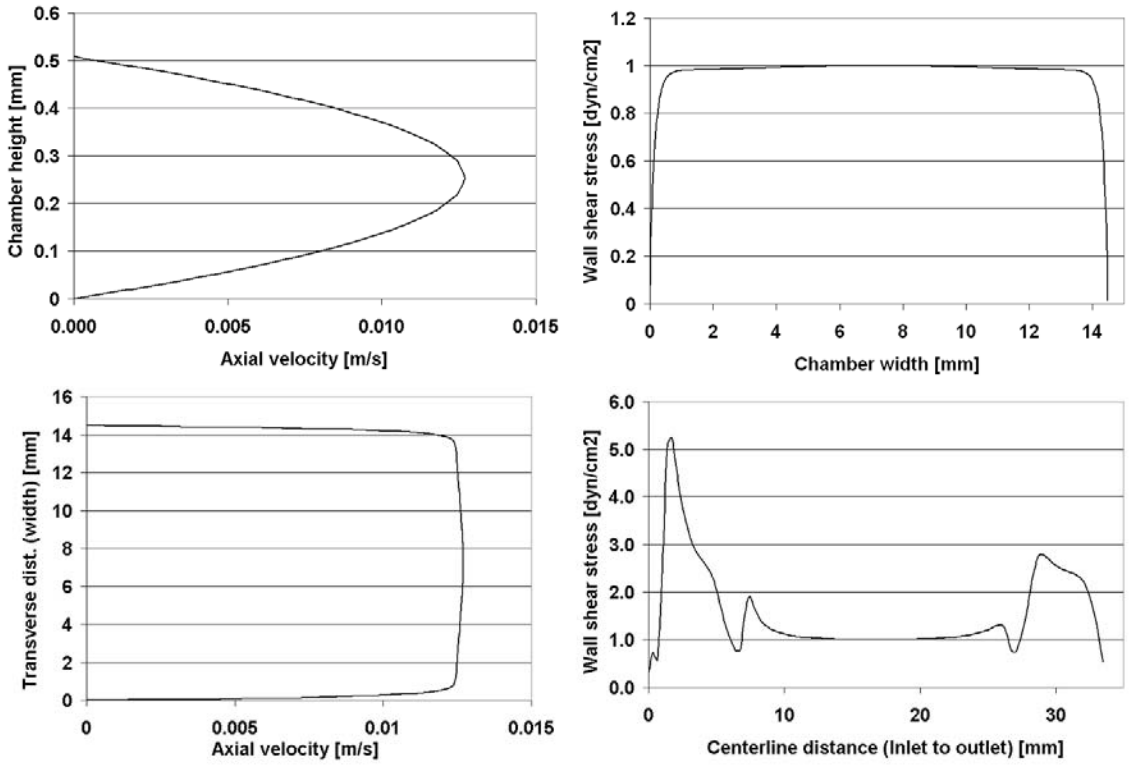

Figure 5.5: Chamber 2 (Bioptechs) - computational model predictions showing velocity profiles at midplane and wall shear stress profiles at the centerline of the chamber.

Experimentally measured flow velocities are relatively uniform in this chamber (Figure 5.11); this is due in part to the fact that the region of interest is small in

comparison to the length of the entire channel (only 30 out of 183 data points), which aids in maintaining uniform flow velocity magnitudes. For this chamber, a 0.0118 m/s target velocity is necessary to achieve 1 dyn/cm^2 of shear stress. While only 6 out of 30 (20%) examined data points were within ± 10% of the target velocity, 22 out of 24 (73.33%) were within ± 25% of the target velocity. Nearly all of the data points, 29 out of 30 (96.67%) were within ± 50% of the target velocity (see Table 5.3).

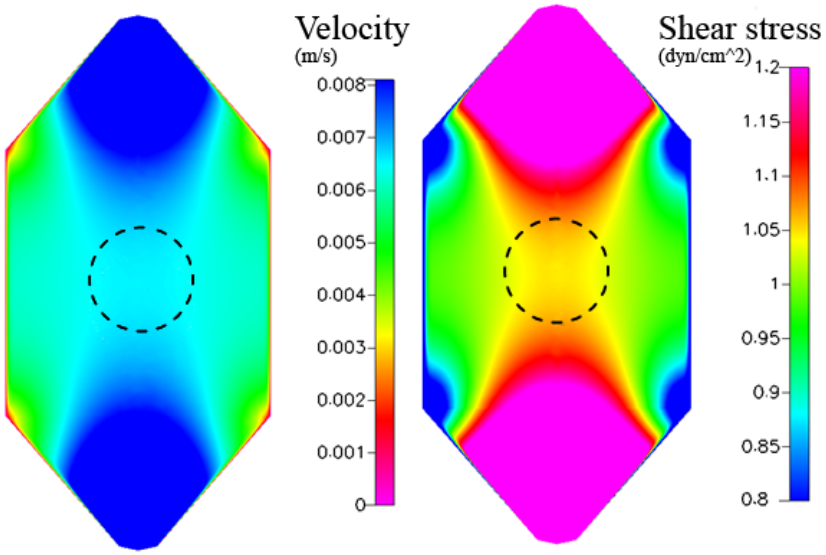

Figure 5.6: Chamber 3 (Warner) - computational model predictions are shown for the velocity profile [m/s] at the center of the chamber (maximum velocity) and wall shear stress [dyn/cm^2] along chamber surface, within the region of interest for cell mechanotransduction studies.

Chamber 3 (Warner) – 1 dyn/cm^2

The design of the third chamber represents a geometric compromise between the first two chambers studied. The flow profile across the midplane of this chamber (Figure 5.6) is similar to that of the second chamber; predicted flow velocities are relatively uniform across the width of the chamber, reaching a maximum of 0.00637 m/s (Reynolds number of 1). Similar to the previous chambers, there is little variance in predicted wall shear stress on the midplane. However, strong variation is predicted along the centerline from inlet to outlet. In this case, the shear stress across the bottom surface at the

midplane varies from 0.5 - 1.05 dyn/cm^2, with a mean stress of 1.01 dyn/cm^2 (Figure 5.7). While 97% of the midplane region is within ±10% of the target stress, only 10% of the region along the centerline exhibits a shear stress within ±5% of the target, and only 58% of the latter region shows a shear stress within ±50% of the intended shear stress (Table 5.2).

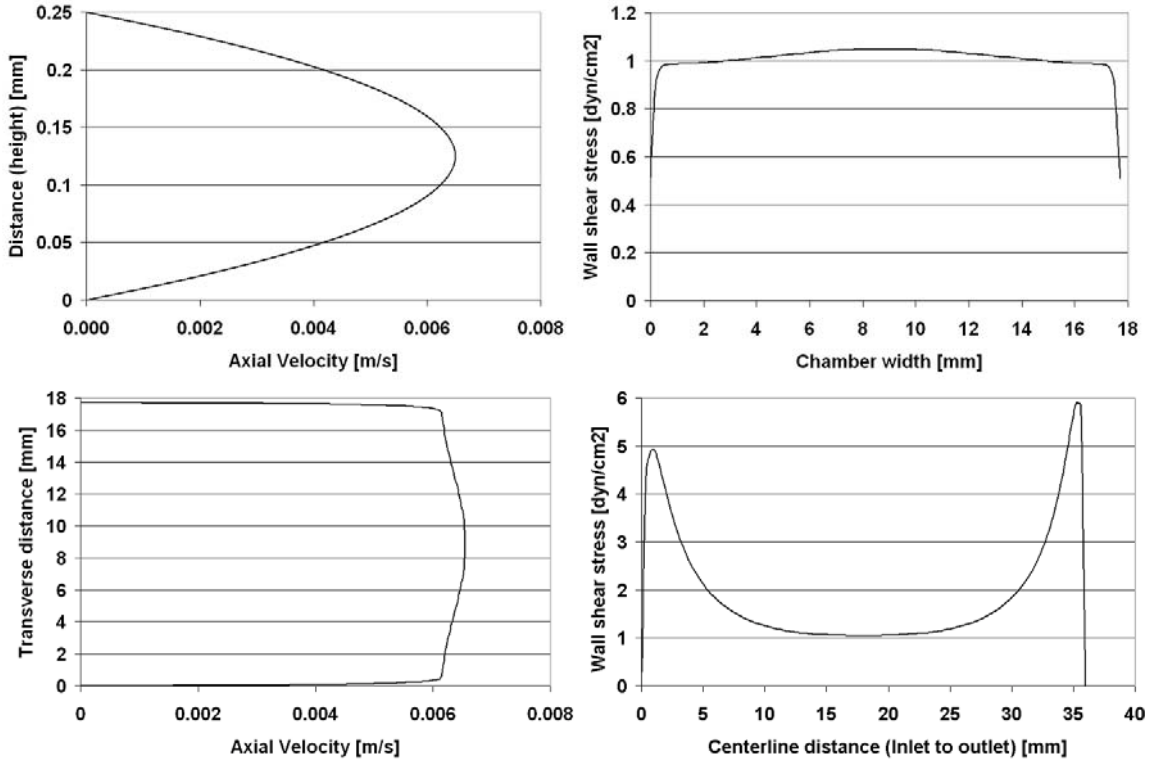

Figure 5.7: Chamber 3 (Warner) - computational model predictions showing velocity profiles at midplane and wall shear stress profiles at the centerline of the chamber.

At a characteristic height, the flow profile in this chamber (Figure 5.12) follows the flow pattern of the idealized parallel plate chamber. The fluid velocity is at its maximum through the central portion of the flow channel and tapers off as it approaches the side walls. In this chamber, the area of interest is approximately the same size as that in the Bioptechs chamber, resulting in a similar number of data points (28) being examined. The target velocity required to achieve 1 dyn/cm^2 shear stress is

approximately 0.0065 m/s. Only 6 out of 28 points (21.43%) were measured within ± 10% of the target velocity, and just 11 out of 28 points (39.29%) were within ± 25% of the target velocity. However, 24 out of 28 points (85.71%) were within ± 50% of the target velocity (Table 5.3).

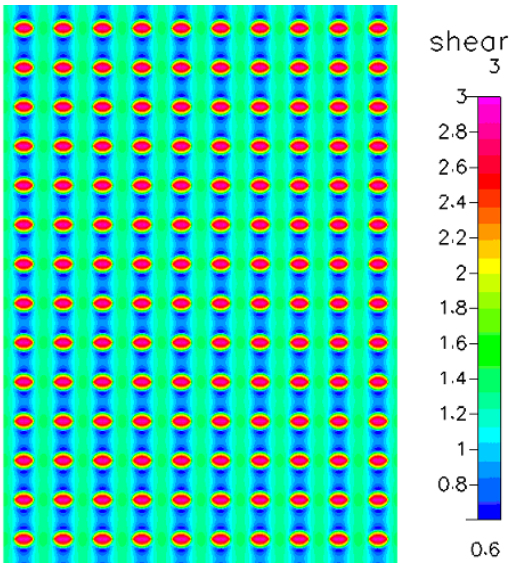

Figure 5.8: Case study based on computation model implementing geometry of Chamber 1 (Oligene) and including the cell monolayer on bottom surface. Looking from above, the shear stress [dyn/cm^2] is mapped in region of interest for cell mechanotransduction studies.

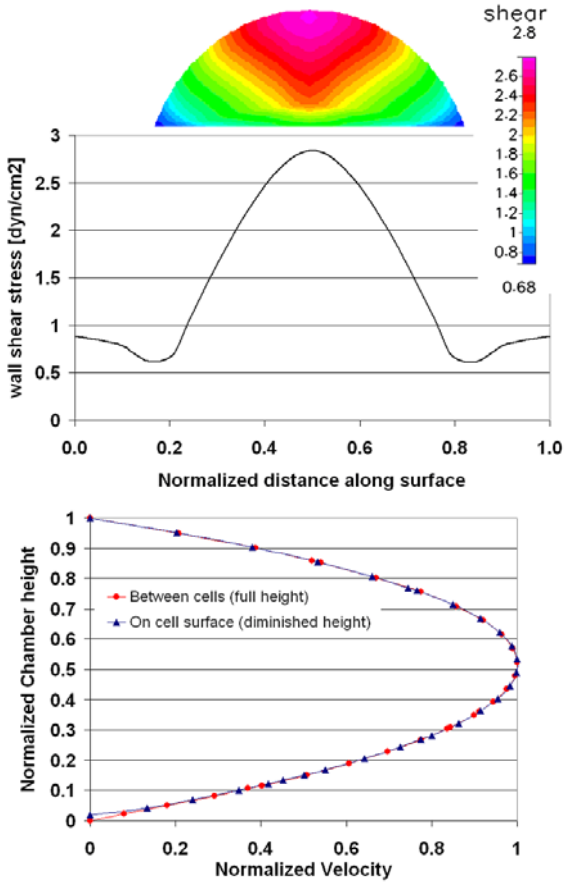

Figure 5.9: Computational measurement of velocity profiles and corresponding shear stresses for the case study implementing the geometry of Chamber 1 (Oligene). Shear stress depicted along the surface of the cells and velocity profiles are shown (a) over a cell surface (shortened chamber height) and (b) between cell array (normalized height), in region of interest where a cell monolayer is cultivated within the chamber.

Results with cell monolayer – 1 dyn/cm^2

To address any potential effects of cells on prevailing flow regimes, computational predictions are also reported for a case study including cells that are

seeded "virtually", on the lower surface of the chamber. Data from case studies using the Oligene chamber geometry is reported and is representative of the results from all three chambers. Inclusion of the cell monolayer in the computational analysis resulted in an almost three-fold increase in applied shear stress on the cell surface (2.8 dyn/cm^2, Figure 5.8); the mean stress was almost twice as high as the target stress. It should be noted that the chamber height decreases due to the presence of the cell layer; this results in an increase in velocity with respect to height of the flow volume and results in an increase in imparted stress (Fig 5.9).

In addition, experimental data was obtained for the Oligene FCS chamber with MLO-Y4 cells seeded on the coverslip. As the particles used for imaging fluid displacements are on the same order of magnitude as cell dimensions, some interactions may have occurred between the beads and cell layer, particularly in the direction perpendicular to flow. The results obtained at a depth of midchannel and upwards correspond well to the computationally predicted cross sectional profile. The velocity is at a maximum close to the center height, decreasing in a near parabolic manner towards the top surface of the channel.

Results with target stress of 10 dyn/cm^2

In a final stage of the analysis, higher target shear stress regimes, *i.e.* 10 dyn/cm^2, were applied to evaluate efficacy of the three chambers in achieving target shear stresses typical for osteoblast and endothelial cell research[31,34,44]. Increasing the target shear stress results in similar flow patterns across the chamber, but the range of observed shear stress magnitudes increases. For all chambers, the velocity profile essentially scales with the

increase in target stress (from 1 to 10 dyn/cm^2). Thus, profiles depicted in the figures are appropriate for understanding chamber performance for various flow rates. In each case, these results show an increase from those calculated for the lower target stress levels in the first stage of the study, and hence, a pattern emerges where the range of shear stress experienced may be proportional to the increase in target stress or flow range.

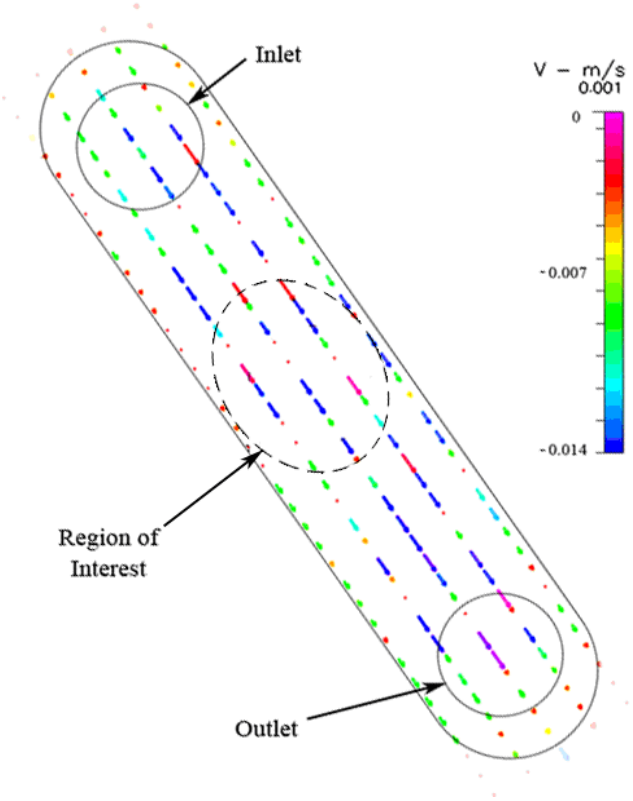

Figure 5.10: Experimental transverse velocity profile, of one focal plane, for the Oligene FCS chamber.

DISCUSSION

Flow/perfusion chambers are designed to impart a constant target shear stress to cells seeded within. In this study, computational fluid dynamics models and experimental fluid dynamics studies were implemented to predict and to measure shear stresses achieved at the cell level when implementing three commercially available cell flow/perfusion

chambers. Both computational predictions, as well as μPIV measurements of actual fluid displacements, showed that the fluid velocity magnitude defining the local mechanical environment of cells is poorly controlled and is location dependent. This results in flow-imparted cellular shear stresses that are highly variable and rarely reach the magnitudes of 1 and 10 dyn/cm^2 set as targets in the context of this study. Furthermore, the mechanical stimulus imparted to cells within a chamber is location dependent, so that two neighboring cells may be exposed to significantly different stresses. In fact along the midplane, between 49% and 96% (depending on the chamber) of imparted stresses are within $\pm$5% of the target magnitude when cells are not included. However, stresses on the cell surface itself can reach as high as 280% of the target value if the cell monolayer is included explicitly in the model. This challenges the basic assumption that all cells in a monolayer experience the desired target stress set using the idealized formula for calculating shear stress at the wall in a parallel plate model, which is the basic paradigm underlying most parallel plate flow chamber designs and their implementation. These trends, *i.e.* the failure to achieve target stresses and the spatial dependence of stress magnitudes across the cell monolayer, were observed in all three flow/perfusion chambers tested. In contrast to these common trends, there was little commonality in flow regimes or shear stresses magnitudes imparted to the cells between the chamber devices studied. Based on these data, not only is calibration of each flow chamber imperative to "tune" or to maximize the possibility of achieving the target stress over the area on which cells are seeded, but also, prior to comparing data between systems, one must take into account intrinsic differences in the flow regimes produced by the different devices.

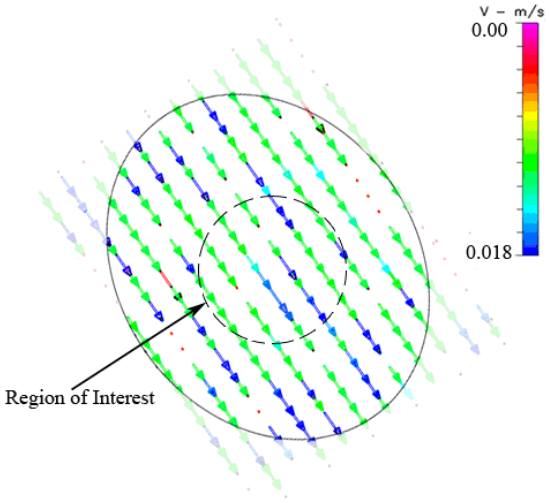

Figure 5.11: Experimental transverse velocity profile, of one focal plane, for the Bioptechs FCS2 chamber. Note: the outer boundary indicates the area that is observable under the microscope.

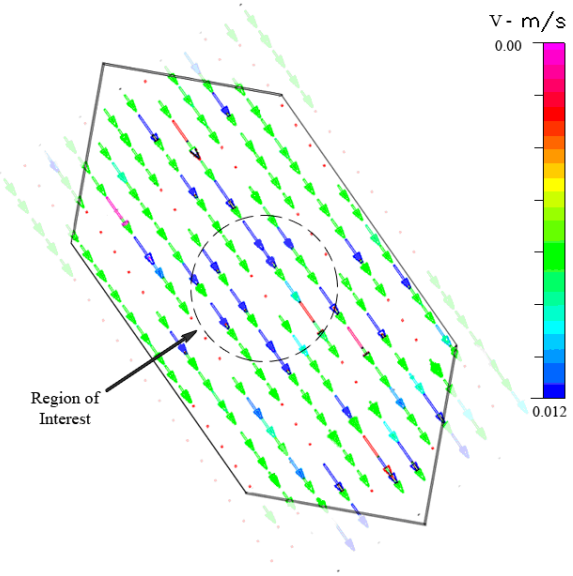

Figure 5.12: Experimental transverse velocity profile, of one focal plane, for the Warner RC-30 HV chamber.

Cell perfusion chambers have been developed to simulate physiologic fluid flow *in vitro* and to study the role of fluid flow in mechanotransduction[19,20,22,23,46]. However, this study evaluates how well these systems perform with respect to achieving the target stress to be imparted to the cell. Among the tested commercial perfusion chambers, all three of the flow regimes showed considerable differences in the flow patterns and shear stresses achieved. The magnitudes of velocity in each chamber varied according to the critical dimensions, as expected, however the shear stresses imparted to the specimen in each chamber fell within dissimilar ranges. The target shear stress was achieved only within a small area of each commercial chamber and the location of this area varied from chamber to chamber. Thus, comparisons of outcome measures for a specific cell response may not be appropriate if different chambers were used to impart stresses to the cell. In addition, the target stress value may not always be located in the same area in different chambers; therefore, the observation of a specific point for comparison would

prove inaccurate since various flow chambers could cause a variety of desired shear stress locations.

The presence and location of seeded cells, as well as the point of observation, are critical. Interestingly, computational model predictions of imparted shear stresses increase by almost three-fold when cells are accounted for in flow geometry delineation; this corroborates data reported in the literature[45]. Furthermore, it challenges theories of mechanotransduction that are based strongly on "known" discrepancies between *in vitro* and *in vivo* stress regimes, since presumed controlled stress regimes *in vitro* are likely to be different than those applied in these theories. Spatial variance in target stresses underscore this point. Based on the data of this study, there is significant spatial variance in shear stresses from the target value and there may only be a small area within the chamber in which the desired stresses are imparted. Hence, the assumption that stresses found in the center of the chamber accurately reflect the target value may be invalid. However, flow field simulations provide insight into local stresses imparted at cell surfaces, providing a unique perspective for elucidating mechanotransduction at the cellular level. If one is aware that stresses vary spatially within and between chambers, flow simulation models could be exploited to identify relevant areas of interest for specific outcome measures.

This study was implemented using a target shear stress of 1 and 10 dyn/cm^2, and the results found for the chambers were comparable to this value. However, the actual stress felt by osteoblasts and osteocytes *in vivo* remains unclear, and a large range of stresses has been applied in past studies. Furthermore, flow chambers are used in a wide variety of experiments with different kinds of cells. For example, endothelial cells have

been subjected to shear stresses around 20 dyn/cm^2 [31,34,44]. At this value, simulations for the chambers examined in this study showed a significant increase in the range of shear stresses experienced. Thus, it can be inferred that, as target stresses are increased, the effects on flow profiles and shear ranges would be amplified and problems inherent to identifying the location of the target stress location would increase as well. Therefore, the effects observed in these computational and experimental studies are expected to occur for a variety of target stresses.

Potential limitations in this study are derived from the fact that it is by nature a computational study which was validated experimentally using a steady flow condition. However, the simulations presented in this study are accurate, virtual depictions of the three commercial devices in use and allow for elucidation of flow regimes that would not be possible with current experimental fluid dynamics methods. A further limitation of the study was the idealization of the cell monolayer as an evenly spaced array of rigid, spheroid bodies, excluding detailed cellular structures. In addition, the cells were modeled as static entities, *i.e.* the model did not account for adaptation in cell structure or realignment of groups of cells with time, both of which have been observed experimentally in response to flow. Nonetheless, inclusion of the monolayer in the computational model resulted in prediction of shear stress magnitudes consistent with those reported in the literature for a similar geometry and setup[45].

With regard to the experimental studies, potential limitations were inherent to idealizations used in implementing the μPIV protocol and within the flow chambers themselves. Due to the size of the particles relative to the cells, it was not feasible to use μPIV to observe deviations in the flow attributable to the presence of the cell monolayer.

Furthermore, when implementing all three commercial chambers, it was difficult to prevent completely leakage around the flow channels. Leakage reduces the effective flow rate through the channel (versus what is applied via the pump), and thereby reduces shear rates. In addition, for two of the chambers, the inlet and outlet areas were so small as to necessitate small caliber tubing that was prone to collapse and difficult to manipulate; this small diameter tubing was prone to very high fluid pressures, which sometimes caused the tubing to disengage from either the inlet/outlet or the syringe, resulting in persistent fluid leakage. Choice of gasket thickness could also influence both computational and experimental results as well and further complicate the targeting of particular flow or stress regimes. Finally, the formation of air bubbles appeared to be inherent to implementation of the types of parallel plate flow chambers studied in combination with a syringe pump; not only do such bubbles have the potential to disrupt the biochemical environment of the cells seeded in the chamber, but they also have the potential to disrupt the mechanical environment of the cells. In carrying out these studies, every effort was made to mitigate bubble formation and experiments were repeated if bubble formation was observed to disrupt flow.

The results of this study challenge the basic premise of *in vitro* mechanotransduction studies, *i.e.* a controlled flow regime is applied to impart a defined mechanical stimulus to cells, even if it is not always possible to insure that the flow regimes are purely physiologic. In fact, flow regimes found in commercially available perfusion chambers are not constant and shear stresses that are imparted to cells are location dependent at the cellular level. Hence, cells on one side of a chamber may experience a different stress than those on the opposite side. This complicates the

elucidation of cellular mechanisms of mechanotransduction. Furthermore, these flow fields differ between chambers as well; according to their geometry and set flow rate. This further exacerbates meaningful elucidation of mechanotransduction mechanisms through comparison of studies conducted with different chamber designs. At the very least, this study underscores the importance of calibrating devices to achieve stress magnitudes near targeted stress levels. From a broader perspective, by coupling computational fluid dynamics with cell biology, new approaches can be developed to overcome limitations of the current technology. Thereby, the impact of *in vitro* studies will be increased and data from different laboratories will be able to be compared, which could greatly increase the impact of cell biology research.

ACKNOWLEDGEMENTS

This study has been funded in part from grants from the National Institutes of Health (ARO50594-01), NASA John Glenn Bioscience and Engineering Consortium (JGBEC NCC3-1008) and the National Center for Microgravity Research. The authors would like to acknowledge and thank Dr. Greg Zimmerli, and Ms. Josée Adamson for their suggestions and support. MLO-Y4 cells and culture protocols were generously provided by Linda Bonewald, PhD, at the University of Missouri – Kansas City. This investigation was conducted in a facility constructed with support from Research Facilities Improvement Program Grant Number C06 RR12463-01 from the National Center for Research Resources, National Institutes of Health.

REFERENCES

1. Papadaki M, Eskin SG, 1997. Effects of fluid shear stress on gene regulation of vascular cells. Biotechnol Prog 13:209-221.

2. Pavalko FM, Chen NX, Turner CH, Burr DB, Atkinson S, Hsieh YF, Qiu J, Duncan RL, 1998. Fluid shear-induced mechanical signaling in MC3T3-E1 osteoblasts requires cytoskeleton-integrin interactions. Am J Physiol 275:C1591-C1601.

3. Guo P, Weinstein AM, Weinbaum S, 2000. A hydrodynamic mechanosensory hypothesis for brush border microvilli. Am J Physiol Renal Physiol 279:F698-F712.

4. Birukov KG, Birukova AA, Dudek SM, Verin AD, Crow MT, Zhan X, DePaola N, Garcia JG, 2002. Shear stress-mediated cytoskeletal remodeling and cortactin translocation in pulmonary endothelial cells. Am J Respir Cell Mol Biol 26:453-464.

5. Rectenwald JE, Moldawer LL, Huber TS, Seeger JM, Ozaki CK, 2000. Direct evidence for cytokine involvement in neointimal hyperplasia. Circulation 102:1697-1702.

6. Tedgui A, Mallat Z, 2001. Anti-inflammatory mechanisms in the vascular wall. Circ Res 88:877-887.

7. Wolpert L, 1969. Positional information and the spatial pattern of cellular differentiation. J Theor Biol 25:1-47.

8. Crick F, 1970. Diffusion in embryogenesis. Nature 5231:420-422.

9. Knothe Tate ML, Niederer P, 1998. Theoretical FE-based model developed to predict the relative contribution of convective and diffusive transport mechanisms for the maintenance of local equilibria within cortical bone. Adv Heat Mass Trans Biotech (ASME) 362:133-142.

10. Tami AE, Nasser P, Verborgt O, Schaffler MB, Knothe Tate ML, 2002. The role of interstitial fluid flow in the remodeling response to fatigue loading. J Bone Miner Res 17:2030-2037.

11. Mishra S, Knothe Tate ML, 2003. Effect of lacunocanalicular architecture on hydraulic conductance in bone tissue: Implications for bone health and evolution. Anat Rec 273A:752-762.

12. Wilkinson JC, Stein RA, Guyer CA, Beechem JM, Staros JV, 2001. Real-time kinetics of ligand/cell surface receptor interactions in living cells: binding of epidermal growth factor to the epidermal growth factor receptor. Biochemistry 40:10230-10242.

13. Funyu J, Mochida S, Inao M, Matsui A, Fujiwara K, 2001. VEGF can act as vascular permeability factor in the hepatic sinusoids through upregulation of porosity of endothelial cells. Biochem Biophys Res Commun 280:481-485.

14. Cinamon G, Alon R, 2003. A real time in vitro assay for studying leukocyte transendothelial migration under physiological flow conditions. J Immunol Methods 27:53-62.

15. Tsuji T, Kawada Y, Kai-Murozono M, Komatsu S, Han SA, Takeuchi K, Mizushima H, Miyazaki K, Irimura T, 2002. Regulation of melanoma cell migration and invasion by laminin-5 and alpha3beta1 integrin (VLA-3). Clin Exp Metastasis 19:127-134.

16. Berthiaume F, Aparicio CL, Eungdamrong J, Yarmush ML, 1999. Age- and disease-related decline in immune function: an opportunity for "thymus-boosting" therapies. Tissue Eng 5:499-514.

17. Kamm RD, 2002. Cellular fluid mechanics. Annual Review of Fluid Mechanics 34:211-232.

18. Knothe Tate ML, 2003. "Whither flows the fluid in bone?" An osteocyte's perspective. J Biomech 36:1409-1424.

19. Frangos JA, McIntire LV, Eskin SG, 1988. Shear stress induced stimulation of mammalian cell metabolism. Biotech Bioeng 32:1053-1060.

20. Hung CT, Pollack SR, Reilly TM, Brighton CT, 1995. Real-time calcium response of cultured bone cells to fluid flow. Clin Orthop 313:256-269.

21. Jacobs CR, Yellowley CE, Davis BR, Zhou Z, Cimbala JM, Donahue HJ, 1998. Differential effect of steady versus oscillating flow on bone cells. J Biomech 31:969-976.

22. Allen FD, Hung CT, Pollack SR, Brighton CT, 2000. Serum modulates the intracellular calcium response of primary cultured bone cells to shear flow. J Biomech 33:1585-1591.

23. Donahue SW, Donahue HJ, Jacobs CR, 2003. Osteoblastic cells have refractory periods for fluid-flow-induced intracellular calcium oscillations for short bouts of flow and display multiple low-magnitude oscillations during long-term flow. J Biomech 36:35-43.

24. Salih V, Greenwald SE, Chong CF, Coumbe A, Berry CL, 1992. The development of an in-vitro perfusion system for studies on cultured cells. Int J Exp Pathol 73:625-632.

25. Busscher HJ, van der Mei HC, 1995. Use of flow chamber devices and image analysis methods to study microbial adhesion. Methods Enzymol 253:455-77.

26. Brown DC, Larson RS, 2001. Improvements to parallel plate flow chambers to reduce reagent and cellular requirements. BMC Immunol 2:9.

27. Chotard-Ghodsnia R, Drochon A, Grebe R: A new flow chamber for the study of shear stress and transmural pressure upon cells adhering to a porous biomaterial. J Biomech Eng 2002, 124:258-261.

28. Sorkin AM, Dee KC, Knothe Tate ML, 2004. "Culture shock" from the bone cell's perspective: emulating physiological conditions for mechanobiological investigations. Am J Physiol Cell Physiol 287:C1527-36.

29. Nauman EA, Satcher RL, Keaveny TM, Halloran BP, Bikle DD, 2001. Osteoblasts respond to pulsatile fluid flow with short-term increases in PGE(2) but no change in mineralization. J Appl Physiol 90:1849-1854.

30. Pavalko FM, Gerard RL, Ponik SM, Gallagher PJ, Jin Y, Norvell SM, 2003. Fluid shear stress inhibits TNF-alpha-induced apoptosis in osteoblasts: a role for fluid shear stress-induced activation of PI3-kinase and inhibition of caspase-3. J Cell Physiol 194:194-205.

31. Butler PJ, Norwich G, Weinbaum S, Chien S, 2001. Shear stress induces a time- and position-dependent increase in endothelial cell membrane fluidity. Am J Physiol Cell Physiol 280:C962-C969.

32. Yellowley CE, Jacobs CR, Donahue HJ, 1999. Mechanisms contributing to fluid-flow-induced Ca2+ mobilization in articular chondrocytes. J Cell Physiol 80:402-408.

33. Archambault JM, Elfervig-Wall MK, Tsuzaki M, Herzog W, Banes AJ, 2002. Rabbit tendon cells produce MMP-3 in response to fluid flow without significant calcium transients. J Biomech 35:303-309.

34. Albuquerque ML, Flozak AS, 2003. Lamellipodial motility in wounded endothelial cells exposed to physiologic flow is associated with different patterns of beta1-integrin and vinculin localization. J Cell Physiol 195:50-60.

35. Forlow SB, McEver RP, Nollert MU, 2000. Leukocyte-leukocyte interactions mediated by platelet microparticles under flow. Blood 95:1317-1323.

36. Essig M, Friedlander G, 2003. Shear-stress-responsive signal transduction mechanisms in renal proximal tubule cells. Curr Opin Nephrol Hypertens 12:31-34.

37. Bilek AM, Dee KC, Gaver DP III, 2003. Mechanisms of surface-tension-induced epithelial cell damage in a model of pulmonary airway reopening. J Appl Physiol 94:770-783.

38. Goldstein AS, DiMilla PA, 2002. Effect of adsorbed fibronectin concentration on cell adhesion and deformation under shear on hydrophobic surfaces. J Biomed Mater Res 59:665-675.

39. Koerner RJ, Butterworth LA, Mayer IV, Dasbach R, Busscher HJ, 2002. Bacterial adhesion to titanium-oxy-nitride (TiNOX) coatings with different resistivities: a novel approach for the development of biomaterials. Biomaterials 23:2835-2840.

40. Kumar TR, Krishnan LK, 2002. A stable matrix for generation of tissue-engineered nonthrombogenic vascular grafts. Tissue Eng 8:763-770.

41. Hildebrand G, Kunze S, Driver M, 2001. Blood cell adhesion on sensor materials studied by light, scanning electron, and atomic-force microscopy. Ann Biomed Eng 29:1100-1105.

42. Knothe Tate ML, Knothe U, 2000. An ex vivo model to study transport processes and fluid flow in loaded bone. J Biomech 33:247-254.

43. Knothe Tate ML, Adamson JR, Tami AE, Bauer TW, 2004. The osteocyte. Int J Biochem Cell Biol 36:1-8.

44. Younis HF, Kaazempur-Mofrad MR, Chung C, Chan RC, Kamm RD, 2003. Computational analysis of the effects of exercise on hemodynamics in the carotid bifurcation. Ann Biomed Eng 31:995-1006.

45. Gaver DP, Kute SM, 1998. A theoretical model study of the influence of fluid stresses on a cell adhering to a microchannel wall. Biophys J 75:721-733.

46. Jacobs CR, Yellowley CE, Davis BR, Zhou Z, Cimbala JM, Donahue HJ, 1998. Differential effect of steady versus oscillating flow on bone cells. J Biomech 31:969-976.

47. Fukushima S, Natatsu A, Kaibara M, Oka K, Tanishita K, 2001. Measurement of surface topography of endothelial cell and wall shear stress distribution on the cell. JSME 44(c):972-981.

48. Bakker DP, van der Plaats A, Verkerke GJ, Busscher HJ, van der Mei HC, 2003. Comparison of velocity profiles for different flow chamber designs used in studies of microbial adhesion to surfaces. Appl Environ Microbiol 69: 6280-7.

49. McCann JA, Peterson SD, Plesniak MW, Webster TJ, Haberstroh KM, 2005. Non-uniform flow behavior in a parallel plate flow chamber : alters endothelial cell responses. Ann Biomed Eng 33: 328-36.

50. Pozrikidis C, 1997. Shear flow over a protuberance on a plane wall. J Eng Math 31:29-42.

51. Anderson EJ, Knothe Tate ML, 2004. Performance evaluation of three cell flow chambers: How well is stress controlled at the cellular level? Euro Soc Biom 353.

52. Anderson EJ, Knothe Tate ML, 2004. Performance evaluation of four cell flow chambers: How well is stress controlled at the cellular level? ASME IMECE 2004:61432.

CHAPTER 6

Characterization and optimization of tissue engineering scaffold architectures and flow regimes for cell cultivation

Eric J. Anderson[1], Melissa L. Knothe Tate[1,2]

[1]Dept. of Mechanical & Aerospace Engineering, Case Western Reserve University, Cleveland, OH
[2]Dept. of Biomedical Engineering, Case Western Reserve University, Cleveland, OH

To be submitted to *Tissue Engineering*

ABSTRACT

Tissue engineering scaffolds are designed to provide a controlled environment for cell migration and proliferation in order to promote tissue infiltration as well as *de novo* tissue formation. Through optimization of scaffold geometry design it is possible to exploit scaffolds as delivery devices for chemical and mechanical signals to guide the infiltration, attachment, differentiation and/or secretion of extracellular matrix by cells seeded within. The purpose of this study is to provide a technological platform as a first step to optimize scaffold geometries for this purpose. Specifically, computational fluid dynamics models were developed to quantify the effect that deviations between target and actual scaffold geometries have on global and local flow regimes within. A range of geometric variance from target prototype scaffold geometries was simulated. For the prototype design studied, a 25% reduction in the diameter of the dominant flow channels resulted in a 75% reduction in scaffold permeability. This approach offers a new

technological tool for virtual prediction of geometric variance effects on scaffold permeability, as well as local velocity and shear stresses within scaffold flow channels. This allows for future characterization and optimization of scaffold geometries to deliver targeted mechanical and chemical signals and obviates the need for iterative prototyping and experimental measures.

INTRODUCTION

Fabrication of three-dimensional scaffolds for cell-seeding and subsequent implantation has become an increasingly important multifunctional tissue engineering approach for bridging or immediate infilling of massive tissue defects. Recently tissue engineers have begun to exploit biophysical principles of transport and mechanics to produce scaffolds[3-9] that provide a microenvironment conductive to cell infiltration (seeding) and cultivation. In addition, the concept of design optimization has been applied to define rapid prototyped[10], biodegradable scaffold geometries to meet both solid structural (mechanical) and mass transport specifications. Furthermore, fluid flow has been applied empirically to augment perfusion of bioreactor medium to cells within three-dimensional scaffolds, and computational simulations have been used to estimate shear stresses imparted to cells during flow[11-16]. Computational fluid dynamics calculations of the flow environment within scaffolds provide not only a new measure for prediction of scaffold performance but also a new enabling technology for the optimization of scaffolds as delivery devices for mechanical and chemical signals to guide differentiation, proliferation and extracellular matrix production by cells seeded within[17-20].

Through mass and fluid transport, scaffolds interact mechano-chemo-biologically with the surrounding environment to enhance cell migration and proliferation. The geometry and dimensions of scaffold microstructure are critical for optimization of fluid transport and permeability in the scaffold, which influence cell viability throughout the volume of tissue that is to be regenerated[21]. The degree to which small variations from target scaffold geometries, introduced during manufacturing, influence flow properties through scaffolds has not been described previously. Although manufacturing specifications allow for small deviations that may not affect global flow regimes or other scaffold performance parameters, it is not clear the degree to which such deviations affect flow regimes at the cellular length scale. It is hypothesized that small deviations from target geometries can have a significant impact not only on scaffold permeability (a bulk property), but also on forces imparted by fluid flow to cells seeded within.

Yet, it is not known to what degree rapid prototyped scaffolds meet technical specifications required to impart the desired flow environment to cells seeded within. Furthermore, no design tool is available to optimize porosity and permeability of scaffolds for specific defect geometries. Thus, the goal of this study was to provide a tool to analyze flow regimes in a tissue-engineered scaffold and optimize scaffold architecture to produce local (nm-μm) flow fields modulating migration, adhesion, and mechanotransduction in cells seeded on the scaffold surfaces, as well as define global flow parameters (μm-mm) that are applied to the scaffold to enhance directed cell infiltration (seeding) and to augment mass transport in diffusion-compromised remote regions.

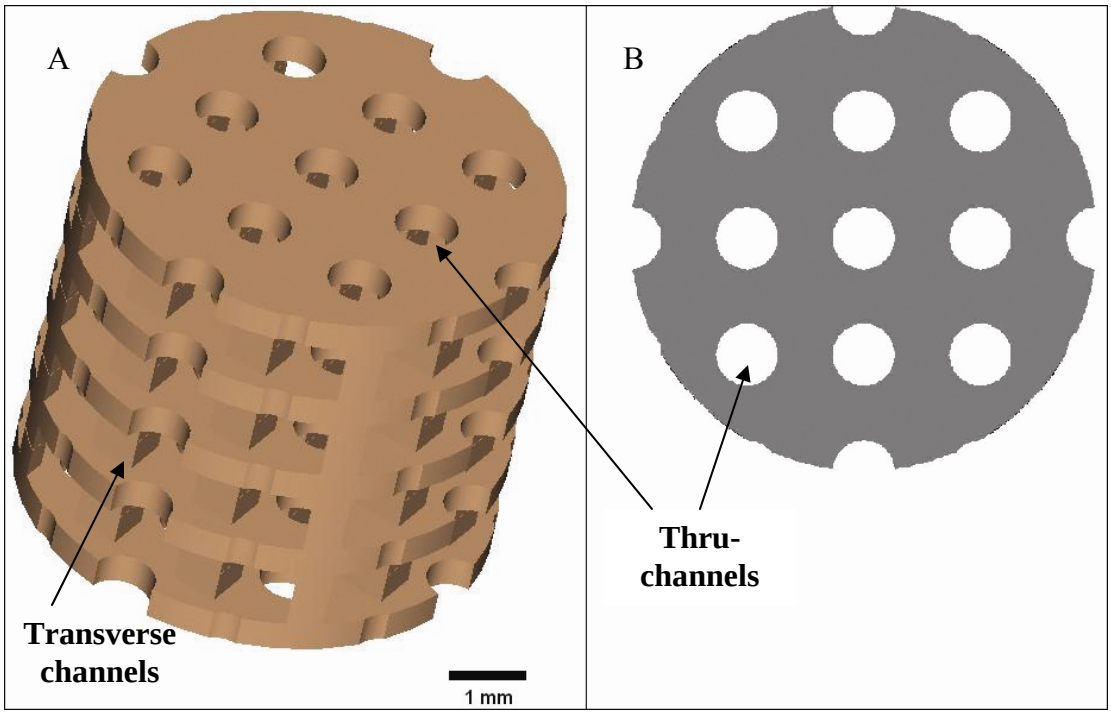

Figure 6.1: Example of a target design geometry for tissue engineering scaffold, adapted from a design by Professor Malcolm Cooke, University of Texas at El Paso. (a) Computer model before rapid-prototyping, contains nine longitudinal channels and seven transverse layers; CAD image courtesy of Professor Malcolm Cooke. (b) Transverse plane of cylindrical scaffold showing dominant through channels in the axial direction.

METHODS

A scaffold with two different pore sizes and geometries was chosen to test the feasibilility of virtual permeability and flow characterization testing with deviation from target design geometry as the independent variable. This scaffold design, conceived by Professor Malcolm Cooke for bone tissue engineering applications[29,30], was designed to incorporate relatively large thru channels (0.8 mm in diameter) "for rapid tissue penetration"[22] and smaller order local transverse channels (0.4 × 0.9 × 0.6 mm) for "tissue development". This particular scaffold design is particularly suited to be adapted for patient specific defect geometries based on magnetic resonance imaging or computerized tomography. Furthermore, the design is particularly applicable as a testbed for the permeability and flow regime analyses presented here, as it has two orders of magnitude of length scale, in

which respective global and local fluid flow regimes will develop when the scaffold is placed in a bioreactor or *in situ*.

Scaffold creation

Scaffolds comprising a three-dimensional layered cylinder with nine circular and four semi-circular channels in the longitudinal direction were created using a solid modeling program (Pro/Engineer, PTC) and fabricated out of poly(propylene fumarate), PPF, using a stereolithography (SLA) rapid prototyping machine (3D Systems, Valencia, CA). All longitudinal channels within the scaffold are considered to be the primary flow direction and are connected through seven transverse channels that make up a secondary flow direction (Fig. 6.1). The actual geometries of the prototyped scaffolds (n = 4) were obtained using μCT imaging (700 slices, resolution = 12 μm), where a reconstructed three-dimensional image of the prototyped geometry was compared with the target geometry in order to characterize discrepancies between structures (Fig. 6.2). Overall, major differences between the actual and prototyped designs are found in the primary flow direction (longitudinal channels), and thus variations in the characteristic diameter of these channels was the main independent variable for fluids analysis in this study.

Mesh creation

To predict flow through the target design as well as actual prototyped scaffolds, a computational mesh of the scaffold fluid space was created for both cases (ESI-CFD, Huntsville, AL). In order to estimate the effects of nonconformance with specifications, *i.e.* variance between the target and actual geometries, geometric deviations were modeled by reducing diameters of the longitudinal channels iteratively (100% - 0%, in

Figure 6.2: Micro-CT image of a scaffold fabricated using stereolithography (rapid-prototyping). Image courtesy of Professor David Dean, Case Western Reserve University.

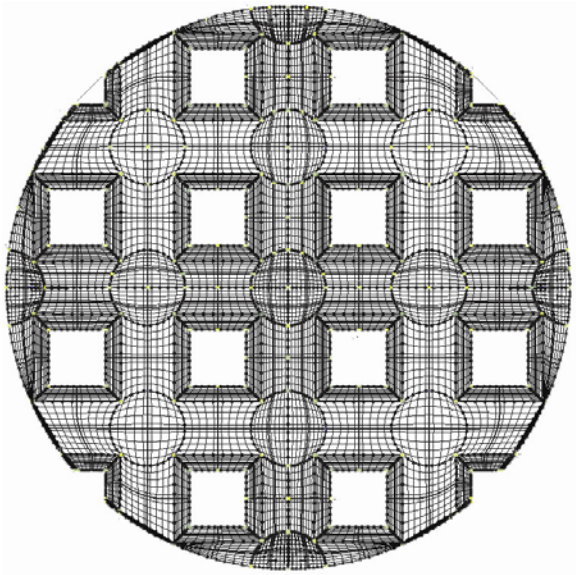

Figure 6.3: Computational mesh of target design geometry for fluid dynamic simulation; longitudinal channels are rendered at 100, 75, 50, and 25% of target channel diameter to simulate increasing channel occlusions that are observed experimentally.

25% increments). These deviations were typical of those in actual rapid prototyped models (Fig. 6.3). For all models, the nodal-mesh contained a three-dimensional structured grid in order to represent the fluid space, where grid independence was ensured through parametric analysis. The resultant mesh density for all models is 179,334 cells, where the reduction in channel diameter (prototyped geometries) yields a decrease in cell volume but not in the cell (mesh) density.

Computational fluid dynamics

For all models, computational fluid dynamics is used to predict flow in the target and actual scaffold geometries (CFD-ACE, ESI-CFD, Huntsville, AL). A 2nd order upwind discretization scheme is used to calculate flow from the Continuity Equation (1) and Navier-Stokes' Equations (2) in three-dimensions,

$$\nabla \cdot V = 0 \tag{1}$$

$$\rho\left(V \cdot \nabla V\right) = -\nabla P + \mu \nabla^2 V \tag{2}$$

where V is the velocity vector, ρ is density, P is pressure, and μ is viscosity. Pressure and velocity are decoupled by linear interpolation for each volume, and any instabilities are eliminated through an average of the Navier-Stokes' equations at each volume face as well as a relation between the face velocity and imparted pressure gradient. Finally, the wall shear stress is also determined throughout the scaffold, as cells attached to scaffold walls are dependent on the imparted shear stress for necessary stimulation and proliferation. The stress that would be imparted to cells seeded within the scaffold is calculated at the walls based on the viscosity and strain rate,

$$\tau_w = \mu \dot{\gamma} \tag{3}$$

where τ_w is the wall shear stress, μ is viscosity, and $\dot{\gamma}$ is the strain rate.

For all simulations, flow is induced in the longitudinal direction of the scaffold, which is the direction for which the scaffold is designed. The perfusion medium is to be slightly more viscous than water at 37°C (taken from physiology of the lacunocanalicular network[21]) with the appropriate fluid properties: μ = 0.001 kg/ms, ρ = 993 kg/m^3. No-slip boundary conditions are implemented on all scaffold surfaces, as well as on the rounded sides of the scaffold which are sealed to restrict flow from entering/exiting in the

transverse direction. Thus, flow is induced through the top and bottom circular surfaces, designated as the inlet and outlet, where an applied pressure drop is given to impart a shear stress similar to that required for osteoblast stimulation (5 - 10 dyn/cm^2)[28] to cells seeded within the transverse layers of the scaffold[23,24]. Simulations are run for steady-state (velocity time-derivatives are zero) with a rigid, non-deforming scaffold, until convergence is reached for a criterion of 0.00001.

Because scaffold designs are based on specific flow parameters used to enhance cell migration and proliferation, the change in these parameters resulting from geometrical discrepancies is expected to change scaffold performance. In order to evaluate performance with respect to global design parameters, flow simulations are used to calculate permeability in the longitudinal direction for each case. Based on the mass flow rate calculated in the fluid simulation of each scaffold, permeability is determined as a function of longitudinal channel diameter using Darcy's Law (4)

$$k = \frac{\dot{m}\,\mu\,L}{A_{cs}\,\rho\,P_{inlet}} \tag{4}$$

where k is permeability (m^2), $\dot{m}$ is mass flow rate, μ is viscosity, L = 5.2 mm is the scaffold length, A_{cs} = 28.3 mm^2 is cross-sectional area of the scaffold, ρ is density, and P_{inlet} = 100 Pa is the applied inlet pressure (where P_{outlet} = 0).

RESULTS

Flow simulations in the given scaffold geometry are performed to characterize the fluid environment of the target design. A pressure drop (ΔP = 100 Pa) is applied to induce shear stresses in transverse channels on the order of magnitude as those applied in *in vitro*

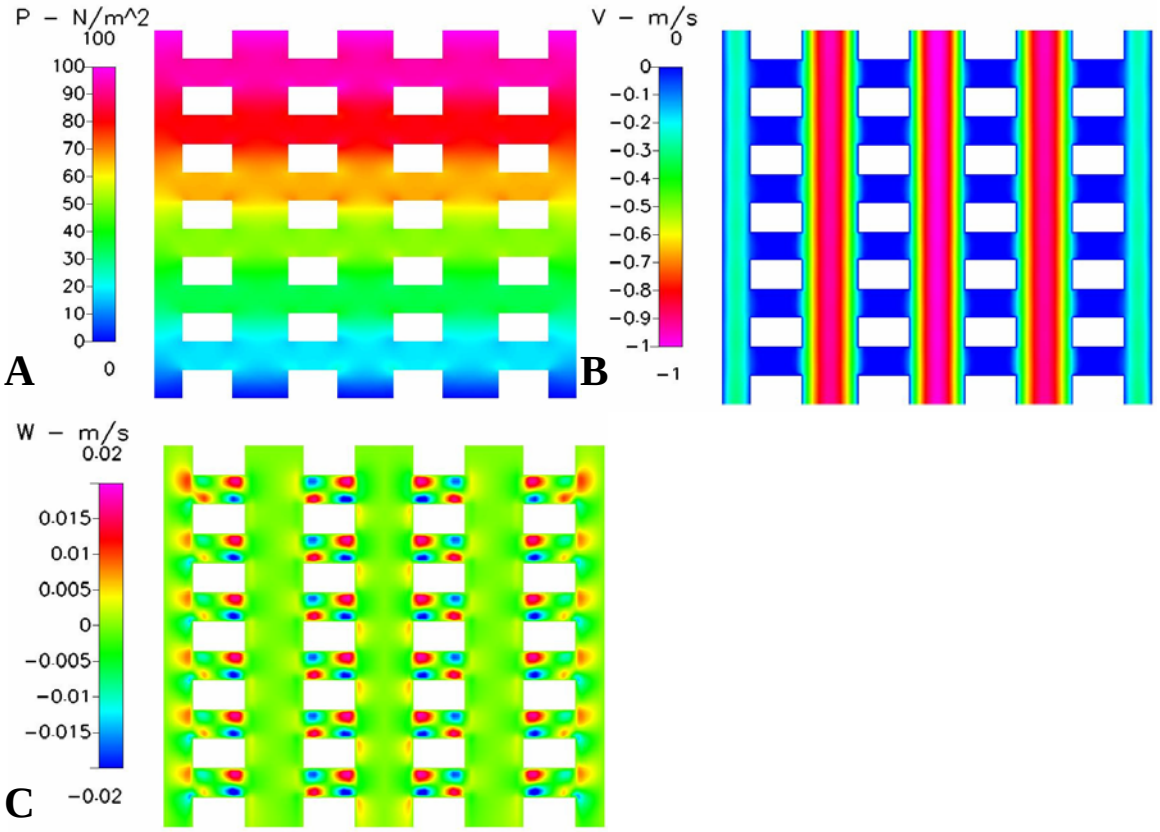

Figure 6.4: Target design simulation: (a) pressure gradient, (b) axial (top to bottom) velocity, (c) transverse (left to right) velocity, in given centered cross-section of scaffold geometry.

osteoblast mechanotransduction studies[28]. The resulting pressure gradient within the scaffold is nearly linear with respect to the longitudinal direction (Fig. 6.4a). The axial velocity is maximal in the longitudinal channels and resembles the analytic velocity profile for pressure-induced pipe flow[25] (Fig. 6.4b). For a cross-section at the midplane of the scaffold, axial velocity peaks at the center of each longitudinal channel (~1 m/s) with the exception of the outer channels in which the walls are considered to be sealed. Deviations from the pipe-flow profile are found at each transverse fluid layer, where expansion causes velocity changes similar to an axisymmetric jet[26]. Consequently, expansion into the transverse layers yields a transverse velocity, and thus a flow in and out of these channels (Fig. 6.4c). For the transverse velocity, circulation zones, similar to

channel-driven cavity flow at low Reynolds number[25], are found in each layer with a maximum velocity of 0.02 m/s (two orders of magnitude lower than the longitudinal channels). The circulation zones are nearly symmetric in the inner layers of the scaffold, where a noticeable reduction in velocity is found in layers adjacent to the sealed scaffold walls.

Due to the resultant velocity magnitudes, shear stresses on the target scaffold differ by an order of magnitude between the longitudinal channels and the transverse layers (Fig. 6.5a). On the inner walls of the longitudinal channels, the regions of maximum velocity, shear stresses approach 60 - 80 dyn/cm^2 for channels at the center of the scaffold. Semi-circular channels that border the sealed walls yield a reduced velocity profile, and thus have wall shear stresses between 30 - 40 dyn/cm^2. However, in the transverse layers, shear stress on the scaffold walls is significantly lower due to the lower order of magnitude transverse velocity. Here, shear stresses on the top and bottom walls of the transverse cavities range from 0 – 10 dyn/cm^2 (Fig. 6.5b).

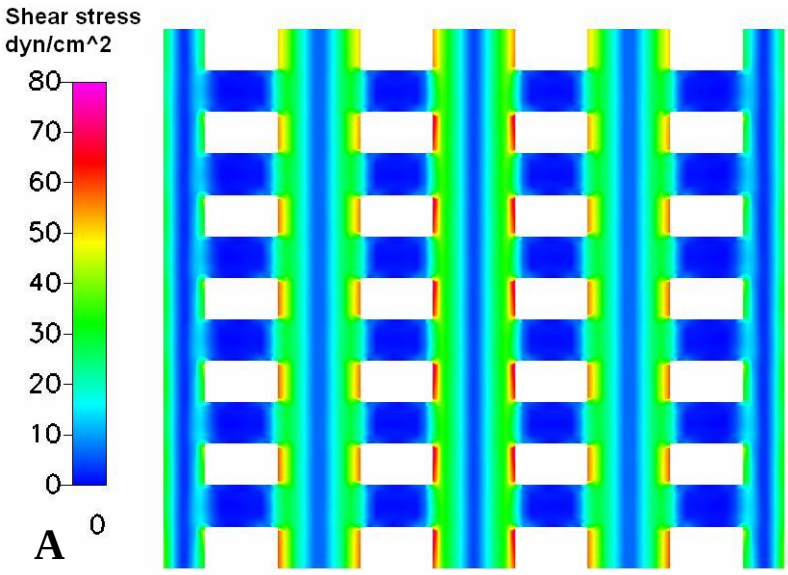

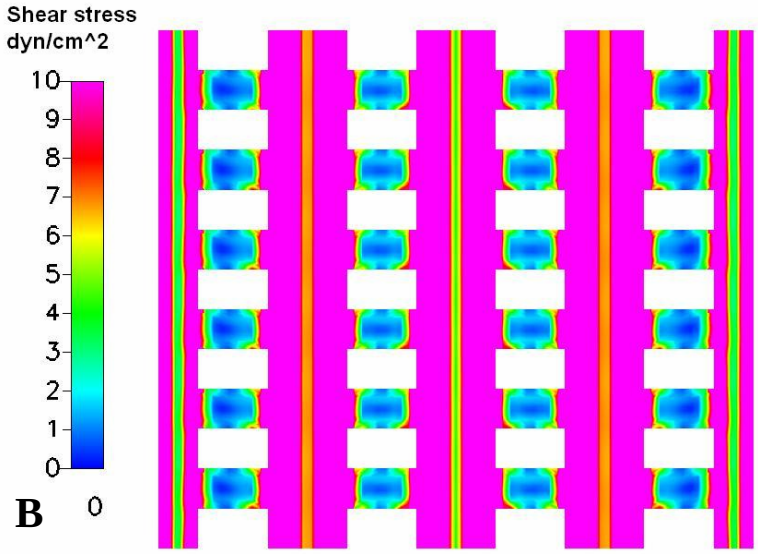

Figure 6.5: Target design simulation: (a) shear stress at high scale (80 dyn/cm^2 in channels), (b) shear stress at low scale range (10 dyn/cm^2 on transverse layer walls).

When the longitudinal channel diameters are reduced to mimic deviations in the prototype geometries from target geometries (e.g. due to manufacturing), velocity magnitudes and shear stresses decrease within the scaffold walls. As the overall channel diameter decreases, the magnitude of axial velocity in the longitudinal channels also decreases due to the expansion from the channels to the transverse layers (Fig. 6.6). For instance, at a 75% reduction in channel diameter, the maximum axial velocity in the channel is reduced by 93% of the target value to 0.07 m/s. In addition, the velocity profiles in the prototyped geometries are periodic with distance from the inlet to outlet of the scaffold, where maximal velocity is found between each transverse layer, *i.e.* when bounded longitudinal channel walls, and axial velocity decreases as it expands into the transverse sections. Thus, the greater the reduction in channel diameter, the greater the volume ratio between the channels and transverse layers or expansion, and hence the differences in velocity are more profound.

In addition to changes in axial velocity, the transverse velocities are also reduced, where associated circulations are shifted from the target design locations (Fig. 6.6). As

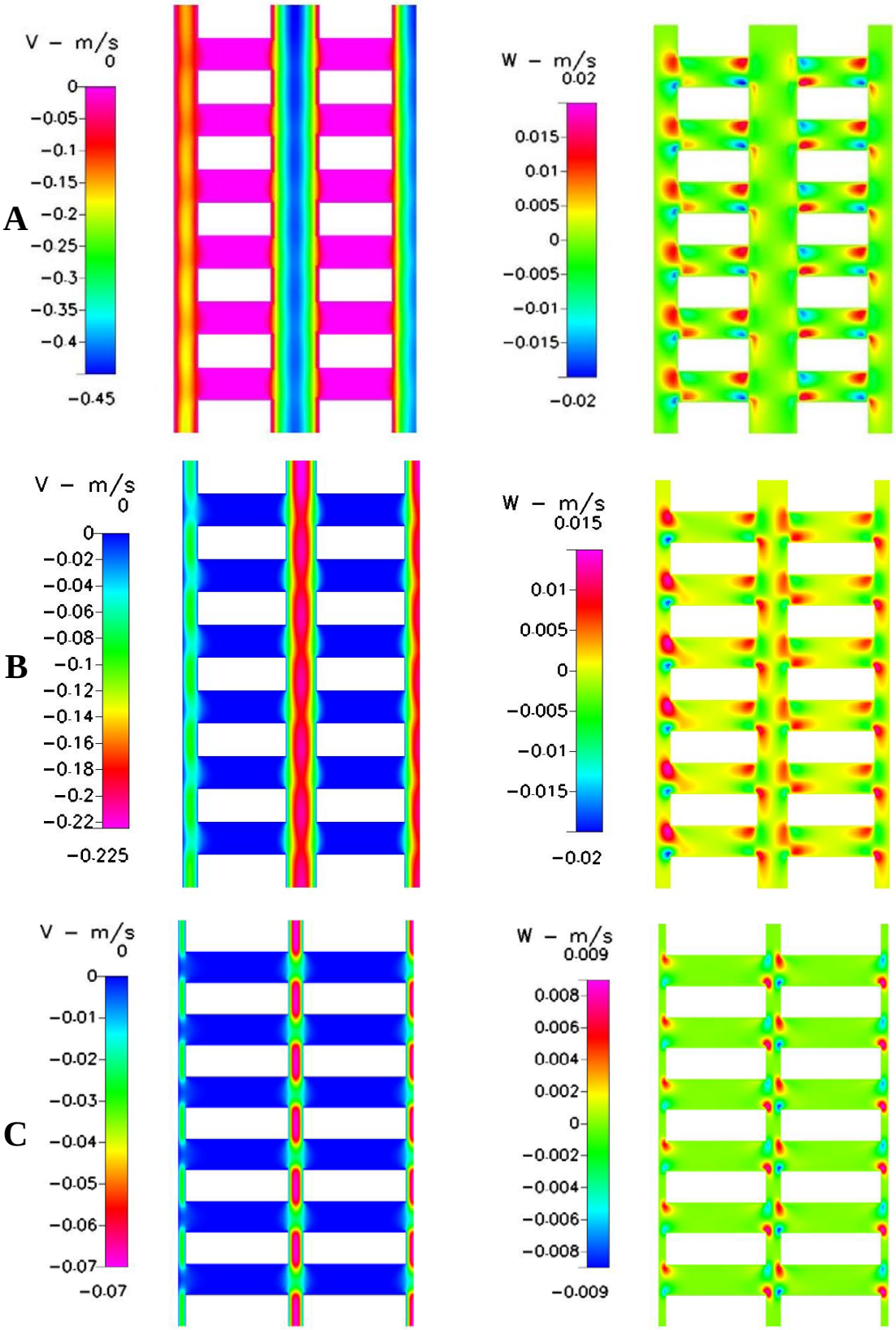

Figure 6.6: Prototyped scaffold simulation, symmetric cross-sections: axial velocity, and transverse velocity in (a) 75%, (b) 50%, and (c) 25% of target channel diameter.

in the axial velocity, expansion into the transverse layers causes the magnitude of transverse velocity to decrease (up to 50%) with decreasing channel diameter. Lengthening in the transverse distance between longitudinal channels (due to diameter reduction), yields both a magnitude reduction in transverse flow as well as circulation zones. As channel diameter decreases, circulating flow in the scaffold is shifted from the transverse layers to the adjacent longitudinal channels, and thus the reason for the periodicity of the axial velocity.

As a result of decreases and shifts in velocity, the resulting shear stress is reduced from the target geometry in both the transverse sections and longitudinal channels (Fig. 6.7a). At a short distance into the transverse layers (0.1 mm), the wall shear stress decreases from 5 dyn/cm^2 in the target case to 3.5, 0.5, and 0.02 dyn/cm^2, with channel diameters of 75%, 50%, and 25% respectively. Hence, as the distance between longitudinal channels increases, the area of high mechanical stimulation, or shear stress, in the transverse layers decreases. Furthermore, the wall shear stress in the longitudinal channels (in between the transverse layers) also decreases from the target value of 80 dyn/cm^2 (in circular channels) to nearly 10 dyn/cm^2 at a channel diameter of 25%.

Finally, as the calculated permeability depends strongly on the area available to flow, reductions in velocities throughout the scaffold, and thus mass flow rate cause the overall scaffold permeability to decrease with channel diameter (Fig. 6.7b). For a normalized permeability, with respect to the target value, decreases in the channel diameter or cross-sectional flow area cause a dramatic decrease in scaffold permeability. Hence, at 75% of the target channel diameter (or 25% reduction), the scaffold permeability is reduced to nearly 20% of the target value. Since intrinsic permeability is

independent of pressure at the desired range, the change in channel diameter, and cross-sectional flow area, causes a decrease in the mass flow rate through the scaffold, thus reducing global permeability.

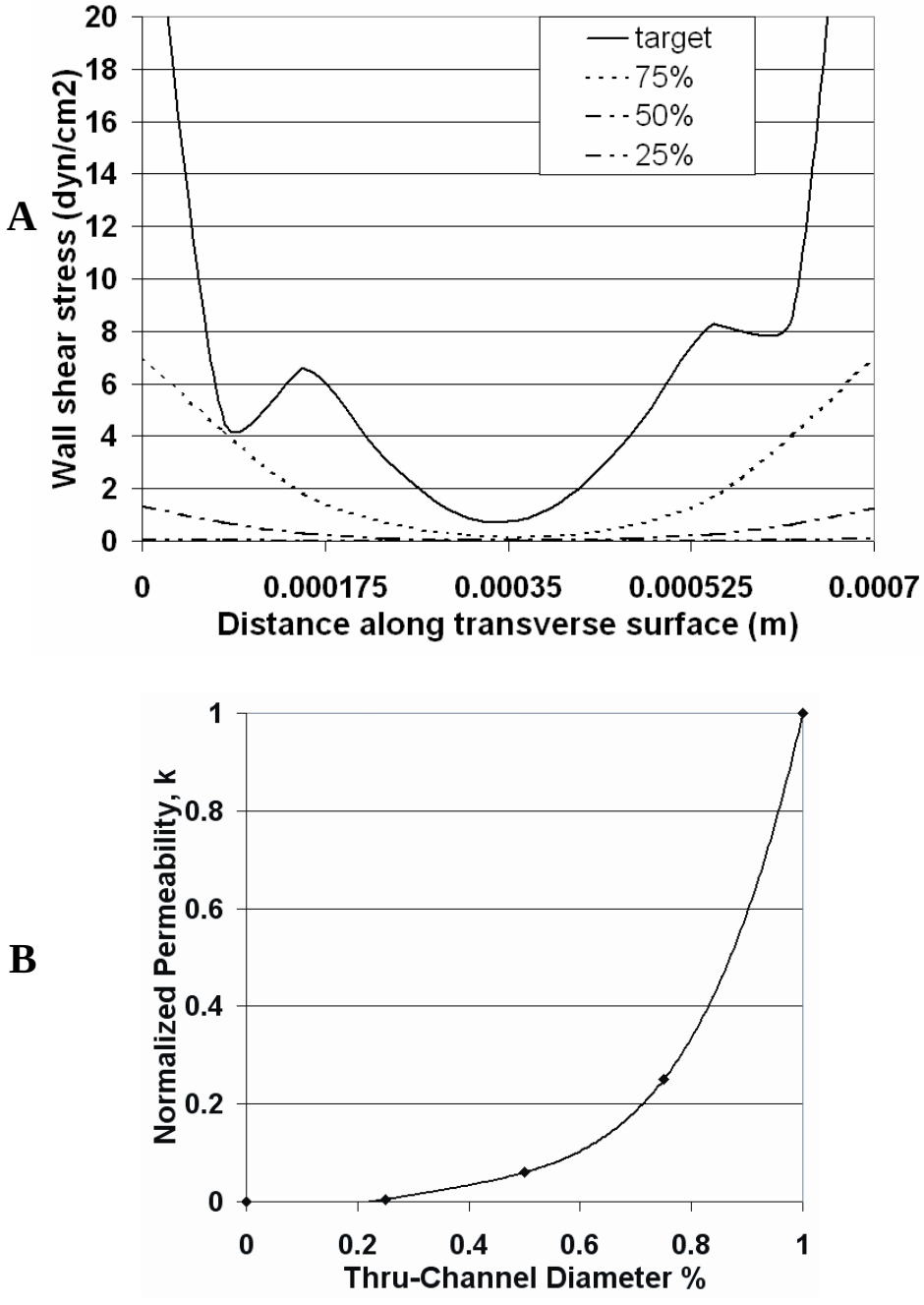

Figure 6.7: Comparison between target and prototype geometries: (a) wall shear stress in transverse layers, (b) calculated overall scaffold permeability, for the target, 75, 50, and 25% channel diameter models.

DISCUSSION

Fabrication of three-dimensional scaffolds for cell-seeding and implantation has become an increasingly important tissue engineering approach for bridging massive tissue defects. Scaffolds are designed to provide a mechanically and biochemically controlled milieu for cell seeding or ingrowth, matrix formation, and tissue regeneration, within the prevailing tissue environment where they are implanted[27]. The microarchitecture of the scaffold design provides a specific geometry to obtain desired flow parameters such as flow rate, shear stress, flow direction, and permeability. However, this study demonstrates that variance from target geometry influences not only the local flow environment (*i.e.* cell-level) within the scaffold, but also the permeability of the scaffold as a whole.

Flow simulations through the target scaffold geometry show specific velocity and shear stress distributions that are designed to provide an optimal environment for cell migration and proliferation. The large longitudinal channels of the scaffold are high-flow areas in which transport occurs at such a rate as to be advantageous to cell infiltration as well as nutrient distribution. Similarly, the high velocity in these sections yields a maximal wall shear stress in which cell attachment would be inhibited and cell infiltration into the scaffold interior would be enhanced during flow. In addition, these channels provide the bulk of the flow through the scaffold, and thus permeability is primarily dependent on their dimension; transverse layers exert a negligible contribution to permeability in comparison. However, these channels feed into the transverse layers of the scaffold, as flow expands into each section much like axisymmetric jet flow. Consequently, the transverse layers have a velocity an order of magnitude less than the

longitudinal channels, and thus wall shear stress in these sections, at surfaces conducive to cell attachment, is decreased (~10 dyn/cm^2 for the given pressure drop). Hence, the low-flow environment of the transverse layers yields circulation zones as well as shear stresses that provide an ideal location for cell attachment and transduction of shear stresses from fluid drag on cell membranes. Overall, the scaffold design can potentially address infiltration through the longitudinal channels as well as attachment, possibly modulating downstream events such as differentiation, proliferation and extracellular matrix secretion by cells within the transverse layers of the scaffold.

However, as deviations between the target design and actual prototype geometries become more dramatic, the actual local and global flow environments in the scaffolds deviate from the desired flow environment as well. Mimicking the iterative occlusion of the longitudinal channel diameter, a reduction in channel diameter yields a reduction in velocity and wall shear stress for both longitudinal channels and transverse layers (up to a 93%, 50%, and 99% decrease in channel velocity, transverse velocity, and transverse stress respectively, for a 75% reduction in diameter). This decrease causes not only a loss in the scaffold's transport capacity, affecting efficiency of cell infiltration and nutrient delivery, but also in the mechanical stimulation of cells through imparted shear stress, which would likely result in decreased tissue development.

Using knowledge of how geometry discrepancies affect flow, permeability of the scaffold can be predicted based on longitudinal channel diameter. Mass flow rates taken from the simulations are used to calculate a permeability that is intrinsic to the material (i.e. not dependent on flow). These permeabilities are then plotted with the appropriate longitudinal channel diameter to create a predictive curve of permeability as a function of

prototype geometry. Thus, measurement of the dominant flow geometry (i.e. longitudinal channels) can yield the estimated performance of the scaffold, as permeability is inherently tied to flow rate, velocity and imparted shear stress. The ability to predict scaffold permeability based on geometric measurements yields a quick tool to optimize structure without the time and expense of prototyping and experimental measurements.

However, since only one scaffold geometry was investigated in this study, certain limitations arise due to the specificity of the fluid environment. Individual evaluations would be necessary to obtain specific details of a given target geometry that is dissimilar to the proposed design. Yet, the methodology of this study can be carried out to optimize the geometry of any scaffold, still reducing the experimentation and production time. Furthermore, geometric discrepancies beyond those of the longitudinal channel dimensions were not taken into account in this study. However, since the longitudinal channels dominate the global flow through the scaffold, or permeability, geometrical variations beyond these defects would be negligible compared to the dominant effects of the longitudinal channels on the overall fluid environment. A similar argument can be made with regard to the inclusion of cells in these models, i.e. changes in flow due to the presence of cells would be negligible compared to effects on the fluid environment. Finally, a limitation may arise from the fact that flow through scaffolds is often unsteady (oscillating, pulsating, etc.); nonetheless, since the calculated permeability is independent of flow, the change in permeability due to occlusion of the channel diameter will persist. Variations will occur in velocity and shear stress, although the varying pressure can be used to determine the unsteady flow rate, velocity, and shear stress from Darcy's Law

and the governing equations. In sum, this study presents a predictive optimization tool that is applicable to any scaffold geometry through which flow occurs, as such it is not dependent solely on the predictions presented herein.

The success of tissue engineering scaffolds in repairing tissue defects depends on the solid characteristics as well as the flow regimes within the design. As the geometry is intended to impart specific velocities, pressures, and stresses within the scaffold, the accuracy of the fabricated structure is integral to overall performance. This study presents a novel design tool to investigate the effect of differences (between design specifications and actual manufactured geometries) on fluid flow and permeability[17-20]. Furthermore, it provides a platform to predict and optimize porosity and permeability of scaffolds for specific geometries, thus reducing the number of experimental studies necessary to validate design performance.

ACKNOWLEDGEMENTS

The scaffold design studied in this feasibility paper was an adaptation of a design developed by Professor Malcolm Cooke, University of Texas at El Paso. The CAD-model of the scaffold and the fabricated PPF was kindly provided by Professor Malcolm Cooke. The PPF used by Dr. Cooke to create the scaffolds was produced by Amit Mistry, Xingfeng Shi, and Dr. Antonios Mikos, Bioengineering Department, Rice University in Houston, Texas. Professor David Dean of the Department of Neurosurgery at Case Western Reserve University provided the micro-computed tomography image of a representative rapid prototyped scaffold; imaging was carried out by Scanco AG in

Bassersdorf, Switzerland. The authors would like to thank Professor Dean for reading and providing suggestions on the final revision of the manuscript. This study was supported by the Presidential Research Initiative at Case Western Reserve University and the National Institutes of Health (AR049351-01). This investigation was conducted in a facility constructed with support from Research Facilities Improvement Program Grant Number C06 RR12463-01 from the National Center for Research Resources, National Institutes of Health.

REFERENCES

1. Hutmacher DW, 2001. Scaffold design and fabrication technologies for engineering tissues-state of the art and future perspectives. J Biomater Scie Polym Edn 12: 107.

2. Hutmacher DW, 2000. Mechanical properties and cell cultural response of polycaprolactone scaffolds designed and fabricated via fused deposition modeling. J Biomed Mater Res 55:203.

3. Mikos AG, Sarakinos G, Lyman MD, Ingber DE, Vacanti JP, Langer R, 1993. Prevascularization of porous biodegradable polymer. Biotechnol Bioeng 42:716.

4. Butler DL, Goldstein SA, Guilak F, 1993. Functional tissue engineering: the role of biomechanics. J Biomech Eng 122:570.

5. Hollister SJ, Maddox RD, Taboas JM, 2002. Optimal design and fabrication of scaffolds to mimic tissue properties and satisfy biological constraints. Biomaterials 23:4095.

6. Hollister SJ, 2005. Porous scaffold design for tissue engineering. Nat Mater 4:518.

7. Howk D, Chu TM, 2006. Design variables for mechanical properties of bone tissue scaffolds. Biomed Sci Instrum 42:278.

8. Adachi T, Osako Y, Tanaka M, Hojo M, Hollister SJ, 2006. Framework for optimal design of porous scaffold microstructure by computational simulation of bone regeneration. Biomaterials 27:3964.

9. Knothe Tate ML, 2006. Multiscale computational engineering of bones: State-of-the-art insights for the future. In: Bronner, F., Farach-Carson, M.C., Mikos, A.G., eds. Engineering of Functional Skeletal Tissues. New York, NY: Springer, pp. 141-159.

10. Chua CK, Leong KF, Cheah CM, Chua SW, 2003. Development of a tissue engineering scaffold structure library for rapid prototyping. Part 2: Parametric library and assembly program. Int J Adv Manuf Technol 21:302.

11. Raimondi MT, Boschetti F, Falcone L, Fiore GB, Remuzzi A, Marazzi M, Marinoni E, Pietrabissa R, 2002. Mechanobiology of engineered cartilage cultured under a quantified fluid dynamic environment. Biomech Modeling Mechanobiol 1:69.

12. Raimondi MT, Boschetti F, Falcone L, Migliavacca F, Remuzzi A, Dubini G, 2004. The effect of media perfusion on three-dimensional cultures of human chondrocytes: Integration of experimental and computational approaches. Biorheology 41:401.

13. Botchwey EA, Pollack SR, Levine EM, Johnston ED, Laurencin CT, 2004. Quantitative analysis of three-dimensional fluid flow in rotating bioreactors for tissue engineering. J Biomed Mater Res A 69:205.

14. Porter B, Zauel R, Stockman H, Guldberg R, Fyhrie D, 2005. 3-D computational modeling of media flow through scaffolds in a perfusion bioreactor. J Biomech 38:543.

15. Boschetti F, Raimondi MT, Migliavacca F, Dubini G, 2006. Prediction of the micro-fluid dynamic environment imposed to three-dimensional engineered cell systems in bioreactors. J Biomech 39:418.

16. Cioffi M, Boschetti F, Raimondi MT, Dubini G, 2006. Modeling evaluation of the fluid-dynamic microenvironment in tissue-engineered constructs: a micro-CT based model. Biotechnol Bioeng 93:500.

17. Anderson EJ, Jackowe DJ, Cooke MN, Savrin JS, Mistry A, Shi X, Rimnac C, Mikos AG, Knothe Tate ML, Dean D, 2005. Permeability and porosity of in vitro degraded, stereolithographically-rendered solid/porous composite poly(propylene fumarate) tissue engineering scaffolds. Abstract presented at the Midwest Tissue Engineering Conference.

18. Anderson EJ, Savrin J, Cooke M, Dean D, Knothe Tate ML, 2005. Evaluation of and optimization of tissue engineering scaffolds using computational fluid dynamics. Abstract presented at the Annual Meeting of the Biomedical Engineering Society, Baltimore, MD. Abstract no. 143471.

19. Anderson EJ, Savrin J, Cooke M, Dean D, Knothe Tate ML, 2005. Performance evaluation of tissue engineering scaffolds – development of a novel tool for optimization of fluid flow & permeability. Abstract presented at the ASME Summer Bioengineering Conference, Vail, CO. Abstract no. 0410280.

20. Anderson EJ, Savrin J, Cooke M, Dean D, Knothe Tate ML, 2006. Optimization of tissue engineering scaffold architectures and flow regimes for cell cultivation. Abstract presented at the Annual Meeting of the Orthopaedic Research Society, Chicago, IL.

21. Knothe Tate ML, 2003. "Whither flows the fluid in bone?" An osteocyte's perspective. J Biomech 36:1409.

22. Griffith LG, Naughton G, 2001. Biomaterials and scaffolds for tissue engineering: Emerging design principles. Ann NY Acad Sci, Proc BECON Conference on Reparative Medicine, 961, 83-95.

23. Anderson EJ, Kaliyamoorthy S, Alexander JID, Knothe Tate ML, 2005. Nano-microscale models of periosteocytic flow show differences in stresses imparted to cell body and processes. Ann Biomed Eng 33:52.

24. Anderson EJ, Falls TS, Sorkin AM, Knothe Tate ML, 2006. The imperative for controlled mechanical stresses in unraveling cellular mechanisms of mechanotransduction. Biomed Eng Online 5:27.

25. White FM, 1991. Viscous Fluid Flow. 2nd ed., McGraw Hill, New York, NY.

26. Schlichting H, 1933. Laminare Strahlenhausbreitung. Z Angew Math Mech 13, 260, 1933.

27. Sikavitsas VI, Bancroft GN, Lemoine JJ, Liebschner MAK, Dauner M, Mikos AG, 2005. Flow perfusion enhances the calcified matrix deposition of marrow stromal cells in biodegradable nonwoven fiber mesh scaffolds. Ann Biomed Eng 33:63.

28. Hung CT, Allen FD, Pollack SR, Brighton CT, 1996. Intracellular Ca^{2+} stores and extracellular Ca^{2+} are required in real-time Ca^{2+} response of bone cells experiencing fluid flow. J Biomech 29:1411-1417.

29. Cooke MN, 2004. Novel stereolithographic manufacture of biodegradable bone tissue scaffolds. Dissertation Abstracts International 0548, Ann Arbor, MI.

30. Gibson LJ, Ashby MF, 1997. Cellular solids: structure and properties. 2nd ed., Cambridge Univ. Press, New York.

CHAPTER 7

Concluding Remarks

For the past century, the relationship between bone's structure and function has been elucidated using experimental and theoretical approaches. Ultimate goals of this research include development of the capacity to grow or repair bone tissue as well as translation of this knowledge to prevent or reverse bone disease. Bone remodeling is a spatiotemporally complex process involving osteocytes, osteoblasts and osteoclasts. Osteocytes are the putative mechanosensors of bone. The coordination and navigation of the cellular events underlying remodeling are the subject of much current research. Specifically, the mechanisms of mechanotransduction in bone, or how external mechanical loads are transduced to osteocytes embedded deep within the tissue, are not yet known.

The movement of the fluid surrounding osteocytes has been hypothesized to play a key role in "carrying" chemical and mechanical signals from the skeletal level, at which forces are transmitted from ground reaction forces, to the cells that adapt the tissue from within. The flow of pericellular fluid cannot be observed *in vivo* due to limitations in current imaging modalities. Hence, computational models have been created to predict flow at various length scales in bone and to elucidate the role of fluid flow in mechanotransduction. However, due to technological limitations and the high complexity of bone tissue, most models comprise highly idealized geometries and are limited to the macroscopic length scale. This results in a gap in understanding of the transduction pathways from the systems, to the organ, tissue and cellular levels.

The work presented here aims to bridge this gap in understanding, and investigates fluid flow in bone from the microscopic perspective, using bottom-up computational and experimental approaches. Using physiologic geometry at the tissue and cellular levels, we have predicted that which cannot be observed or measured directly, and have reached an understanding of the imparted mechanical forces and their locations at micro- and nano-scales. Overall, this research has addressed fluid dynamics at the multiple length scales in bone, thus providing the pathway from previous macro-models down to the cellular level, which is the focal point for bone remodeling.

Beginning with the tissue-level, Chapter 2 linked computational and experimental models to describe flow thru an osteocyte network. These cells, known as the "mechanosensors" of bone, are the essential communication hub for bone remodeling. Thus, measurements of flow at this level are integral to understanding how signals are transduced from external forces. In this pursuit, cellular communication, permeability and signal efficiency are calculated, representing previously undetermined parameters at this length scale in bone. Combined computational fluid dynamics models and scaled-up physical models recreate (virtually and physically) the micro-geometry or tissue-level of bone. This allows not only for material characterization, but also sets up the mechanical loads or boundary conditions for follow-on studies, through calculation of pressures induced over a single cell.

At the cellular-level, Chapter 3 determines the mechanical environment of a single bone cell (osteocyte). Using an idealized geometry for the cell and its surrounding annular fluid space, computational fluid dynamics models are created to elucidate the types and locations of forces that the cell itself is exposed to. The essential goal of these

studies is to answer the question "what do external skeletal forces transform into at the cell level?" Boundary conditions from the previous models were imposed on a single cell to calculate mechanical forces and flow regimes in the pericellular space. The major implications of this study are that mechanical forces are localized at the cell level. Subsequently, cells are likely subspecialized to sense different types of forces along *e.g.* cell processes and the cell body. On a single osteocyte, minimal shear stress is found on the cell body, corresponding to a nearly constant hydrodynamic pressure. In contrast, high gradients of shear stress and pressure are predicted along the cell processes which extend from the body, forming a communication network with other cells.

Following the areas of increased shear stress on the cell process, Chapter 4 investigates sub-cellular geometries and their effects on predicted mechanical forces. For a single process or canaliculus, computational models of physiologic geometry predict a critical variation in shear stress due to complexities in mineralized geometry, where peak stresses are amplified to magnitudes on the order of those noted as necessary to incite cellular responses over baseline in *in vitro* cell studies. Thus, the paradox that has existed in bone between *in vivo* and *in vitro* predictions may be explained through previously neglected spatial incongruities in physiological subcellular geometry that result in amplification of shear stress magnitudes in space and in time. Furthermore, these localized mechanical forces at protrusions of the mineralized bone represent the final transduction of external mechanical forces from the skeletal level to the level of the cell. Of note, transduction at the level of individual receptors to the up- and downregulation of gene activity in the cell nucleus represents the next frontier.

Taking this knowledge of mechanotransduction from previous macro-scale models to the cell itself, the deciphering of mechanical signaling pathways and local fluid environments can be used to improve current laboratory and clinical applications used to understand and exploit the structure-function relationship in bone. Characterization and optimization of *in vitro* cell flow devices are presented in Chapter 5, where performance is measured based on the imparted shear stress to a cell monolayer, with respect to the ideal forces predicted in bone. Commercial chambers are found to impart a range of stresses to cells seeded within the chamber that fall in and out of the desired physiologic state, and thus improvements to existing designs and new designs are addressed. In addition, structures designed to grow bone tissue are evaluated in Chapter 6. The fluid environment of tissue engineering scaffolds is investigated, and tools to optimize the mechanical milieu of such scaffolds are presented to improve functional engineering of bone tissue in the future.

Outlook

The most important aspect of this research is that it extends our understanding of *in vivo* fluid dynamics and mechanotransduction from organ or tissue down to the subcellular level. Due to technological limitations, observations geometries and consequently fluid movement in more remote regions of bone tissue are impossible, and thus the work presented here serves as a best yet prediction of the currently immeasurable. However in lieu of the capability to observe pericellular flow *in vivo*, a number of improvements can still be made in approaches to repair or grow bone, or even to prevent disease. As this work is primarily in healthy tissue, future studies could be carried out to determine

changes in mechanical environments due to diseased or damaged bone. In addition, the cell-scale work presented in this dissertation opens up the possibility for a plethora of future studies on bone cells, including *in vitro* and *in vivo* and *in silico* models, that may further bridge our understanding of the physical and biological aspects of one of nature's most exquisite bioactive materials, *i.e.* bone.

APPENDIX

Appendix A – Chapter 2

Experimental permeability raw data

Falling head - **pre**Chauvenet's - water 1000x piece

delta t (s)	h1 (m)	h2 (m)	L (m)	u (kg/ms)	p (kg/m^3)	g (m/s^2)	k (m^2)
45.03	0.239	0.169	0.159	0.00098	997.4	9.81	
57	0.239	0.169	0.159	0.00098	997.4	9.81	
52.03	0.239	0.169	0.159	0.00098	997.4	9.81	
50	0.239	0.169	0.159	0.00098	997.4	9.81	
48.35	0.239	0.169	0.159	0.00098	997.4	9.81	
50.41	0.239	0.169	0.159	0.00098	997.4	9.81	
48.91	0.239	0.169	0.159	0.00098	997.4	9.81	
48.1	0.239	0.169	0.159	0.00098	997.4	9.81	
49.75	0.239	0.169	0.159	0.00098	997.4	9.81	
49.953333	0.239	0.169	0.159	0.00098	997.4	9.81	1.1049E-10

Std. Dev.= 3.270

Chauvenet's criterion: N=10 xmax/Sx = 1.96

(57-49.95)/ 3.27= 2.154944 =>Throw out 57

Falling head - **post**Chauvenet's - water 1000x piece

delta t (s)	h1 (m)	h2 (m)	L (m)	u (kg/ms)	p (kg/m^3)	g (m/s^2)	k (m^2)
45.03	0.239	0.169	0.159	0.00098	997.4	9.81	
52.03	0.239	0.169	0.159	0.00098	997.4	9.81	
50	0.239	0.169	0.159	0.00098	997.4	9.81	
48.35	0.239	0.169	0.159	0.00098	997.4	9.81	
50.41	0.239	0.169	0.159	0.00098	997.4	9.81	
48.91	0.239	0.169	0.159	0.00098	997.4	9.81	
48.1	0.239	0.169	0.159	0.00098	997.4	9.81	
49.75	0.239	0.169	0.159	0.00098	997.4	9.81	
49.073	0.239	0.169	0.159	0.00098	997.4	9.81	1.1247E-10

Std. Dev. = 2.060

Falling head - **pre**Chauvenet's - silicone 1000x piece

delta t (s)	h1 (m)	h2 (m)	L (m)	u (kg/ms)	p (kg/m^3)	g (m/s^2)	k (m^2)
11220	0.239	0.169	0.159	1	1075	9.81	
11098	0.239	0.169	0.159	1	1075	9.81	
11317	0.239	0.169	0.159	1	1075	9.81	
11225	0.239	0.169	0.159	1	1075	9.81	
11105	0.239	0.169	0.159	1	1075	9.81	
11284	0.239	0.169	0.159	1	1075	9.81	
11301	0.239	0.169	0.159	1	1075	9.81	
11234	0.239	0.169	0.159	1	1075	9.81	
11202	0.239	0.169	0.159	1	1075	9.81	
11220.67	0.207	0.1683	0.159	1	1075	9.81	2.7811E-10

Std. Dev.= 78.035
Chauvenet's criterion:N=10 xmax/Sx = 1.96

Try: (57-49.95333)/3.270 = 1.234485

In the described method, there are inherent uncertainties that arise from the instrumentation chosen. In order to understand the effect in which these uncertainties have on the results, an analysis is performed to determine the uncertainty in measured permeability and the individual contributions to the uncertainty for each parameter. The general solution for uncertainty is

$$\left(\frac{U_k}{k}\right)^2 = \left(\frac{X_1}{k}\frac{\partial k}{\partial X_1}\right)^2\left(\frac{U_{X1}}{X_1}\right)^2 + \left(\frac{X_2}{k}\frac{\partial k}{\partial X_2}\right)^2\left(\frac{U_{X2}}{X_2}\right)^2 + \ldots\ldots + \left(\frac{X_n}{k}\frac{\partial k}{\partial X_n}\right)^2\left(\frac{U_{Xn}}{X_n}\right)^2$$

where permeability k is a function of $X_1, X_2, \ldots, X_n$.

For the Falling Head test, measurements for length, head, and time will introduce uncertainty into the results, as in the previous methods. Here, the head is measured as two separate values, h_1 and h_2, where each introduces an associated uncertainty. The length measurements in this equation (ΔL, A=l*w, h) are found using calipers, where the uncertainty is 0.5 mm for each parameter. The time has an associated uncertainty as well, where Δt is measured with uncertainty of 0.5s for water and 0.01s for silicon oil. The

remaining parameters of viscosity, density, and gravity are assumed to be constant for the given environmental conditions, and thus their uncertainty becomes negligible. The greatest contribution to uncertainty is from the length measurements (via calipers), however since the tolerance is within the desired range, an alternate form of measurement will not be investigated (All uncertainties reported at 95% confidence).

Uncertainty in water samples:

$$\left(\frac{U_k}{k}\right)^2 = \left(\frac{L}{k}\frac{\partial k}{\partial L}\right)^2\left(\frac{U_L}{L}\right)^2 + \left(\frac{\Delta t}{k}\frac{\partial k}{\partial \Delta t}\right)^2\left(\frac{U_{\Delta t}}{\Delta t}\right)^2 + \left(\frac{h1}{k}\frac{\partial k}{\partial h1}\right)^2\left(\frac{U_{h1}}{h1}\right)^2 + \left(\frac{h2}{k}\frac{\partial k}{\partial h2}\right)^2\left(\frac{U_{h2}}{h2}\right)^2$$

replace with measured values and uncertainties

$$\left(\frac{U_k}{k}\right)^2 = \left(\frac{.0005}{.159}\right)^2 + \left(\frac{0.5}{49.07}\right)^2 + \left(\frac{1}{\ln\left(\frac{.239}{.169}\right)}\right)^2\left(\frac{.0005}{.239}\right)^2 + \left(\frac{1}{\ln\left(\frac{.239}{.169}\right)}\right)^2\left(\frac{.0005}{.169}\right)^2$$

$$\left(\frac{U_k}{k}\right) = 1.5\% \qquad U_k = 1.67x10^{-12}\,m^2$$

Uncertainty in silicon oil samples:

$$\left(\frac{U_k}{k}\right)^2 = \left(\frac{L}{k}\frac{\partial k}{\partial L}\right)^2\left(\frac{U_L}{L}\right)^2 + \left(\frac{\Delta t}{k}\frac{\partial k}{\partial \Delta t}\right)^2\left(\frac{U_{\Delta t}}{\Delta t}\right)^2 + \left(\frac{h1}{k}\frac{\partial k}{\partial h1}\right)^2\left(\frac{U_{h1}}{h1}\right)^2 + \left(\frac{h2}{k}\frac{\partial k}{\partial h2}\right)^2\left(\frac{U_{h2}}{h2}\right)^2$$

replace with measured values and uncertainties

$$\left(\frac{U_k}{k}\right)^2 = \left(\frac{.0005}{.159}\right)^2 + \left(\frac{.01}{11221}\right)^2 + \left(\frac{1}{\ln\left(\frac{.239}{.169}\right)}\right)^2\left(\frac{.0005}{.239}\right)^2 + \left(\frac{1}{\ln\left(\frac{.239}{.169}\right)}\right)^2\left(\frac{.0005}{.169}\right)^2$$

$$\left(\frac{U_k}{k}\right) = 1.09\% \qquad U_k = 3.04x10^{-12}\,m^2$$

Appendix B – Chapter 4

Statistical analysis of physiologic image dimensions

In order to gain accurate depictions of the complex subcellular geometry of bone, fluid pathway measurements were taken from high-resolution microscopy images. Slivers of bone tissue were obtained from rat femora of three different subjects, all of which were of similar age, health status, and gender, where each received one of three possible fixing methods. A transmitted electron microscope (TEM) was used to capture two-dimensional images (m = 25) of the bone tissue at various magnifications, where the mineralized bone tissue and cell body are still intact as to accurately capture the fluid space at the subcellular level (Fig. B.1).

Using microscopy imaging software (OpenLab 4.0.3), electronic measurements of the process diameter and fluid-gap height on both sides of the process at the same location were recorded in 0.1 μm intervals where the geometry was visible. In addition, where applicable, the above measurements were also recorded as a function of distance from the cell body as yield possible inferences about variation along the length of the process. In all cases, the parameters were recorded as a function animal number (1-3), fixation method (1-3), and magnification factor (1-5). Since the images used for this study were acquired for previous research investigations, not all images contained relevant structures for this study, and thus measurements were taken from only a sub-section of the total images (n = 16). As a result, incomplete data exists for different combinations of animal, fixation, and magnification, where the resulting data set is listed in table B.1.

Fixation / Animal #	1 – (mpb8)	2 – (mpb7)	3 – (kpb7)
1	-	-	1, 2, 4, 5
2	-	1, 2, 3, 4	-
3	1, 2	-	-

Table B.1: Resulting data set taken from the above combinations of animal, fixation method, and magnification factor. For a specific animal and fixation, the implemented microscope magnification is shown, where 1=15000x, 2=19800x, 3=25200x, 4=32700x, and 5=54300x.

Measurements were taken electronically and exported for statistical analysis using hypothesized linear models with analysis of variance (ANOVA) and regression fit analysis. Specifically, analysis was done to determine if: (1) fluid-gap size varies within bone tissue as a function of animal, fixation, and magnitude; (2) process diameter varies with animal, fixation, and magnitude; (3) fluid-gap size varies with process diameter; and (4) process diameter and fluid-gap size vary as a function of distance from the cell body. A general linear model was used for analysis of variance testing,

$$y_{ijk} = \mu + A_j + B_k + AB_{jk} + \varepsilon_{ijk} \tag{1}$$

where y is the response variable (process diameter or gap size), μ is the sample mean, A and B are factors for any two of the possible factors (animal, fixation, magnification), ε is standard error, i=1,..,242 is measurement index, j and k are indices that match the factor levels. However, since the resulting data set is incomplete in table B.1, not all combinations could be taken into account in a 2-way ANOVA test. Thus, in certain cases inferences on the influence of a specific factor were based on only one factor, and thus (1) is simplified for 1-way ANOVA testing. As seen from the table, only when the response variable is a function of animal and magnification (excluding fixation factor) can a 2-way ANOVA be carried out, and then only with two of the five magnification levels. Thus, in order to test the effect of animal and fixation on the response variable using 1-way ANOVA, we must assume that the interaction between these two factors is

negligible, which may be reasonable based on biological considerations. In this case, hypotheses are tested to determine the influence of the proposed factor in a 1-way ANOVA, where

Null hypothesis, H_0: $A_j = 0$ vs. Alternate, H_a: $A_j \neq 0$

In addition to the significance testing using analysis of variance, a regression analysis was also carried out in certain cases to determine possible patterns in the response variables, where the general model is

$$y_{ijk} = \beta_0 + \beta_1 x_1 + \varepsilon_{ijk} \tag{2}$$

where y is the response variable (process diameter or gap size), β_0 is regression constant, β_1 is the regression coefficient for the applied factor (distance from cell body), and x_1 is the predictor variable. Specifically, regression was used to determine if process diameter and gap size varied with distance from the cell body. In this case, measurements were only able to be taken from two images where magnification factor was held constant.

Overall mean gap-size and process diameter

Based on the sampling data for fluid-gap size and cell process diameter, overall both dimensions were found to vary with large standard deviation, for a constant magnification (discussed below). The overall mean fluid-gap size is found to be 0.131 μm with 0.056 standard deviation, where the overall mean cell-process diameter is 0.0991 μm and 0.0289 standard deviation. Removing any outliers, a two-sample t-test of the means yields that the overall gap-size and process-diameter are significantly different, although on the same order of magnitude, and thus need to be measured independently

(Fig. B.1). The data for gap-size and process diameter are reasonably normal and the residuals are found to be independent.

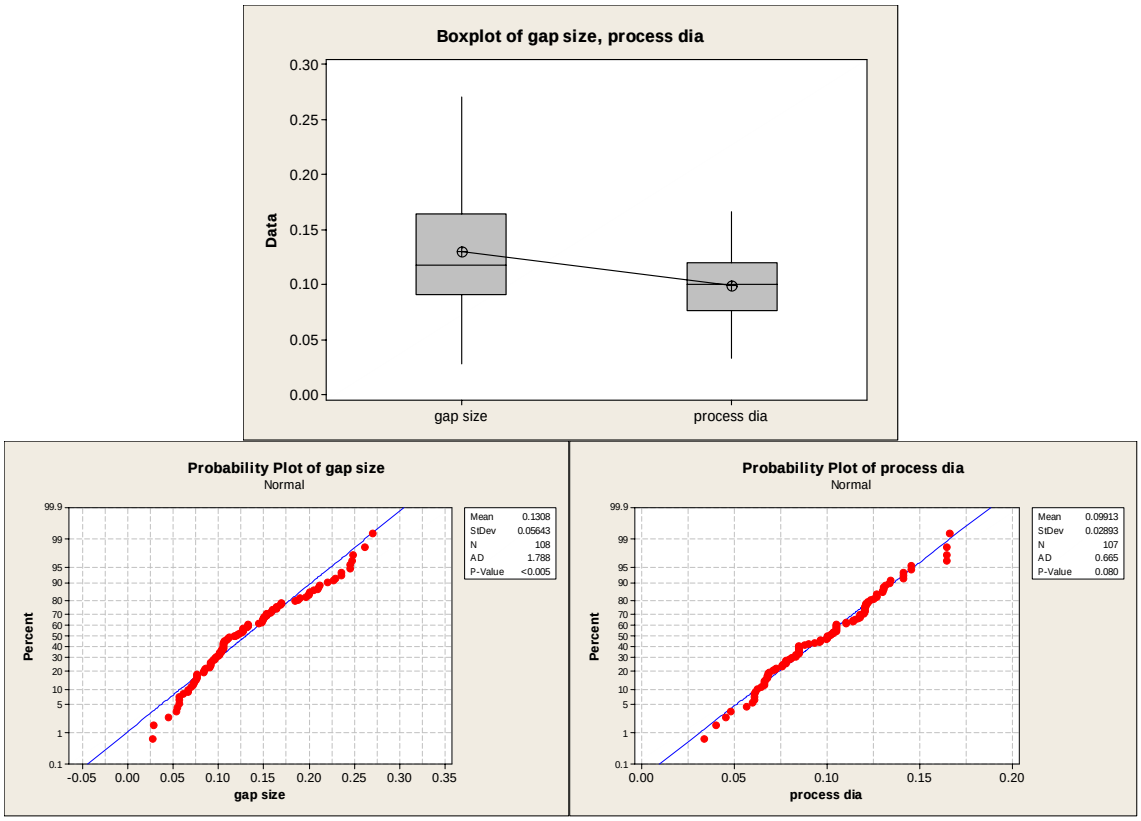

Fig. B.1: (top) boxplot - mean and standard deviation for overall fluid-gap size and process diameter are found to be significantly differenct; (bottom) normality plots of gap size and process diameter.

Effect of animal and fixation on gap-size

In order to evaluate the effects of animal, fixation method, and magnification factor on the measured response variables, analysis of variance was carried out for all cases. To begin, the influence of these factors on fluid-gap size was investigated. When the magnification is held constant, thus removing its effect, the influence of specific animal (n=3) was found (due to incomplete data, fixation method cannot be constant, although the negligence is deemed acceptable as found below). Removing any outliers, 1-way ANOVA provides the mean gap-sizes as a function of animal (Fig. B.2). According to the ANOVA test, the animal isn't found to significantly effect the gap-size

measurement (p-value = 0.492), and thus the null hypothesis proposed above is accepted. Hence, in the following observations and analysis, the animal number does not need to be held constant. Although fixation was not held constant, the animal didn't cause significant variance in measured gap-size regardless, and thus our assumptions are upheld. Similarly, normal and independence assumptions are also satisfied, where normality and residual plots show no noticeable variation or pattern. Since gap size was not found to vary even when fixation could not be held constant due to incomplete data, analysis on the effect of fixation on gap size does not need to be completed as it would yield the same results. Thus, the below results (Fig. B.2), show that neither animal nor fixation method significantly affect the measured gap-size.

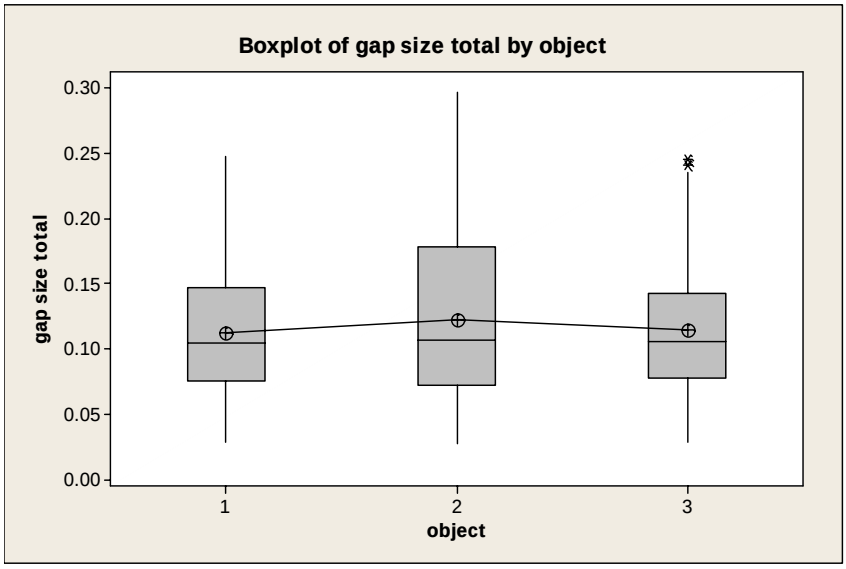

Source	DF	SS	MS	F	P-value
Animal	2	0.00436	0.00218	0.71	0.492
Error	232	0.71168	0.00307		
Total	234	0.71604			

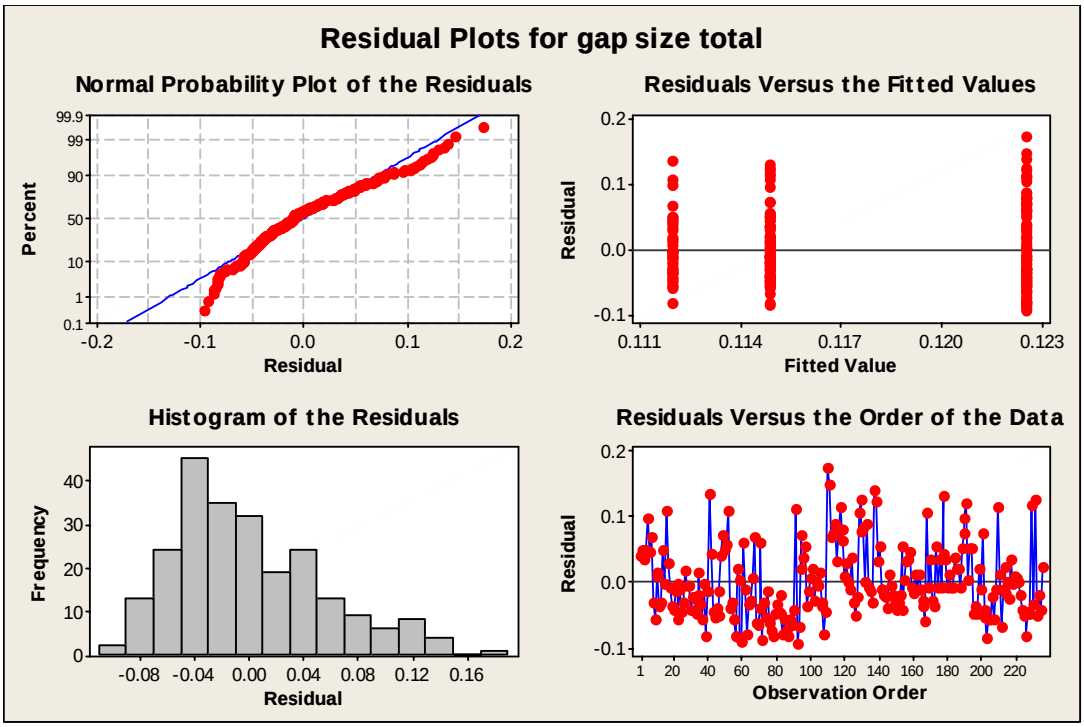

Fig. B.2: (top) box plots of gap size; (bottom) normality plot, residuals show independence and normal data; ANOVA table, animal doesn't significantly effect total gap size.

Effect of magnification on gap-size

Since animal and fixation variation were found to have no effect on gap-size measurement, the influence of magnification can be investigated without holding these factors constant. Thus, a 1-way analysis of variance for gap size as a function of magnification is calculated, where a significant difference in gap-size measurement is found, hence the null hypothesis is rejected. Comparing the confidence intervals for each magnification group, it is found that the measured gap-size differs significantly between groups 1 and 2 only (Fig. B.3). Again, assumptions on normality and independence are satisfied as seen from residual plots of the data.

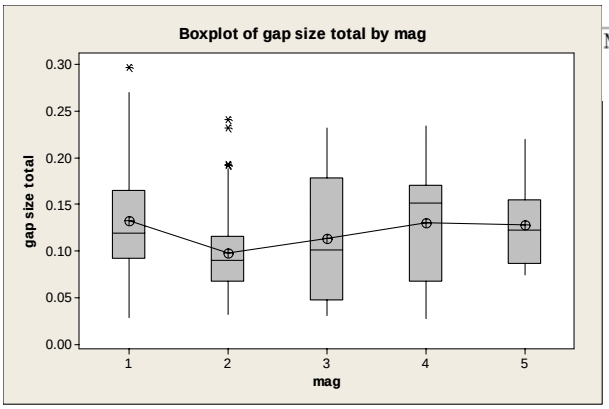

Source	DF	SS	MS	F	P-value
Magnification	4	0.0639	0.01597	5.63	<0.0001
Error	230	0.65214	0.00284		
Total	234	0.71604			

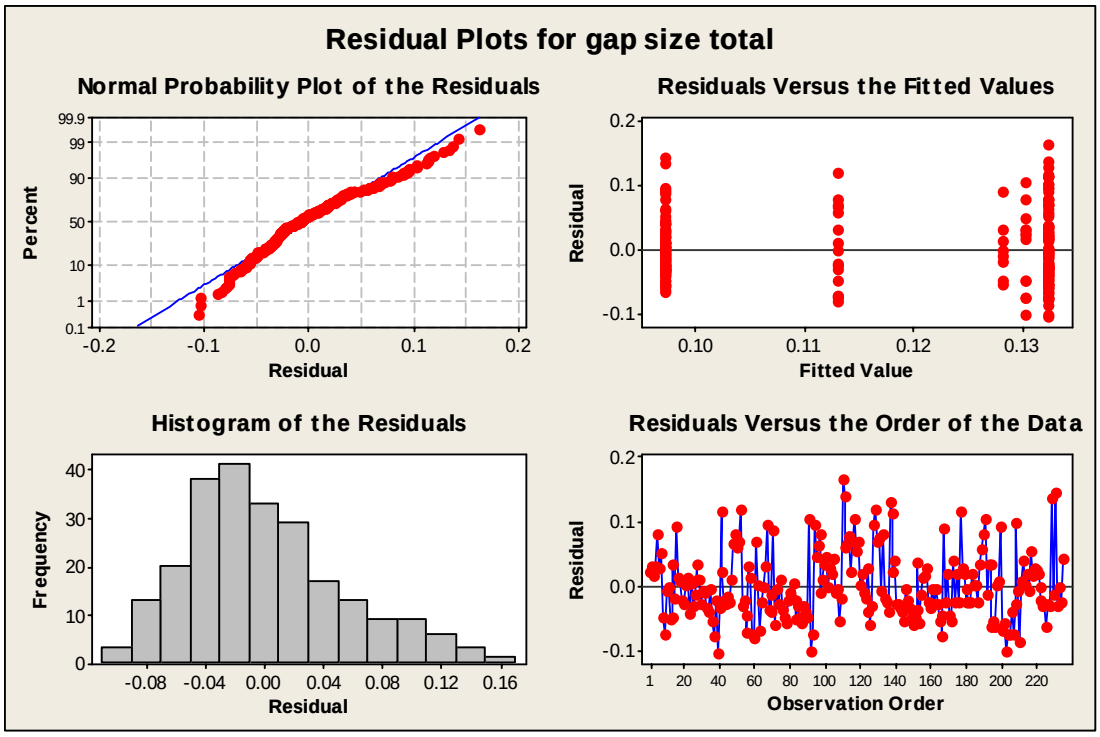

Fig. B.3: (top-left) box plot of gap size with significance between groups 1 and 2; (top-right) normal and residual plots show independence and normality of data; (lower-right) ANOVA table, magnification shows significant effect on gap.

Effect of animal and fixation on process diameter

Due to the possible influence of magnification on the measured response variables and an incomplete data set for all possible combinations, the process diameter is measured as a function of animal and fixation, where magnification is held constant. Using 1-way ANOVA for both animal and fixation factors, it is found that neither animal nor fixation has a significant effect on measure process-diameter (Fig. B.4). Since there

is no influence of these factors, results for the mean and standard deviation of process diameter are found to be the identical. Here, boxplots show very similar mean and standard deviation between the groups, where the normality assumption is upheld. However, it is noted that the variance seems to increase as with group 1-3, bringing questionability into the residual plots. However, since the data set is not balanced, a misrepresentation could exist. Regardless, the residuals appear to satisfy independence at least for this pilot study.

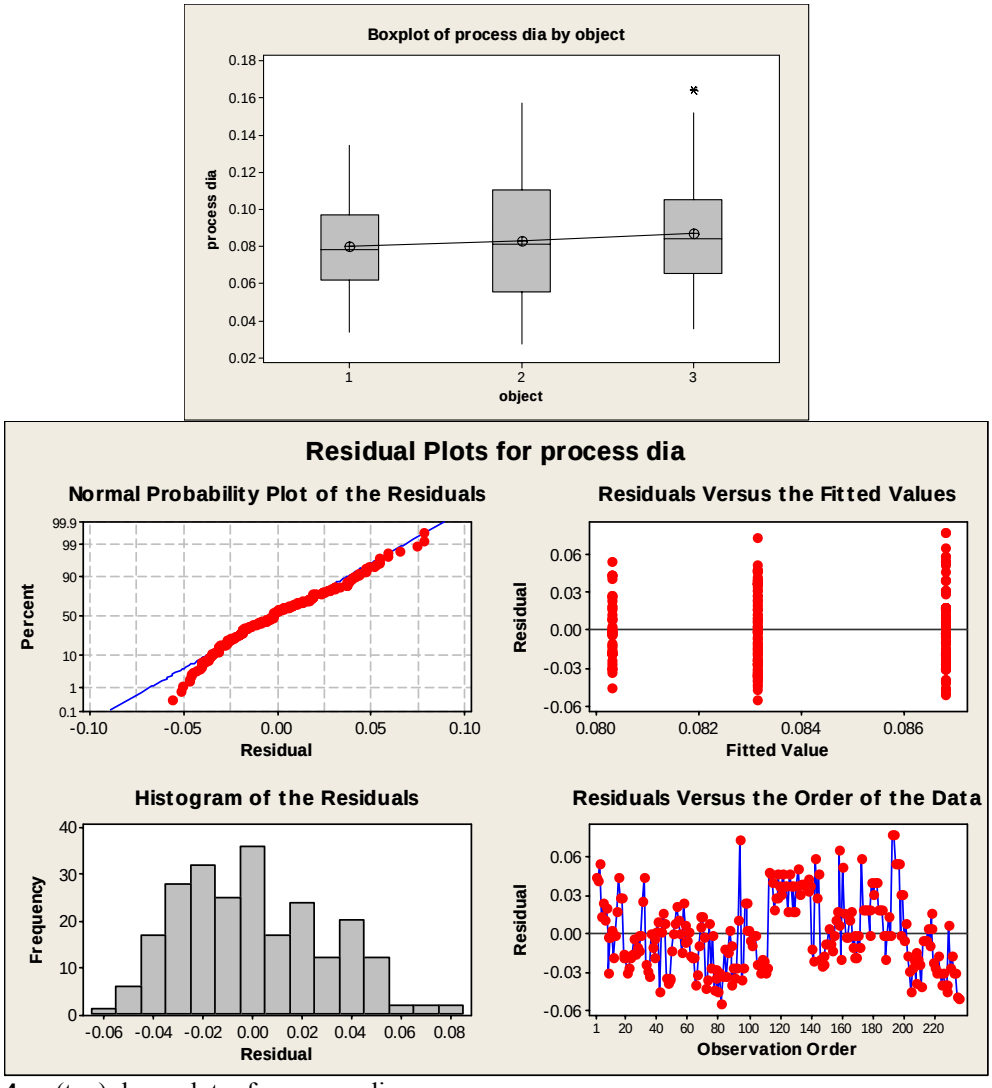

Fig. B.4: (top) box plot of process dia. vs. animal (fixation); (bottom) normal and residual plots of data; (right) ANOVA table, animal (fixation) do not affect process diameter.

Source	DF	SS	MS	F	P-value
Factor	2	0.001439	0.00072	0.86	0.425
Error	233	0.195423	0.000834		
Total	235	0.196863			

Effect of magnification on process diameter

As before, since animal and fixation are not to found to influence the measured response variable, the effect of magnification can be investigated without holding these factors constant. Using 1-way ANOVA calculations for the proposed single-factor linear model, process diameter is found to significantly vary as a function of magnification (Fig. B.5). Specifically, significance is found between magnification groups 1-2, 1-3, 2-4, and 2-5. Again, the lower-magnification groups are found to significantly affect the measured response variable, as seen in the gap-size determination.

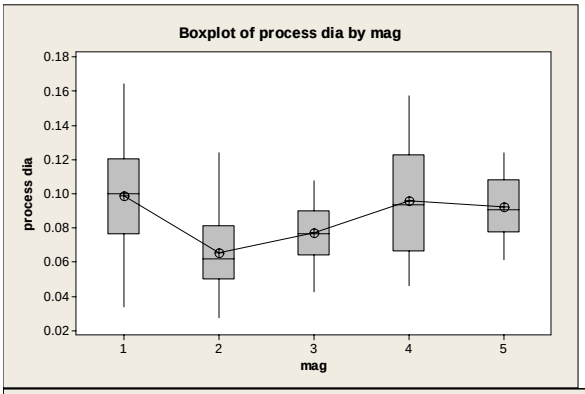

Source	DF	SS	MS	F	P-value
Magnification	4	0.057388	0.014347	23.76	<0.001
Error	231	0.139475	0.000604		
Total	235	0.196863			

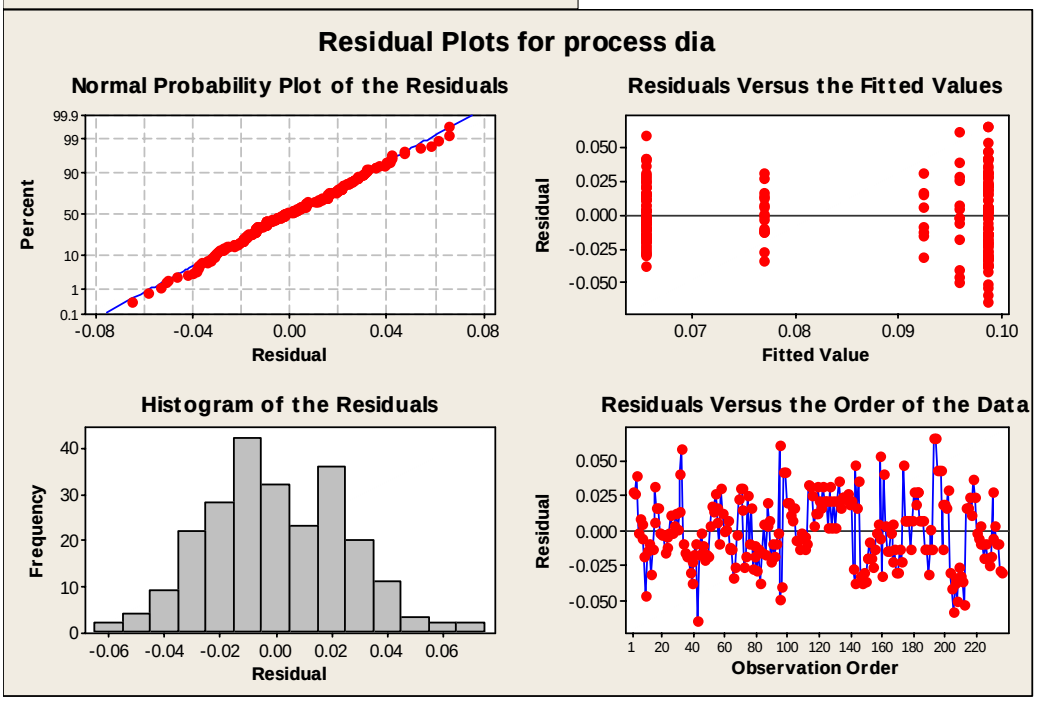

Fig. B.5: (top) boxplots of process diameter vs. magnification significance with groups 1-2; (bottom) normality and residual plots; (top-right) ANOVA table, magnification significantly affects process dia.

Relationship between gap-size and process diameter

In order to determine how fluid gap-size relates to cell-process diameter, the response variables are plotted for a constant magnification, as dictated by the ANOVA tests in previous sections. Using regression analysis, in general gap-size is found to increase with increasing process diameter (Fig. B.6). However, the proposed linear regression model does not yield a strong relationship, where R^2 is found to be 39%. Using a t-test on the predictor (process diameter), a significant relationship between gap-size and process diameter is found (P-value<0.001). Furthermore, analysis of variance of the regression model shows that the model itself is significant (P-value<0.001), thus supporting the predictor-response relationship. Specifically, gap-size increases with roughly 1.3x the process diameter, which correlates closely to values reported in the literature (1.5x process diameter). Residual plots show that normality is satisfied, however the variance appears to increase with gap-size, yet for a pilot study, it is assumed that independence is satisfied.

Regression equation:

Gap-size = 0.0111 + 1.29*(process-diameter)

Predictor	Coef	SE Coef	T	P-value
Constant	0.01112	0.01155	0.96	0.339
Process dia.	1.2942	0.1737	7.45	<0.001
S = 0.0289	R^2 = 39.5%	R^2_{adj} = 38.8%		

Source	DF	SS	MS	F	P-value
Regression	1	0.0466	0.0466	55.52	<0.001
Residual Err	85	0.0714	0.0008		
Total	86	0.1180			

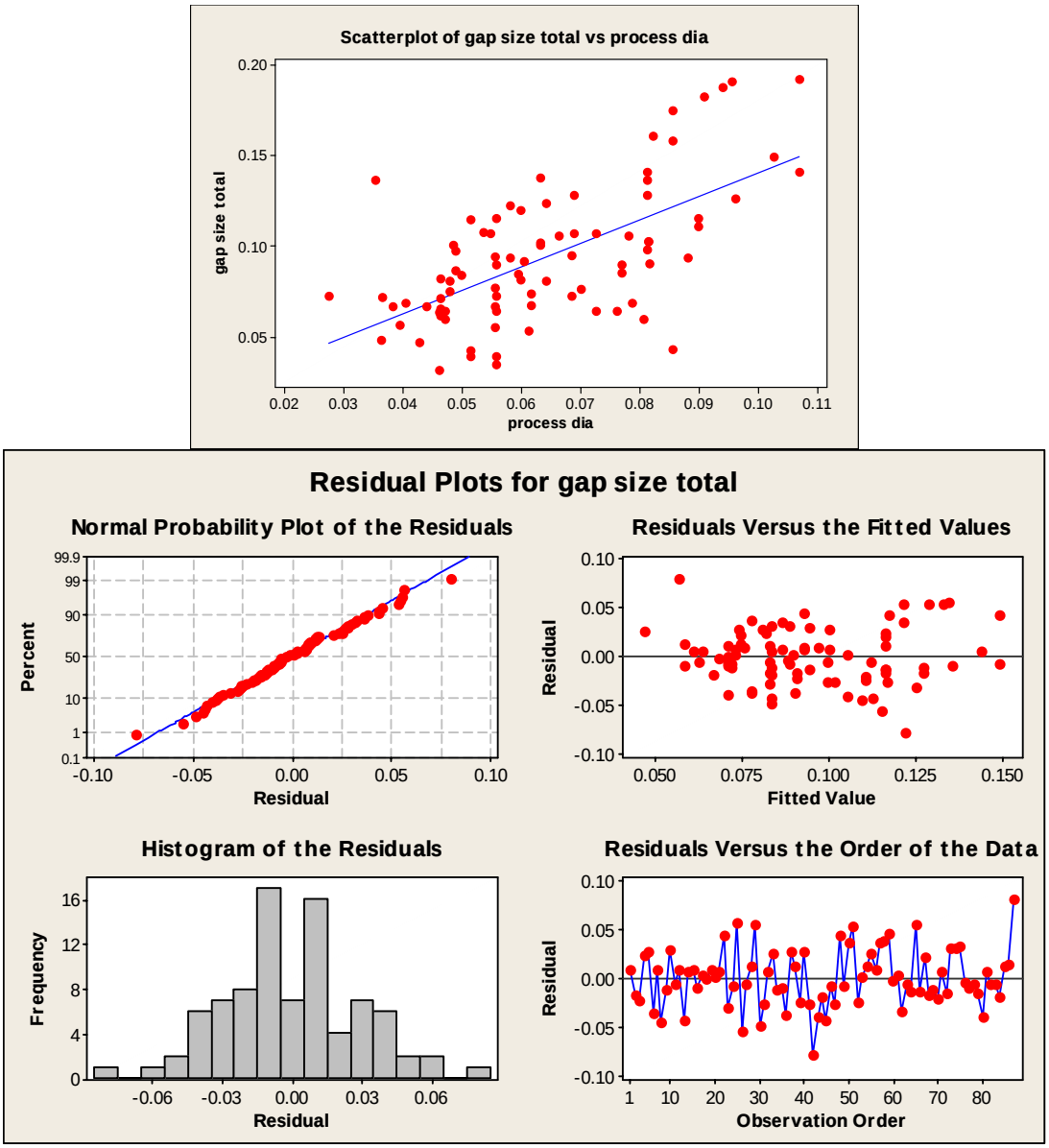

Fig. B.6: (top) gap-size, process scatterplot with linear regression; (bottom) normal and residual plots of data; (top) regression analysis, significant process relationship, low-R^2 value; (top) ANOVA table, regression model is significant.

Process diameter and gap-size as function of distance from cell-body

In order to determine how the process diameter and gap-size vary with distance from the cell body, regression analysis from two data sets (images) is used to calculate a general linear model. For a constant magnification, the process diameter is found to decrease with increasing distance from the cell body (Fig. B.7). The regression is assumed to be strong as R^2 is 78% (with no change in adjusted R^2). Using a t-test, the distance from

the cell body is found to be significant to the change in process diameter. Furthermore, using ANOVA on the regression model itself, the regression is found to be significant (P-value<0.001). The diameter decreases with 0.0164x the distance from the cell body, which is similar to values reported in the literature.

Regression equation:

Process diameter = 0.093 – 0.0164*(distance from cell body)

Predictor	Coef	SE Coef	T	P-value
Constant	0.09299	0.0034	27.34	<0.001
Dist from cell	-0.0164	0.0016	-9.96	<0.001
S = 0.008388	R2 = 78.6%	R2adj = 77.8%		

Source	DF	SS	MS	F	P-value
Regression	1	0.00698	0.00698	99.14	<0.001
Res. Error	27	0.00189	0.00007		
Total	28	0.00888			

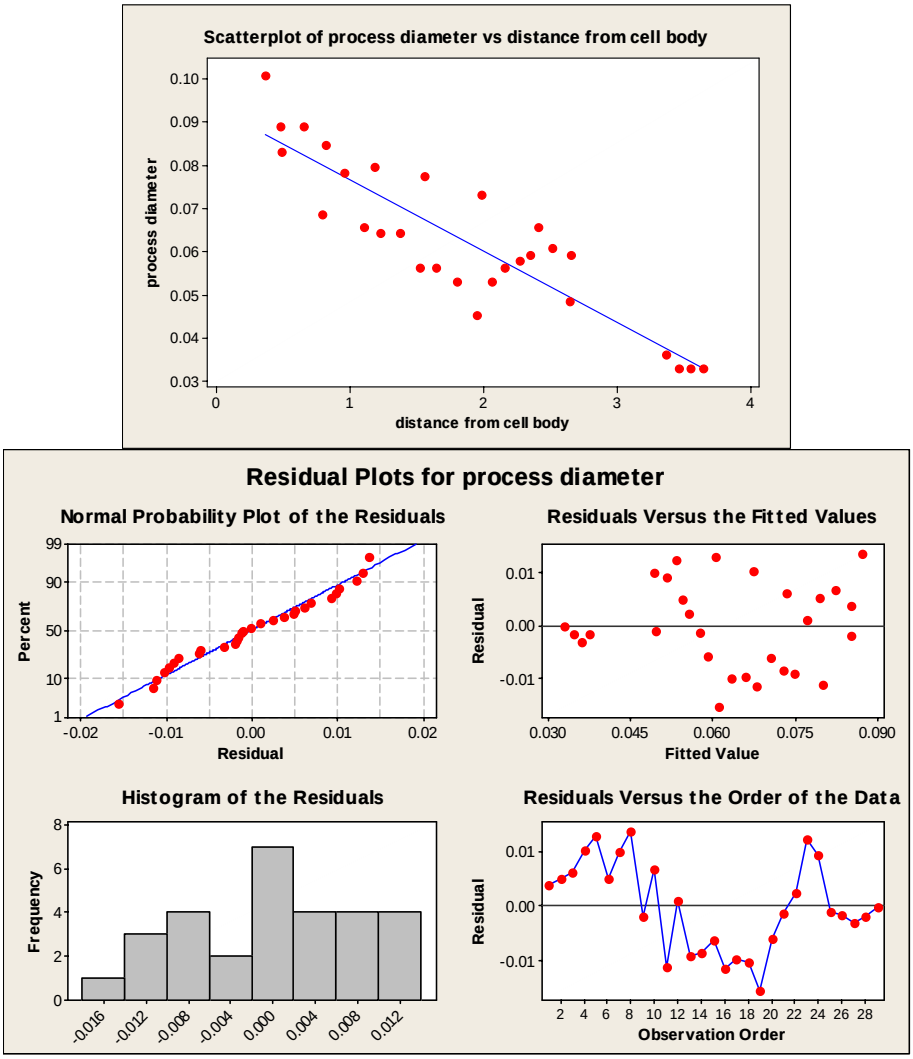

Fig. B.7: (top) process diameter vs distance from cell body, regression; (bottom) normal and residual plots; (top-left) regression analysis, t-test, distance from cell is significant; (top-right) ANOVA table for regression model, significance is found.

Similarly to the relationship between process diameter and distance from the cell body, the fluid gap-size is found to decrease with increasing distance from the cell body (Fig. B.8). This further supports the relationship between process diameter and gap-size as noted in previous sections. The gap-size decreases with 0.154 plus 0.0428x the distance from the cell body, where R^2 = 54% is not quite as strong as for the process diameter. The distance is found to significantly affect the gap-size using a t-test, and performing an ANOVA for the regression model, yields that the model itself is significant (P-value<0.001). Thus, the predicted general relationship is assumed to be accurate. The residuals show that normality is satisfied; yet again the variance tends to increase with increase in distance from the cell body. However, independence is assumed to be satisfied for this pilot study.

Regression equation:

Gap size = 0.154 – 0.0429*(distance from cell body)

Predictor	Coef	SE Coef	T	P-value	Source	DF	SS	MS	F	P-value
Constant	0.15389	0.01884	8.17	<0.001	Regression	1	0.03171	0.03171	26.05	<0.001
Dist from cell	-0.0429	0.00841	-5.10	<0.001	Res. Error	22	0.02678	0.00122		
S = 0.034889	R^2 = 54.2%	R^2_{adj} = 52.1%			Total	23	0.05848			

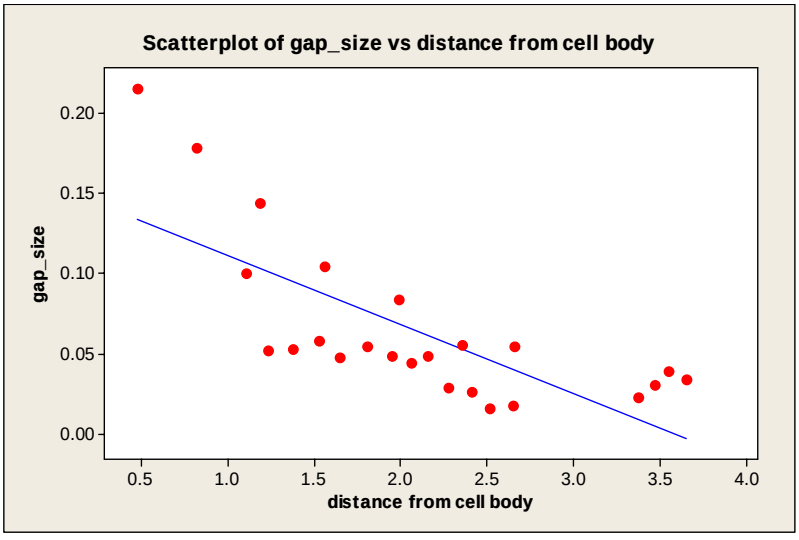

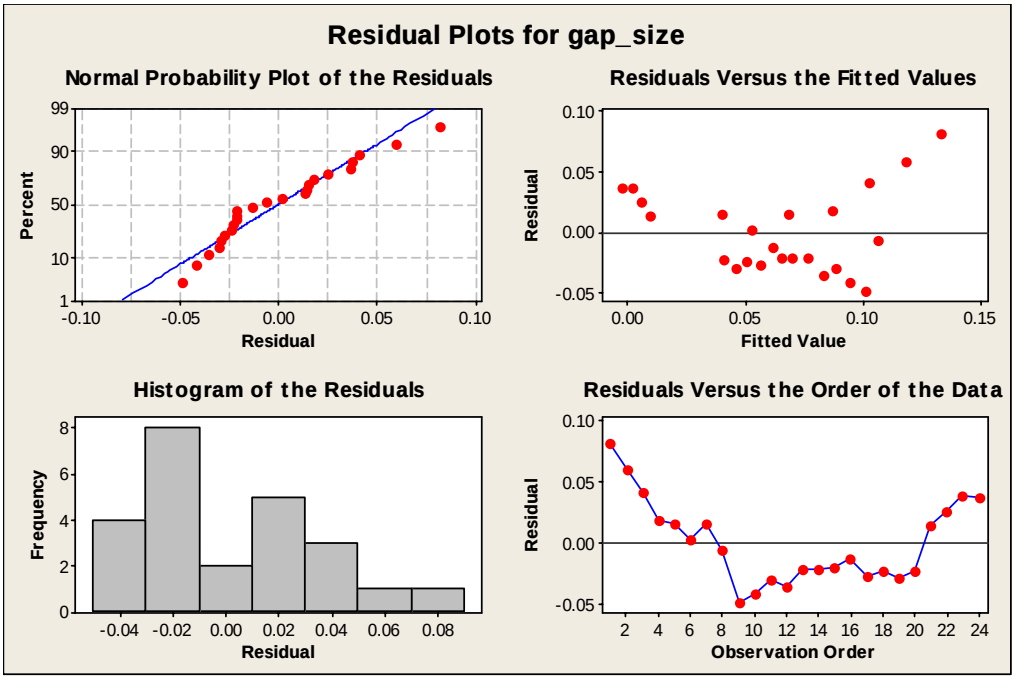

Fig. B.8: (top) gap-size vs distance from cell body, regression; (bottom) normal and residual plots; (top-let) regression analysis, t-test, distance from cell is significant; (top-right) ANOVA table for regression model, significance is found.

BIBLIOGRAPHY

Aarden EM, Burger EH, Nijweide PJ, 1994. Function of osteocytes in bone. J Cell Biochem 55:287-299.

Aarden EM, Wassenaar AM, Alblas MJ, Nijweide PJ, 1996. Immunocytochemical demonstration of extracellular matrix proteins in isolated. osteocytes. Histochem Cell Biol 106:495-501.

Adachi T, Osako Y, Tanaka M, Hojo M, Hollister SJ, 2006. Framework for optimal design of porous scaffold microstructure by computational simulation of bone regeneration. Biomaterials 27:3964.

Ajubi NE, Klein-Nulend J, Alblas MJ, Burger EH, Nijweide PJ, 1999. Signal transduction pathways involved in fluid flow-induced PGE2 production by cultured osteocytes. Am J Physiol 276:E171-E178.

Albuquerque ML, Flozak AS, 2003. Lamellipodial motility in wounded endothelial cells exposed to physiologic flow is associated with different patterns of beta1-integrin and vinculin localization. J Cell Physiol 195:50-60.

Alexopoulos LG, Setton LA, Guilak F, 2005. The biomechanical role of the chondrocyte pericellular matrix in articular cartilage. Acta Biomater 1:317-325.

Allen FD, Hung CT, Pollack SR, Brighton CT, 2000. Serum modulates the intracellular calcium response of primary cultured bone cells to shear flow. J Biomech 33:1585-1591.

Almekinders LC, Banes AJ, Ballenger CA, 1993. Effects of repetitive motion on human fibroblasts. Med Sci Sports Exerc 25:603-7.

Anderson EJ, Knothe Tate ML, 2004. Performance evaluation of three cell flow chambers: How well is stress controlled at the cellular level? Euro Soc Biom 353.

Anderson EJ, Knothe Tate ML, 2004. Measuring permeability of bone in the lacunocanalicular network via scaled physical models. Transactions of BMES.

Anderson EJ, Knothe Tate ML, 2004. Performance evaluation of four cell flow chambers: How well is stress controlled at the cellular level? ASME IMECE 2004:61432.

Anderson EJ, Knothe Tate ML, 2005. Lacunocanalicular permeability measurements in healthy and osteoporotic patients: An experimental fluid mechanics approach using scaled physical models. Trans ORS 2005, 1126.

Anderson EJ, Kaliyamoorthy S, Alexander JID, Knothe Tate ML, 2005. Nano-micro scale models of periosteocytic flow show differences in stresses imparted to cell body and processes. Ann Biomed Eng 33:52-62.

Anderson EJ, Jackowe DJ, Cooke MN, Savrin JS, Mistry A, Shi X, Rimnac C, Mikos AG, Knothe Tate ML, Dean D, 2005. Permeability and porosity of in vitro degraded, stereolithographically-rendered solid/porous composite poly(propylene fumarate) tissue engineering scaffolds. Abstract presented at the Midwest Tissue Engineering Conference.

Anderson EJ, Savrin J, Cooke M, Dean D, Knothe Tate ML, 2005. Performance evaluation of tissue engineering scaffolds – development of a novel tool for optimization of fluid flow & permeability.

Abstract presented at the ASME Summer Bioengineering Conference, Vail, CO. Abstract no. 0410280.

Anderson EJ, Savrin J, Cooke M, Dean D, Knothe Tate ML, 2005. Evaluation of and optimization of tissue engineering scaffolds using computational fluid dynamics. Abstract presented at the Annual Meeting of the Biomedical Engineering Society, Baltimore, MD. Abstract no. 143471.

Anderson EJ, Savrin J, Cooke M, Dean D, Knothe Tate ML, 2006. Optimization of tissue engineering scaffold architectures and flow regimes for cell cultivation. Abstract presented at the Annual Meeting of the Orthopaedic Research Society, Chicago, IL.

Anderson EJ, Falls TD, Sorkin AM, Knothe Tate ML, 2006. The imperative for controlled mechanical stresses in unraveling cellular mechanisms of mechanotransduction. Biomed Eng Online 5:27.

Anderson JC, Eriksson C, 1968. Electrical properties of wet collagen. Nature 218:166-168.

Archambault JM, Elfervig-Wall MK, Tsuzaki M, Herzog W, Banes AJ, 2002. Rabbit tendon cells produce MMP-3 in response to fluid flow without significant calcium transients. J Biomech 35:303-309.

Astarita G, 1997. Dimensional analysis, scaling, and orders of magnitude. Chem Eng Sci 52:4681-4698.

Bakker DP, van der Plaats A, Verkerke GJ, Busscher HJ, van der Mei HC, 2003. Comparison of velocity profiles for different flow chamber designs used in studies of microbial adhesion to surfaces. Appl Environ Microbiol 69: 6280-7.

Bassett CA, 1965. Electrical effects in bone. Scientific American 213:18-25.

Baud CA, 1968. Submicroscopic structure and functional aspects of the osteocyte. Clin Orthop 56:227-36.:227-236.

Berthiaume F, Aparicio CL, Eungdamrong J, Yarmush ML, 1999. Age- and disease-related decline in immune function: an opportunity for "thymus-boosting" therapies. Tissue Eng 5:499-514.

Bhagyalakshmi A, Berthiaume F, Reich M, Frangos JA, 1992. Fluid shear stress stimulates membrane phospholipid metabolism in cultured human endothelial cells. J Vasc Res 29:443-449.

Bilek AM, Dee KC, Gaver DP III, 2003. Mechanisms of surface-tension-induced epithelial cell damage in a model of pulmonary airway reopening. J Appl Physiol 94:770-783.

Biot MA, 1941. General theory of three-dimensional consolidation. J Applied Physics 12:155-164.

Birukov KG, Birukova AA, Dudek SM, Verin AD, Crow MT, Zhan X, DePaola N, Garcia JG, 2002. Shear stress-mediated cytoskeletal remodeling and cortactin translocation in pulmonary endothelial cells. Am J Respir Cell Mol Biol 26:453-464.

Boschetti F, Raimondi MT, Migliavacca F, Dubini G, 2006. Prediction of the micro-fluid dynamic environment imposed to three-dimensional engineered cell systems in bioreactors. J Biomech 39:418.

Botchwey EA, Pollack SR, Levine EM, Johnston ED, Laurencin CT, 2004. Quantitative analysis of three-dimensional fluid flow in rotating bioreactors for tissue engineering. J Biomed Mater Res A 69:205.

Bridgman P, 1922. Dimensional Analysis. Yale University Press, New Haven.

Brown DC, Larson RS, 2001. Improvements to parallel plate flow chambers to reduce reagent and cellular requirements. BMC Immunol 2:9.

Burger EH, Veldhuijzen JP, 1993. Influence of mechanical factors on bone formation, resorption and growth in vitro. In: Hall BK (ed.) Bone, vol. 7. CRC Press, Boca Raton, FL, USA, pp. 37-56.

Burger EH, Klein-Nulend J, Smit TH, 2003. Strain-derived canalicular fluid flow regulates osteoclast activity in a remodelling osteon-a proposal. J Biomech 36:1453-1459.

Busscher HJ, van der Mei HC, 1995. Use of flow chamber devices and image analysis methods to study microbial adhesion. Methods Enzymol 253:455-77.

Butler DL, Goldstein, S.A., Guilak, F. Functional tissue engineering: the role of biomechanics. J Biomech Eng 122, 570, 1993.

Butler PJ, Norwich G, Weinbaum S, Chien S, 2001. Shear stress induces a time- and position-dependent increase in endothelial cell membrane fluidity. Am J Physiol Cell Physiol 280:C962-C969.

Cheng JT, Giordano N, 2002. Fluid flow through nanometer-scale channels. Phys Rev 65:31206.

Chin WC, 2001. Computational Rheology for Pipeline and Annular Flow. Woburn: Gulf Professional Publishing, pp. 1-257.

Chua CK, Leong KF, Cheah CM, Chua SW, 2003. Development of a tissue engineering scaffold structure library for rapid prototyping. Part 2: Parametric library and assembly program. Int J Adv Manuf Technol 21:302.

Chotard-Ghodsnia R, Drochon A, Grebe R: A new flow chamber for the study of shear stress and transmural pressure upon cells adhering to a porous biomaterial. J Biomech Eng 2002, 124:258-261.

Cinamon G, Alon R, 2003. A real time in vitro assay for studying leukocyte transendothelial migration under physiological flow conditions. J Immunol Methods 27:53-62.

Cioffi M, Boschetti F, Raimondi MT, Dubini G, 2006. Modeling evaluation of the fluid-dynamic microenvironment in tissue-engineered constructs: a micro-CT based model. Biotechnol Bioeng 93:500.

Cooke MN, 2004. Novel stereolithographic manufacture of biodegradable bone tissue scaffolds. Dissertation Abstracts International 0548, Ann Arbor, MI.

Cooper RR, Milgram JW, Robinson RA, 1966. Morphology of the osteon. An electron microscopic study. J Bone Joing Surg Am 48:1239-1271.

Cowin SC, Weinbaum S, Zeng Y, 1995. A case for bone canaliculi as an anatomical site of strain generated potentials. J Biomech 28:1281-1297.

Cowin SC, 1999. Bone poroelasticity. J Biomech 32:217-238.

Crick F, 1970. Diffusion in embryogenesis. Nature 5231:420-422.

Donahue SW, Donahue HJ, Jacobs CR, 2003. Osteoblastic cells have refractory periods for fluid-flow-induced intracellular calcium oscillations for short bouts of flow and display multiple low-magnitude oscillations during long-term flow. J Biomech 36:35-43.

Dudley HR, Spiro D, 1961. The Fine Structure of Bone Cells. J Biophys Biochem Cyto 11:627-649.

Einstein A, 1911. Elementare betrachtungen ueber die termische molecular bewegungen in festen korpern. Ann Phys 35:679-694.

Essig M, Friedlander G, 2003. Shear-stress-responsive signal transduction mechanisms in renal proximal tubule cells. Curr Opin Nephrol Hypertens 12:31-34.

Ferraro JT, Daneshmand M, Bizios R, Rizzo V, 2004. Depletion of plasma membrane cholesterol dampens hydrostatic pressure and shear stress-induced mechanotransduction pathways in osteoblast cultures. Am J Physiol Cell Physiol 286:C831-C839.

Fleury ME, Boardman KC, Swartz MA, 2006. Autologous morphogen gradients by subtle interstitial flow and matrix interactions. Biophys J 91:113-121.

Forlow SB, McEver RP, Nollert MU, 2000. Leukocyte-leukocyte interactions mediated by platelet microparticles under flow. Blood 95:1317-1323.

Frangos JA, McIntire LV, Eskin SG, 1988. Shear stress induced stimulation of mammalian cell metabolism. Biotech Bioeng 32:1053-1060.

Fritton SP, McLeod KJ, Rubin CT, 2000. Quantifying the strain history of bone: spatial uniformity and self-similarity of low-magnitude strains. J Biomech 33:317-25.

Fukushima S, Natatsu A, Kaibara M, Oka K, Tanishita K, 2001. Measurement of surface topography of endothelial cell and wall shear stress distribution on the cell. JSME 44(c):972-981.

Funyu J, Mochida S, Inao M, Matsui A, Fujiwara K, 2001. VEGF can act as vascular permeability factor in the hepatic sinusoids through upregulation of porosity of endothelial cells. Biochem Biophys Res Commun 280:481-485.

Gaver DP, Kute SM, 1998. A theoretical model study of the influence of fluid stresses on a cell adhering to a microchannel wall. Biophys J 75:721-733.

Gibson LJ, Ashby MF, 1997. Cellular solids: structure and properties. 2nd ed., Cambridge Univ Press, New York.

Goldstein AS, DiMilla PA, 2002. Effect of adsorbed fibronectin concentration on cell adhesion and deformation under shear on hydrophobic surfaces. J Biomed Mater Res 59:665-675.

Griffith LG, Naughton G, 2001. Biomaterials and scaffolds for tissue engineering: Emerging design principles. Ann NY Acad Sci, Proc BECON Conference on Reparative Medicine, 961, 83-95.

Guilak F, Ratcliffe A, Mow VC, 1995. Chondrocyte deformation and local tissue strain in articular cartilage: a confocal microscopy study. J Orthop Res 13:410-21.

Guo P, Weinstein AM, Weinbaum S, 2000. A hydrodynamic mechanosensory hypothesis for brush border microvilli. Am J Physiol Renal Physiol 279:F698-F712.

Han Y, Cowin SC, Schaffler MB, Weinbaum S, 2004. Mechanotransduction and strain amplification in osteocyte cell processes. Proc Natl Acad Sci 101:16689-94.

Harrigan TP, Hamilton JJ, 1993. Bone strain sensation via transmembrane potential changes in surface osteoblasts: Loading rate and microstructural implications. J Biomech 26:183-200.

Hildebrand G, Kunze S, Driver M, 2001. Blood cell adhesion on sensor materials studied by light, scanning electron, and atomic-force microscopy. Ann Biomed Eng 29:1100-1105.

Hollister SJ, Maddox RD, Taboas JM, 2002. Optimal design and fabrication of scaffolds to mimic tissue properties and satisfy biological constraints. Biomaterials 23:4095.

Hollister SJ, 2005. Porous scaffold design for tissue engineering. Nat Mater 4:518.

Howk D, Chu TM, 2006. Design variables for mechanical properties of bone tissue scaffolds. Biomed Sci Instrum 42:278.

Hung CT, Pollack SR, Reilly TM, Brighton CT, 1995. Real-time calcium response of cultured bone cells to fluid flow. Clin Orthop 313:256-269.

Hung CT, Allen FD, Pollack SR, Brighton CT, 1996. Intracellular Ca^{2+} stores and extracellular Ca^{2+} are required in real-time Ca^{2+} response of bone cells experiencing fluid flow. J Biomech 29:1411-1417.

Hutmacher DW, 2000. Mechanical properties and cell cultural response of polycaprolactone scaffolds designed and fabricated via fused deposition modeling. J Biomed Mater Res 55, 203.

Hutmacher DW, 2001. Scaffold design and fabrication technologies for engineering tissues-state of the art and future perspectives. J Biomater Scie Polym Edn 12, 107.

Jacobs CR, Yellowley CE, Davis BR, Zhou Z, Cimbala JM, Donahue HJ, 1998. Differential effect of steady versus oscillating flow on bone cells. J Biomech 31:969-976.

Johnson DL, McAllister TN, Frangos JA, 1996. Fluid flow stimulates rapid and continuous release of nitric oxide in osteoblasts. Am Physiol Soc 205-208.

Johnson MW, Chakkalakal DA, Harper RA, Katz JL, 1980. Comparison of the electromechanical effects in wet and dry bone. J Biomech 13:437-442.

Johnson MW, Chakkalakal DA, Harper RA, Katz JL, Rouhana SW, 1982. Fluid flow in bone in vitro. J Biomech 15:881-885.

Johnson MW, 1984. Behavior of Fluid in Stressed Bone and Cellular Stimulation. Calcif Tissue Int 36:72-76.

Johnson MW, Katz JL, 1984. Some new developments in the rheology of bone. Biorheology 1:169-174.

Junqueira LC, Carneiro J, Kelley RO, 1995. "Bone, In Basic Histology." Upper Saddle River, NJ: Prentice-Hall, pp. 132-151.

Kamm RD, 2002. Cellular fluid mechanics. Annual Review of Fluid Mechanics 34:211-232.

Klein-Nulend J, van der Plas A, Semeins CM, Ajubi NE, Frangos JA, Nijweide PJ, Burger EH, 1995. Sensitivity of osteocytes to biomechanical stress in vitro. FASEB J 9:441-5.

Knapp HF, Reilly GC, Stemmer A, Niederer P, Knothe Tate ML, 2002. Development of preparation methods for and insights obtained from atomic force microscopy of fluid spaces in cortical bone. Scanning 24:25-33.

Knothe Tate ML, Knothe U, Niederer P, 1998a. Experimental elucidation of mechanical load-induced fluid flow and its potential role in bone metabolism and functional adaptation. Am J Med Sci 316:189-195.

Knothe Tate ML, Niederer P, Knothe U, 1998. In vivo tracer transport through the lacunocanalicular system of rat bone in an environment devoid of mechanical loading. Bone 22:107-117.

Knothe Tate ML, Niederer P, 1998. Theoretical FE-based model developed to predict the relative contribution of convective and diffusive transport mechanisms for the maintenance of local equilibria within cortical bone. Advances in Heat and Mass Transfer in Biotechnology. 362:133-142.

Knothe Tate ML, Knothe U, 2000. An ex vivo model to study transport processes and fluid flow in loaded bone. J Biomech 33:247-254.

Knothe Tate ML, Steck R, Forwood MR, Niederer P, 2000. In vivo demonstration of load-induced fluid flow in the rat tibia and its potential implications for processes associated with functional adaptation. J Exp Biol 203:2737-2745.

Knothe Tate ML, 2001. Interstitial fluid flow. In: Cowin SC (ed.) Bone Biomechanics Handbook, 2nd ed. CRC Press, New York, NY, USA, pp. 1-29.

Knothe Tate ML, 2001. Mixing mechanisms and net solute transport in bone. Ann Biomed Eng 29:810-811.

Knothe Tate ML, 2002. Micropathoanatomy of osteoporosis – Indications for a cellular basis of bone disease. Adv Osteoporotic Fract Mgmt 2:9-14.

Knothe Tate ML, 2003. “Whither flows the fluid in bone?” An osteocyte’s perspective. J Biomech 36:1409-1424.

Knothe Tate ML, Adamson JR, Tami AE, Bauer TW, 2004. The osteocyte. Int J Biochem Cell Biol 36:1-8.

Knothe Tate ML, 2006. Multiscale computational engineering of bones: State-of-the-art insights for the future. In: Bronner, F., Farach-Carson, M.C., Mikos, A.G., eds. Engineering of Functional Skeletal Tissues. New York, NY: Springer, pp. 141-159.

Koerner RJ, Butterworth LA, Mayer IV, Dasbach R, Busscher HJ, 2002. Bacterial adhesion to titanium-oxy-nitride (TiNOX) coatings with different resistivities: a novel approach for the development of biomaterials. Biomaterials 23:2835-2840.

Kufahl RH, Saha S, 1990. A Theoretical Model for Stress-Generated Fluid Flow in the Canaliculi-Lacunae Network in Bone Tissue. J Biomech 23:171-180.

Kumar TR, Krishnan LK, 2002. A stable matrix for generation of tissue-engineered nonthrombogenic vascular grafts. Tissue Eng 8:763-770.

Lacroix D, Prendergast PJ, 2000. Mechanotransduction during fracture healing: the effect of cell proliferation. In: Ribreau, Berland, Moreau, Ratier, Renaudeaux, Thiriet, Wendling (Eds.) Mechanotransduction. Groupement pour l'avancement des methods d'analyse des contraintes G.A.M.A.C. et Soci, Paris, pp. 39-46

Lanyon LE, Baggott DG, 1976. Mechanical function as an influence on the structure and form of bone. J Bone Joint Surg 58B:436-443.

Leonardo da Vinci, 1508. Ms. F. In: Johnstone RE, Thring MW (eds.) Pilot plants, models, and scale-up methods in chemical engineering, McGraw-Hill, New York.

Liebschner M, Keller T, 1998. Hydraulic strengthening affects the stiffness and strength of cortical bone. Comp Meth Bioeng 20:761-762.

Liebschner MAK, Keller TS, 1999. The importance of the permeability constant in hydraulic strengthening of cortical bone. In: ASME Bioengineering Division, Summer Conference.

Lipp W, 1954. New studies of bone tissues; morphology, histochemistry and the effects of enzymes and hormones on the peripheral autonomic nervous system. Acta Anat (Basel) 22:151-201.

Mak AFT, Huang DT, Zhang JD, Tong P, 1997. Deformation-induced hierarchical flows and drag forces in bone canaliculi and matrix microporosity. J Biomech 30:11-18.

Manfredini, P, Cocchetti G, Maier G, Redaelli A, Montevicchi FM, 1999. Poroelastic Finite Element Anasysis of a Bone Specimen Under Cyclic Loading. J Biomech 32:135-144.

McCann JA, Peterson SD, Plesniak MW, Webster TJ, Haberstroh KM, 2005. Non-uniform flow behavior in a parallel plate flow chamber : alters endothelial cell responses. Ann Biomed Eng 33: 328-36.

McGarry JG, Klein-Nulend J, Mullender MG, Prendergast PJ, 2005. A comparision of strain and fluid shear stress in stimulating bone cell responses—a computational and experimental study. FASEB J 19:482-4.

Mikos AG, Sarakinos G, Lyman MD, Ingber DE, Vacanti JP, Langer R, 1993. Prevascularization of porous biodegradable polymer. Biotechnol Bioeng 42, 716.

Mishra S, Knothe Tate ML, 2003. Effect of lacunocanalicular architecture on hydraulic conductance in bone tissue: Implications for bone health and evolution. Anat Rec 273A:752-762.

Nauman EA, Satcher RL, Keaveny TM, Halloran BP, Bikle DD, 2001. Osteoblasts respond to pulsatile fluid flow with short-term increases in PGE(2) but no change in mineralization. J Appl Physiol 90:1849-1854.

Neuman MW, Neuman WF, 1980. On the measurement of water compartments, pH and gradients in calvaria. Calcif Tissue Int 31:135-145.

Nicolella DP, Moravits DE, Gale AM, Bonewald LF, Lankford J, 2006. Osteocyte lacunae tissue strain in cortical bone. J Biomech 39:1735-43.

Nowinski JL, Davis CF, 1972. The flexure and torsion of bones viewed as anisotropic poroelastic bodies. Intl J Eng Sci 10:1063-1079.

Owan I, Burr DB, Turner CH, Qiu J, Tu Y, Onyia JE, Duncan RL, 1997. Mechanotransduction in bone: osteoblasts are more responsive to fluid forces than mechanical strain. Am J Physiol 273:C810-5.

Palumbo C, 1986. A three-dimensional ultrastructural study of osteoid-osteocytes in the tibia of chick embryos. Cell Tissue Res 246:125-131.

Papadaki M, Eskin SG, 1997. Effects of fluid shear stress on gene regulation of vascular cells. Biotechnol Prog 13:209-221.

Pavalko FM, Chen NX, Turner CH, Burr DB, Atkinson S, Hsieh YF, Qiu J, Duncan RL, 1998. Fluid shear-induced mechanical signaling in MC3T3-E1 osteoblasts requires cytoskeleton-integrin interactions. Am J Physiol 275:C1591-C1601.

Pavalko FM, Gerard RL, Ponik SM, Gallagher PJ, Jin Y, Norvell SM, 2003. Fluid shear stress inhibits TNF-alpha-induced apoptosis in osteoblasts: a role for fluid shear stress-induced activation of PI3-kinase and inhibition of caspase-3. J Cell Physiol 194:194-205.

Peinkowski D, Pollack SR, 1983. The origin of stress-generated potentials in fluid-saturated bone. J Orthop Res 1:30-41.

Piekarski K, Munro M, 1977. Transport mechanism operating between blood supply and osteocytes in long bones. Nature 269:80-82.

Piekarski K, 1981. Mechanically enhanced perfusion in bone. In the Joint ASME-ASCE Applied Mechanics, Fluids Engineering and Bioengineering Conference: Mechanical Properties of Bone. New York.

Porter B, Zauel R, Stockman H, Guldberg R, Fyhrie D, 2005. 3-D computational modeling of media flow through scaffolds in a perfusion bioreactor. J Biomech 38:543.

Pozrikidis C, 1997. Shear flow over a protuberance on a plane wall. J Eng Math 31:29-42.

Prendergast PJ, Huiskes R, Soballe K, 1997. Biophysical stimuli on cells during tissue differentiation at implant interfaces. J Biomech 30:539-548.

Raimondi MT, Boschetti F, Falcone L, Fiore GB, Remuzzi A, Marazzi M, Marinoni E, Pietrabissa R, 2002. Mechanobiology of engineered cartilage cultured under a quantified fluid dynamic environment. Biomech Modeling Mechanobiol 1:69.

Raimondi MT, Boschetti F, Falcone L, Migliavacca F, Remuzzi A, Dubini G, 2004. The effect of media perfusion on three-dimensional cultures of human chondrocytes: Integration of experimental and computational approaches. Biorheology 41:401.

Rayleigh L, 1892. On the question of the stability of the flow of fluids. Phil Mag 34:59-70.

Rayleigh L, 1904. Fluid friction on even surfaces. Phil Mag 8:66-67.

Rayleigh L, 1915. The principle of similitude. Nature 95:66-68.

Rectenwald JE, Moldawer LL, Huber TS, Seeger JM, Ozaki CK, 2000. Direct evidence for cytokine involvement in neointimal hyperplasia. Circulation 102:1697-1702.

Reich KM, Frangos JA, 1991. Effect of flow on prostaglandin E2 and inositol trisphosphate levels in osteoblasts. Am J Physiol 261:C428-32.

Reilly GC, Knapp HF, Stemmer A, Niederer P, Knothe Tate ML, 2001. Investigation of the morphology of the lacunocanalicular system of cortical bone using atomic force microscopy. Ann Biomed Eng 29:1074-1081.

Reilly GC, Haut TR, Yellowley CE, Donahue HJ, Jacobs CR, 2003. Fluid flow induced PGE2 release by bone cells is reduced by glycocalyx degradation whereas calcium signals are not. Biorheology 40:591-603.

Reynolds O, 1893. An experimental investigation of the circumstances which determine whether the motion of water shall be direct or sinuous, and of the law of resistance in parallel channels. Phil Trans R Soc Lond 174:935-982.

Reynolds O, 1895. On the dynamical theory of incompressible viscous fluids and the determination of the criterion. Phil Trans R Soc Lond 186:123-164.

Roesler H, 1981. Some historical remarks on the theory of cancellous bone structure (Wolff's Law). In The Joing ASME-ASCE Applied Mechanics, Fluids Engineering and Bioengineering Conference: Mechanical Properties of Bone. New York. pp. 27-42.

Roux W, 1885. Beitrage zur morphologie der funktionellen anpassung. Arch Anat Physiol Anat Abt 120-185.

Rubin CT, Lanyon LE, 1984. Regulation of bone formation by applied dynamic loads. J Bone Joint Surg Am 66:397-402.

Rubin CT, Lanyon LE, 1985. Regulation of bone mass by mechanical strain magnitude. Calc Tissue Intl 37:411-417.

Salih V, Greenwald SE, Chong CF, Coumbe A, Berry CL, 1992. The development of an in-vitro perfusion system for studies on cultured cells. Int J Exp Pathol 73:625-632.

Scherft JP, 1972. The lamina limitans of the organic matrix of calcified cartilage and bone. J Ultrastruct Res 38:318-31.

Schlichting H, 1933. Laminare Strahlenhausbreitung. Z Angew Math Mech 13, 260, 1933.

Sikavitsas VI, Bancroft GN, Lemoine JJ, Liebschner MAK, Dauner M, Mikos AG, 2005. Flow perfusion enhances the calcified matrix deposition of marrow stromal cells in biodegradable nonwoven fiber mesh scaffolds. Ann Biomed Eng 33:63.

Smalt R, Mitchell FT, Howard RL, Chambers TJ, 1997. Induction of NO and prostaglandin E2 in osteoblasts by wall-shear stress but no mechanical strain. Am J Physiol 273:E751-8.

Srinivasan S, Gross TS, 2000. Canalicular fluid flow induced by bending of a long bone. Med Eng Phys 22:127-133.

Steck R, Niederer P, Knothe Tate ML, 2000. A finite difference model of load-induced fluid displacements within bone under mechanical loading. Med Eng Phys 22:117-125.

Steck R, Niederer P, Knothe Tate ML, 2003. A finite element analysis for the prediction of load-induced fluid flow and mechanochemical transduction in bone. J Theor Biol 220:249-259.

Steck R, Knothe Tate ML, 2005. In silico stochastic network models that emulate the molecular sieving characteristics of bone. Ann Biomed Eng 33:87-94.

Sorkin AM, Dee KC, Knothe Tate ML, 2004. "Culture shock" from the bone cell's perspective: emulating physiological conditions for mechanobiological investigations. Am J Physiol Cell Physiol 287:C1527-1536.

Tami AE, Nasser P, Verborgt O, Schaffler MB, Knothe Tate ML. 2002. The role of interstitial fluid flow in the remodeling response to fatigue loading. J Bone Miner Res 17:2030-2037.

Tami AE, Schaffler MB, Knothe Tate ML, 2003. Probing the tissue to subcellular level structure underlying bone's molecular sieving function. Biorheology 40:577-590.

Tedgui A, Mallat Z, 2001. Anti-inflammatory mechanisms in the vascular wall. Circ Res 88:877-887.

Tsuji T, Kawada Y, Kai-Murozono M, Komatsu S, Han SA, Takeuchi K, Mizushima H, Miyazaki K, Irimura T, 2002. Regulation of melanoma cell migration and invasion by laminin-5 and alpha3beta1 integrin (VLA-3). Clin Exp Metastasis 19:127-134.

Wang L, Fritton SP, Cowin SC, Weinbaum S, 1999. Fluid pressure relaxation depends upon osteonal microstructure: modeling an oscillatory bending experiment. J Biomech 32:663-672.

Weinbaum S, Cowin Sc, Zeng Y, 1992. Fluid shear stress excitation of osteocytes. Adv Bioeng 22:25-28.

Weinbaum S, Cowin SC, Zeng Y, 1994. A model for the excitation of osteocytes by mechanical loading-induced bone fluid shear stresses. J Biomech 27:339-360.

Weinger JM, Holtrop ME, 1974. An ultrastructural study of bone cells: the occurrence of microtubules, microfilaments and tight junctions. Calc Tissue Res 14:15-29.

White FM, 1991. Viscous Fluid Flow. 2nd ed., McGraw Hill, New York, NY.

Wilkinson JC, Stein RA, Guyer CA, Beechem JM, Staros JV, 2001. Real-time kinetics of ligand/cell surface receptor interactions in living cells: binding of epidermal growth factor to the epidermal growth factor receptor. Biochemistry 40:10230-10242.

Wolff J, 1892. Das gesetz der transformation der knochen. Berlin, Hirschwald.

Wolpert L, 1969. Positional information and the spatial pattern of cellular differentiation. J Theor Biol 25:1-47.

Yellowley CE, Jacobs CR, Donahue HJ, 1999. Mechanisms contributing to fluid-flow-induced Ca2+ mobilization in articular chondrocytes. J Cell Physiol 80:402-408.

You J, Yellowley CE, Donahue HJ, Zhang Y, Chen Q, Jacobs CR, 2000. Substrate deformation levels associated with routine physical activity are less stimulatory to bone cells relative to loading-induced oscillatory fluid flow. J Biomech Eng 122:387-93.

You L, Cowin SC, Schaffler MB, Weinbaum S, 2001. A model for strain amplification in the actin cytoskeleton of osteocytes due to fluid drag on pericellular matrix. J Biomech 34:1375-1386.

You LD, Weinbaum S, Cowin SC, Schaffler MB, 2004. Ultrastructure of the osteocyte process and its pericellular matrix. Anat Rec A Discov Mol Cell Evol Biol 278:505-13.

Younis HF, Kaazempur-Mofrad MR, Chung C, Chan RC, Kamm RD, 2003. Computational analysis of the effects of exercise on hemodynamics in the carotid bifurcation. Ann Biomed Eng 31:995-1006.

Zeng Y, Cowin SC, Weinbaum S, 1994. A fiber matrix model for fluid flow and streaming potentials in the canaliculi of an osteon. Ann Biomed Eng 280-292.

Zhang D, Cowin SC, 1994. Oscillatory bending of a poroelastic beam. J Mech Phys Solids 42:1575-1599.

Zhang D, Cowin SC, 1996. Load carrying capacity of the pore pressure in a poroelastic beam subject to oscillatory excitation. In: Selvadurai (Eds.) Mechanics of poroelastic media. Kluwer Academic Publishers, pp. 273-298.

Zhang D, Weinbaum S, Cowin SC, 1998. Estimates of the Peak Pressures in Bone Pore Water. J Biomech Eng 120:697-703.

Zhang D, Weinbaum S, Cowin SC, 1998b. On the calculation of bone pore water pressure due to mechanical loading. Intl J Solids Struc 35:4981-4997.